2010

Electro-optical And All-optical Switching In Multimode Interference Waveguides Incorporating Semiconductor Nanostructures

Nathan Bickel
University of Central Florida

ELECTRO-OPTICAL AND ALL-OPTICAL SWITCHING IN MULTIMODE INTERFERENCE WAVEGUIDES INCORPORATING SEMICONDUCTOR NANOSTRUCTURES

by

NATHAN P. BICKEL
B. S. in Optics, Institute of Optics, University of Rochester, 1998
M. S. in Optics, Institute of Optics, University of Rochester, 1999
M.S. in Optics, CREOL, The College of Optics and Photonics, University of Central Florida, 2009

A dissertation submitted in partial fulfillment of the requirements
for the degree of Doctor of Philosophy
in CREOL, The College of Optics and Photonics
at the University of Central Florida
Orlando, Florida

Summer Term
2010

Major Professor: Patrick LiKamWa

ABSTRACT

The application of epitaxially grown, III-V semiconductor-based nanostructures to the development of electro-optical and all-optical switches is investigated through the fabrication and testing of integrated photonic devices designed using multimode interference (MMI) waveguides. The properties and limitations of the materials are explored with respect to the operation of those devices through electrical carrier injection and optical pumping. MMI waveguide geometry was employed as it offered advantages such as a very compact device footprint, low polarization sensitivity, large bandwidth and relaxed fabrication tolerances when compared with conventional single-mode waveguide formats.

The first portion of this dissertation focuses on the characterization of the materials and material processing techniques for the monolithic integration of $In_{0.15}Ga_{0.85}As/GaAs$ self-assembled quantum dots (SAQD) and InGaAsP/InGaAsP multiple quantum wells (MQW). Supplemental methods for post-growth bandgap tuning and waveguide formation were developed, including a plasma treatment process which is demonstrated to reliably inhibit thermally induced interdiffusion of Ga and In atoms in $In_{0.15}Ga_{0.85}As/GaAs$ quantum dots. The process is comparable to the existing approach of capping the SAQD wafer with TiO_2, while being simpler to implement along-side companion techniques such as impurity free vacancy disordering. Study of plasma-surface interactions in both wafer structures suggests that the effect may be dependent on the composition of the contact layer.

The second portion of this work deals with the design, fabrication, and the testing of MMI switches which are used to investigate the limits of electrical current control when

employing SAQD as the active core material. A variable power splitter based on a 3-dB MMI coupler is used to analyze the effects of sub-microsecond electrical current pulses in relation to carrier and thermal nonlinearities. Electrical current controlled switching of the variable power splitter and a tunable 2 x 2 MMI coupler is also demonstrated.

The third part of this dissertation explores the response of $In_{0.15}Ga_{0.85}As/GaAs$ SAQD waveguide structures to photogenerated carriers. Also presented is a simple, but effective, design modification to the 2 x 2 MMI cross-coupler switch that allows control over the carrier distribution within the MMI waveguide. This technique is combined with selective-area bandgap tuning to demonstrate a compact, working, all-optical MMI based switch.

To my parents and grandparents: For their endless support and unending love throughout this long adventure.

ACKNOWLEDGMENTS

I am very grateful to my advisor, Dr. Patrick LiKamWa, for the support and patience over the last several years. I would also like to thank the dissertation committee members for their time and effort. Also my appreciation to my fellow group members over the years, including Dr. Daniel May-Arrioja, Dr. Inwoong Kim, Dr. Hyungseok Bang, Tony Ho, and Abdullah Zakariya. I would also like to mention Jeremy Mares, Clarisse Mazuir, Jeremy Brown, Amitabh Ghoshal, Hubert Seigneur, Dr. Nishant Bhatambrekar, Dr. Ivan Divliansky, Dr. Fatih Yaman, Dr. Scott Webster and Dr. Pradeep Srinvasan who provided help in one way or another, and to all the CREOL students, staff, and faculty, thank you.

To my parents, Carl and Joyce, who were there to listen when times got rough, and who believed in me throughout this long journey, I am forever thankful. To my grandparents, John & Helen Harvish, and Walter & Catherine Bickel who kept my spirits up, and particularly to Walter who passed away last year, but who never lost faith in my ability to succeed, thank you.

TABLE OF CONTENTS

LIST OF FIGURES

LIST OF TABLES

LIST OF ACRONYMS

AFM	Atomic Force Microscope
BOE	Buffered Oxide Etchant
CCD	Charge-Coupled Device
ICP	Inductively Coupled Plasma
IID	Impurity Induced Disordering
IFVD	Impurity Free Vacancy Disordering
MMI	Multimode Interference
MQW	Multiple Quantum Well
PAID	Photo-Absorption Induced Disordering
PECVD	Plasma Enhanced Chemical Vapor Deposition
PEI	Plasma Enhanced Intermixing
PII	Plasma Induced Intermixing
PL	Photoluminescence
QD	Quantum Dot
QW	Quantum Well
QWI	Quantum Well Intermixing
RIE	Reactive Ion Etching
RTA	Rapid Thermal Annealing
TE	Transverse Electric
TM	Transverse Magnetic

SAQD	Self-Assembled Quantum Dot
SEM	Scanning Electron Microscope
WCE	Wet Chemical Etching
WDM	Wavelength Division Multiplexing
VPS	Variable Power Splitter

CHAPTER 1: INTRODUCTION

Telecommunications systems have seen rapid advancement over the past 30 years. The earliest fiber networks deployed on a commercial scale yielded a transmission capacity of only 45 Mb/s [1]. New technologies and advances in optical fiber have allowed for a near continuous expansion of system capacity, transmission speed and subsequent cost reduction. These improvements include low loss fiber [2], dispersion shifted fiber [3], fiber amplifiers [4, 5], diode lasers that open up new bandwidth regimes and wavelength division multiplexing (WDM) [6-8]. Today systems routinely operate with a capacity on the order of Tb/s using multiple channels per fiber by employing WDM signals [6, 8]. In recent times, some of the major concerns have been the adaptation of new materials and technological platforms to applications in optical communication networks, continuing the trend towards faster, more compact, and more energy efficient systems.

Further development of optical communications networks will rely heavily on the continued evolution of the active components which handle the generation, routing, and conversion of information within these systems. This information control can be carried out in a number of ways and may be electronic, electro-optical or all-optical in nature. Those networks which rely on electronic information processing are restricted by their active components which set an inherent limit on bandwidth and consequently, the speed of information transfer. Electro-optical and, to a greater extent, all-optical networks, are not as limited and allow for much larger bandwidths and overall processing speeds due to the partial or complete elimination of electronic-to-optical and optical-to-electronic conversions respectively. The changeover from

electronic to electro-optical and all-optical controls is one of the major factors driving current telecommunications research. Since the principle expense for networks today is due to the equipment mediating the optical-electronic-optical conversions, system cost will also be substantially reduced.

Photonic integrated circuits based on III-V semiconductors are an important means by which both electro-optical and all-optical information control can be achieved, with multiple functionalities, such as modulation, amplification, detection and switching, combined into a single construct. Heterostructures employing InP and GaAs material systems typically have broad operational bandwidths, which can be well matched to optical fiber transmission windows. The active layer materials in these structures have steadily advanced from bulk semiconductors in the eighties to quantum wells in the nineties and early 21st century and into the beginnings of commercial exploitation of quantum dots over the last few years [9].

Waveguiding structures fabricated from quantum dot arrays have a number of advantages over quantum well devices. Due to three-dimensional quantum confinement and a discrete density of states, these advantages include narrower spectral linewidth, larger characteristic temperature, higher differential quantum efficiency, and lower threshold current density [10, 11]. A quantum dot laser, for instance, should be able to achieve at least a 1:10 reduction in threshold current density over an equivalent quantum well device [11]. Applications, which have been realized in the literature, range from quantum dot lasers [12, 13] to superluminescent light emitting diodes [14] to semiconductor optical amplifiers based on quantum dots [15, 16], and some switching applications [17, 18]. At least one company has reached the stage of producing commercialized quantum dot lasers [9].

But with these recent applications of quantum dots to the fabrication of lasers, detectors, and semiconductor optical amplifiers for use in telecommunications systems, the exploration into complementary active components for the manipulation of optical signals, utilizing similar material systems, is becoming more crucial. Several characteristics of quantum dots that offer clear advantage over bulk or MQW materials and which are pertinent to electro-optic and all-optical switching have been reported, including enhanced optical and electro-optical nonlinearities [19-21]. Switching devices utilizing quantum dots should then be expected to experience a reduction in power consumption without a loss in device performance. This is of particular importance in the fabrication of switching devices for applications such as optical cross-connects and in time-division signal processing schemes, where reduced power requirements can lead to significant cost savings. However, the study of quantum dot based devices such as external modulators, active switches and power splitters is incomplete. There is a need for additional understanding of the limitations and strengths of such devices fabricated using quantum dot platforms.

1.1 Outline

In this work, the application of epitaxially grown $In_{0.15}Ga_{0.85}As/GaAs$ self-assembled quantum dots (SAQD) to the development of integrated photonic switches is investigated through the fabrication and testing of electro-optical and all-optical devices designed for information transfer and encoding. The properties and limitations of the material are being explored with respect to the operation of those devices through electrical carrier injection and

optical pumping. In chapter 2, materials and material processing techniques are characterized for the monolithic integration of III-V SAQD and MQW structures. Supplemental methods for post-growth bandgap tuning and waveguide formation are developed, including a plasma treatment process which permits effective control of vacancy disordering in $In_{0.15}Ga_{0.85}As/GaAs$ quantum dots. The characterization of plasma-surface interactions is shown to be critical in selecting the proper fabrication steps for use prior to high temperature annealing. Chapter 3 focuses on the design, fabrication, and the testing of several multimode interference (MMI) switches which are used to investigate the limits of electrical current control when employing SAQD as the active material. A variable power splitter based on a 3-dB MMI coupler is used to analyze the effects of sub-microsecond electrical current pulses in relation to carrier and thermal nonlinearities. Current controlled switching of the variable power splitter and a tunable 2 x 2 MMI coupler is also demonstrated. Chapter 4 explores the response of $In_{0.15}Ga_{0.85}As/GaAs$ SAQD waveguide structures to photogenerated carriers. Also presented is a simple, but effective, design modification to the 2 x 2 MMI cross-coupler switches that allows control over the carrier distribution within the MMI waveguide. This technique is combined with bandgap tuning to demonstrate a compact, working, all-optical MMI based switch. Finally, chapter 5 summarizes this dissertation and provides suggestions for future work.

CHAPTER 2: SELF-ASSEMBLED QUANTUM DOT AND MULTIPLE QUANTUM WELL MATERIAL CHARACTERIZATION AND PROCESSING

Over the course of this work, a number of materials and a number of material processing techniques were employed. Both self-assembled quantum dot (SAQD) and multiple quantum well (MQW) wafers were studied for use in device construction. The properties of SAQD wafers were examined for application to electro-optical and all-optical switches, while the MQW material was chosen for the fabrication of all-optical devices. This chapter is committed to discussing these materials and detailing their initial characterization. Investigations into photoluminescence and electroluminescence properties, and the effects of electrical current injection were conducted. Monolithic integration techniques such as impurity free vacancy disordering (IFVD), sputter etching, and selective wet chemical etching were also studied in preparation for device fabrication, along with the development of supplementary methods for bandgap tuning and waveguide formation.

2.1 $In_{0.15}Ga_{0.85}As/GaAs$ Self-Assembled Quantum Dot Wafer

The $In_{0.15}Ga_{0.85}As/GaAs$ self-assembled quantum dot wafer employed in this work was manufactured using molecular beam epitaxy (MBE) on an n^+ GaAs (3×10^{18} cm^{-3}) substrate by NL Nanosemiconductor (now Innolume) of Germany. The epitaxial structure consists of a 500 nm GaAs buffer layer, followed by a 15 nm transition zone and then a n-doped 1.5 μm $Al_{0.35}Ga_{0.65}As$ lower cladding layer. Ten layers of $In_{0.15}Ga_{0.85}As/GaAs$ quantum dots spaced

between eleven GaAs barrier layers, each 33 nm thick, formed the active region which was nominally undoped. The upper cladding was 1.5 μm of $Al_{0.35}Ga_{0.65}As$ and was followed by another 15 nm transition zone. This was capped by a 200 nm GaAs contact layer. The contact layer has a doping concentration of $1x10^{20}$ cm^{-3} and the doping level in the AlGaAs cladding layers is approximately $1x10^{18}$ cm^{-3}. The wafer structure is p-i-n and is shown in Fig. 2.1.

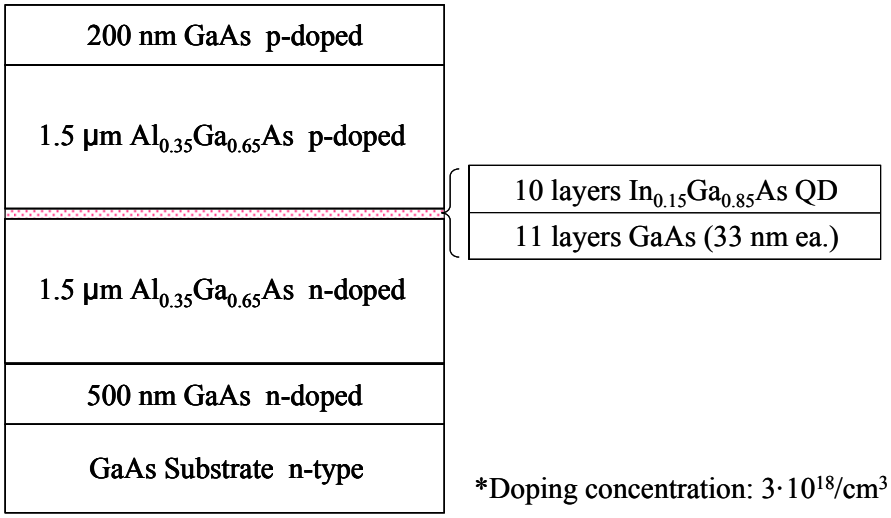

Figure 2.1 $In_{0.15}Ga_{0.85}As$/GaAs SAQD wafer structure.

2.1.1 Electroluminescence Measurements

A ridge waveguide with ohmic contacts placed along the top and bottom was used to measure the room temperature electroluminescence of the SAQD material. The 9 μm wide ridge waveguide was formed by etching through the upper cladding and through the SAQD region, and was cleaved to a length of 1.8 mm. Current was applied through a current probe placed on the top contact using an IXL Lightwave LDX-3525 precision current source. The

electroluminescence was collected with a SMF-28 lensed fiber attached to an Agilent 86146B Optical Spectrum Analyzer which was used to gather the data. The emissions peak was located at approximately 1272 nm (Fig 2.2) and had a FWHM of 55 nm.

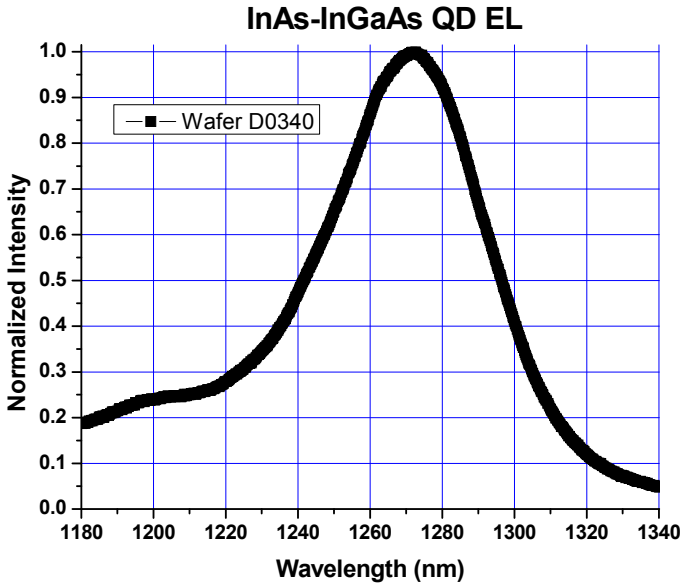

Figure 2.2 SAQD electroluminescence measured at 308.6 A/cm^2.

During the electroluminescence measurements it was observed that the emissions peak shifted to higher energies (shorter wavelengths) as the current injection level was increased. The change was relatively small, ranging from 1275.88 nm at a current density of 61.73 A/cm^2 (10 mA) to 1272.30 nm at 185.19 A/cm^2 (30 mA) as shown in Fig. 2.3. At this point the effect saturated and no further change for increasing current density up to 250 A/cm^2 was noted, excepting a small reduction at 308 A/cm^2. This blue shift in the electroluminescence emission spectrum has been previously reported in both quantum wells and quantum dots [22] and is attributed to the band filling of the conduction band by the injected electrons. With the electrical

injection of carriers into semiconductor materials, electrons and holes rapidly, and respectively, fill the states within the bottom of the conduction band and the top of the valence band. As this continues, transitions no longer can occur at $k = 0$ and higher energies are required to lift an electron from the valence band to the conduction band, resulting in a blue-shift to both the absorption and emission spectrums [23]. The small shift in the spectrum toward longer wavelengths at 308 A/cm^2 may be an indication of device heating which would result in a narrowing of the optical bandgap, counteracting the blue shift due to band filling.

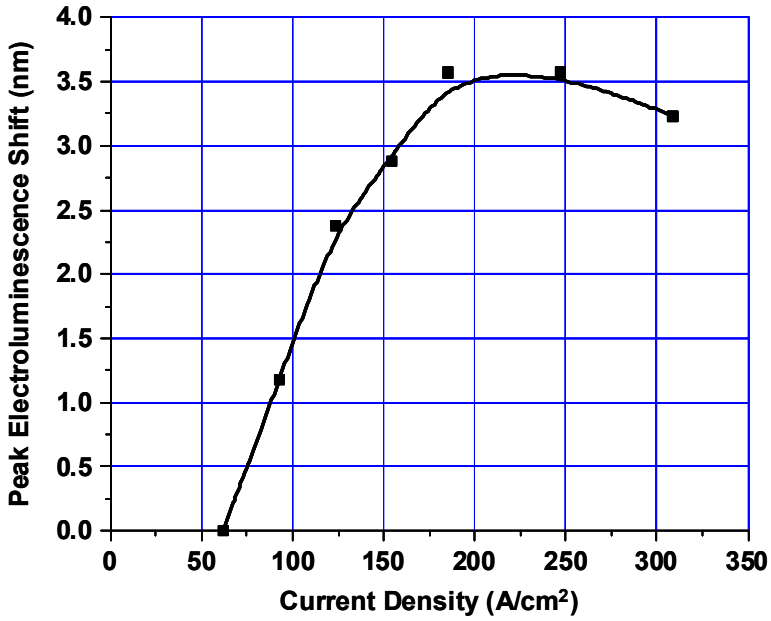

Figure 2.3 Blue shift of electroluminescence emission peak.

2.1.2 Bandgap Tuning and Suppression of Vacancy Disordering

A critical step in the development of complex optoelectronic devices and sub-systems is the ability to integrate multiple functionalities into a single monolithic structure. Selective-area

tuning of the semiconductor active region is often used in order to provide for the differing bandgap requirements of each subcomponent. Manipulation of the bandgap can be accomplished during epitaxial growth, either through growth-etch-regrowth [24] techniques or selective-area epitaxial growth [25-27]. These approaches can produce large bandgap differences with a high degree of spatial resolution over the semiconductor surface, however the former case needs multiple epitaxial growth steps that are time consuming and expensive, while the latter case requires precise placement of pre-growth masking layers and accurately tailored growth conditions. In view of these issues, extensive study has been made of post-growth intermixing methods, particularly in QW and MQW's. These techniques include, but are not limited to, photo-absorption induced disordering (PAID) [28-30], impurity induced disordering (IID) [28, 31], and impurity free vacancy disordering (IFVD) [32-35]. Each of these approaches has their importance in optoelectronic device fabrication, with advantages that depend on the precise application requirements. IFVD, in particular, has received a great deal of notice in the literature, due to its relative simplicity, good spatial resolution between regions of different bandgap energies [32, 35], and its tendency to conserve the electrical properties of the disordered QW [36].

To enhance intermixing in III-V QWs, IFVD techniques employ a dielectric capping layer (e.g. SiO_2) during high temperature, rapid thermal annealing. At these elevated temperatures, gallium (Ga) from the wafer surface (e.g. GaAs, InGaAs, etc) crosses the dielectric-semiconductor boundary, and out-diffuses into the dielectric film, creating vacancies in the group III sublattice. Diffusion of these vacancies through the active region promotes the flow of constituent atoms between the well layer and the barriers, with the elemental components

moving from regions of high concentration to low. With the blurring of the previously sharp concentration gradient between well and barrier, the optical bandgap typically widens and the emission properties of the QW shift to shorter wavelengths. Thermal intermixing (i.e without a capping layer) also shifts the bandgap energies to shorter wavelengths, principally functioning through the innate defects (vacancies and interstitials) which formed during the MBE or metal-organic chemical vapor deposition (MOCVD) growth processes [37, 38]. Since few such vacancies are generally present in QW's, and are finite in number, the shift in the peak bandgap energy is much smaller than would be expected with IFVD for a given annealing temperature and process duration. The success of IFVD as a post-growth technique for selective bandgap tuning in QW and MQW materials depends on the exploitation of this divergence between the capped and uncapped regions.

In contrast, post-growth manipulation of the bandgap in SAQD materials has proven to be considerably more challenging. SAQD's possess a much higher density of unintentional background vacancies as a result of low temperature growth, a large surface area to volume ratio, and large variances in the concentration of constituent elements, in addition to a high level of strain inherent in the growth process. These factors lead to large shifts in the bandgap energy of raw, annealed-only quantum dot samples during thermal intermixing. Consequently, the advantages gained from vacancy formation at the GaAs-SiO_2 (or InGaAs-SiO_2) interface during IFVD [39] are limited, and the relatively small difference in the bandgap energy between capped and uncapped samples is insufficient for many applications. Still, techniques such as capping with highly strained Si_3N_4 [40, 41], SrF_2 [42], and electron beam evaporated TiO_2 [39, 43, 44] exist and have been reported to inhibit the movement of vacancies, thereby reducing the degree

of intermixing compared to uncapped regions of the QD samples. Most prominent among these approaches is work on the implementation of TiO_2 capping layers to suppress disordering. In a single annealing step, this technique was used to generate three distinct bandgaps in an $In_{0.5}Ga_{0.5}As/GaAs$ quantum dot wafer sample where one section was capped with SiO_2 film, a second was capped with a SiO_2/TiO_2 bilayer, and the final section was left uncapped [43].

Other methods for controlling the interdiffusion in both QW and SAQD structures have attempted to influence the degree of defect generation in III-V materials through plasma treatments. The study of plasma-induced intermixing (PII) covers the use of various plasmas, generated in reactive ion etching (RIE) chambers or in inductively coupled plasma reactors, to create a near-surface layer of point defects in the target structure. This is followed by an annealing step which allows the defects to diffuse down to the QW region where they promote intermixing [45, 46], producing a blue-shift in the bandgap energies. While this can be viewed as an extension of ion implantation, where high energy ions (keV or MeV) are used to create defect sites deep inside the upper cladding [47, 48], the ion energies in PII are significantly lower (~100 eV or less) and cause much less damage to the crystal structure. However, PII, like IID, and ion implantation are used to enhance thermal interdiffusion, as opposed to suppressing it. In an adaptation of the IFVD technique, oxygen-based plasma was used to treat the SiO_2 capping films prior to annealing in order to adjust the solubility of the dielectric layer to gallium out-diffusion. When compared to samples coated with untreated SiO_2, the samples with the treated capping layer were shown to suppress vacancy generation (IFVD), but not necessarily thermal intermixing [49]. Interestingly, a number of works have looked at the passivation of semiconductor defect sites through exposing the material surface to molecular gasses. This

includes the passivation of dangling bonds in amorphous silicon with molecular hydrogen [50], and discussions concerning hydrogen passivation of gallium vacancies in wurtzite GaN [51] and zinc-blende GaN [52]. Hydrogen plasma has also been used to passivate the surface of bulk GaAs, with the passivation remaining thermally stable when annealed at 400 °C for one hour in vacuum [53]. Similarly, fluorine has been used to passivate vacancies in amorphous silicon-carbide [54], with vacancy passivation persisting despite annealing up to 800 °K. Furthermore, studies concerning the effects of fluorine containing plasmas on the native defects in GaAs/AlGaAs materials have been carried out [55]. The intention is to now investigate whether low energy plasma can be used to passivate the innate defects in III-V SAQD and thereby permit the suppression of interdiffusion during high temperature annealing.

In this section another option is offered for controlling interdiffusion in SAQD wafer structures during post-growth rapid thermal annealing. Treatment with a low pressure, CF_4-plasma prior to thermal annealing was determined to significantly limit the shift in the peak value of the room temperature photoluminescence for QD wafer samples. Minimal exposure to the plasma (1 minute) is sufficient to partially or fully halt the bandgap shift in the treated regions, thereby providing for efficient selective-area bandgap tuning in the material studied. As part of this research, $In_{0.15}Ga_{0.85}As$/GaAs SAQD samples exposed to CF_4-plasma prior to high temperature annealing are compared with samples coated with thermally deposited TiO_2, with samples coated with SiO_2 capping layers using plasma enhanced chemical vapor deposition (PECVD), and with uncapped, untreated samples (raw annealed) that act as experimental controls. Differential bandgap shifts as high as 84 meV (94 nm) were measured across the wafer surface for samples where half the surface was treated with the CF_4-plasma and half was

annealed without prior modification. These results matched well with those from the samples coated with the thermally deposited TiO_2 film, which produced an energy difference of 73.5 meV (82 nm) with respect to the raw annealed sample.

2.1.2.1 Experimental Details

The SAQD wafer samples utilized for this study were prepared using an ultrasonic bath and acetone to remove any debris and organic residue. The material was then soaked in a buffered oxide etchant solution to remove any native oxide. Several samples were coated with 200 nm of SiO_2 grown at 250 °C in a PlasmaTherm 790 Series PECVD system. Other samples were coated with 220 nm of thermally deposited TiO_2 in an Edwards FL 400 thermal evaporator. The remaining samples were uncapped and either exposed to a CF_4-plasma or else left untreated. Each uncapped sample treated with the plasma process was exposed for 2 minutes unless otherwise stated and the exposure was carried out in a PlasmaTherm 790 Series parallel plate RIE reactor. Table 2.1 lists the plasma process parameters that were used. In order to better replicate the conditions that would be present during device fabrication, each capped sample had one-half of the dielectric capping layer removed using the same CF_4-RIE process parameters given in Table 2.1. The etch rate for the SiO_2 layer was 32 nm/min, and therefore an etch time of 6.25 minutes was required to remove it completely. However, the total processing time of 8.5 minutes was to allow for an approximately two minute exposure of the wafer surface, similar to the uncapped, plasma-treated samples. The TiO_2 layer had an etch rate of 8 nm/min, and an etch time of 30 minutes was needed to clear the film and allow for the same two minute exposure.

A Heatpulse 210 AG Associates rapid thermal annealing furnace (RTA) operating under an N_2 flow was used to anneal the SAQD samples. In order to minimize process related variations, the different samples were annealed together for identical temperature values. After each sample set was loaded into the RTA, the chamber was purged with N_2 for 30 minutes to remove any oxygen that might react with the material surface. The annealing time at the target temperatures was 20 seconds for all cases, with a rise time of approximately 7 seconds. For this study, samples were annealed at 700 °C, 725 °C, 750 °C, 775 °C and 800 °C. To minimize the outgassing of arsenic during the annealing process, each sample was placed between two pieces of freshly cleaned GaAs mechanical wafer with the epitaxial layer facing down. This arrangement provides an arsenic overpressure that restricts the outflow of arsenic from the sample, reducing surface damage.

Table 2.1 Process parameters for CF_4-based reactive ion etching plasma.

CF_4-Based RIE Process	
CF_4 Flow	45 sccm
Residual Pressure	75 mT
RF Power	175 W
DC Bias	343 V
SiO_2 Etch Rate	32 nm/min
TiO_2 Etch Rate	8 nm/min

Photoluminescence data was acquired at room temperature (300 °K) using a SEO Titan CWBB Ti-Sapphire laser operating at 742 nm as the excitation source. The Ti-Sapphire laser

was pumped by a Coherent Innova 90 Argon-Ion laser operating at 514 nm. Light from the Ti-Sapphire laser was coupled into a single-mode optical fiber, passed into a power combiner (port 1), and then out (port 2) to a single-mode optical fiber which was cleaved at the output end. The cleaved end was used to deliver the excitation light to the surface of the SAQD sample, which was mounted on a xyz-stage to control positioning. Photoluminescence emitted from the quantum dot layers was collected with the same cleaved fiber and sent back to the power combiner (now power splitter). The portion of the emission passing to port 3 on the power combiner was then captured on an Agilent 86146B Optical Spectrum Analyzer. The experimental setup is diagramed in Fig. 2.4.

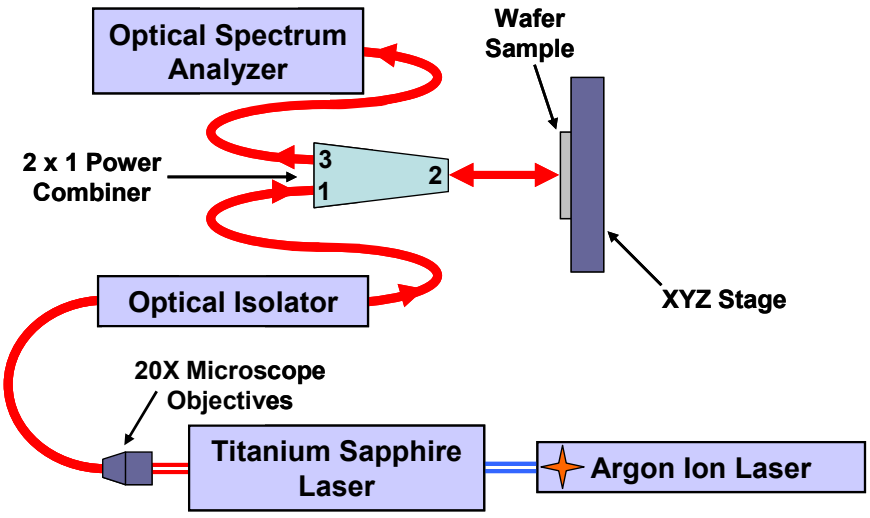

Figure 2.4 Experimental setup for photoluminescence measurements.

2.1.2.2 Results and Discussion

The photoluminescence spectra for three samples annealed at 775 °C for 20 seconds are shown in Fig. 2.5. These consist of the two capped samples, coated with SiO_2 and TiO_2 respectively, as well as an uncapped sample. One half of the uncapped sample was protected from the plasma, preserving the raw, untreated condition as a control, while the other half was exposed to the CF_4-plasma for 2 minutes. For the purpose of reference, the spectrum from an as-grown sample was also recorded. The photoluminescence peak from the sample annealed with a coating of 200 nm of PECVD grown SiO_2 is blue-shifted from the as-grown by 120 meV (140 nm). An almost identical shift of 114 meV is shown for the raw annealed sample, suggesting that too few vacancies were created at the SiO_2-GaAs boundary to significantly influence the disordering. Additional shifting might be attainable if the PECVD grown SiO_2 film were redesigned with a higher porosity level through adjustments in the growth temperature or the silane content of the gas mix [41]. Higher porosity would increase the solubility of the film to Ga, thereby enhancing vacancy creation at the SiO_2-GaAs boundary.

For the sample with 220 nm of thermally deposited TiO_2, a clear reduction in the bandgap shift was observed. The spectrum peak only moved 41 meV (51 nm) from the as-grown peak, or approximately one-third of the spectral shift experienced by the raw annealed sample. Vacancy motion within the sample is suppressed by the presence of the TiO_2 film, which has a larger thermal expansion coefficient (8.2×10^{-6} °C^{-1}) than GaAs (6.0×10^{-6} °C^{-1}), and as a result, induces tensile stress in the wafer surface during thermal annealing. The tensile stress has been determined to promote the formation of vacancy agglomerations, or clusters, as opposed to freely moving vacancies [56, 57]. By locking up the vacancies near the wafer surface, the film

dramatically reduces the degree of intermixing that can occur. This is in opposition to SiO_2, which has a much smaller thermal expansion coefficient (0.5×10^{-6} °C^{-1}) than GaAs, leading to a compressive stress in the GaAs surface when thermally annealed. This compressive stress field is believed to contribute to the interdiffusion process by helping push group III vacancies deeper into the sample [57]. It should be noted that the degree of interdiffusion suppression shown in Fig. 2.5 is surprising given the total thickness of the upper cladding and contact layers (1.715 μm). Most reports on this approach utilize epitaxial structures with very thin GaAs capping layers (≤ 200 nm) [43, 44] or thin contact and upper cladding layers (≤ 500 nm) [58]. The results presented in this work suggest that either the thermally induced strain field reaches deep into the upper cladding or that the majority of native defects are located near the wafer surface.

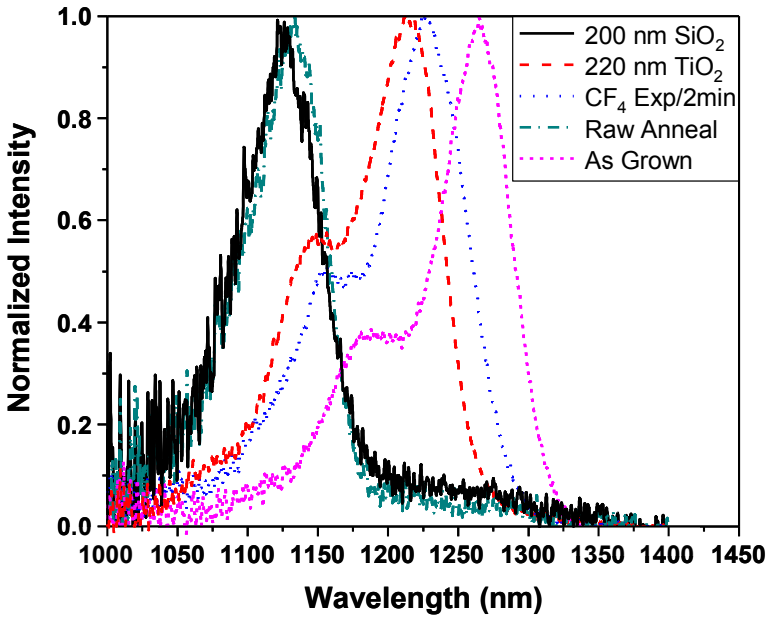

Figure 2.5 Room-temperature photoluminescence spectra for self-assembled quantum dots annealed at 775°C for 20s with capped (SiO_2 and TiO_2) and uncapped (CF_4 treated and raw annealed) samples.

The sample treated with the 2 min, CF_4-plasma process and then annealed at 775 °C for 20 seconds, compares favorably with the TiO_2 capped sample, suppressing the interdiffusion with respect to the raw annealed case, and allowing a blue-shift of only 31 meV (39 nm). The effectiveness of the plasma treatment is confirmed in Fig. 2.6 (a), which plots the shift in photon energy from the as-grown wafer for all four intermixing states, over a temperature range of 700 °C to 800 °C. A slight advantage is maintained by the plasma treated samples against those with thermally deposited TiO_2 for all temperature values studied. Photoluminescence measurements were also acquired for the portions of the capped samples where the dielectric film was completely removed with the CF_4-plasma process (Table 2.1) prior to the high temperature annealing (Fig. 2.6 (b)). This was done in order simulate the more realistic scenario of using dry-etching to remove dielectric films, including a deliberate 2 minutes of overetching, as might occur during device fabrication. In each instance, the results tracked well with the uncapped, plasma treated samples.

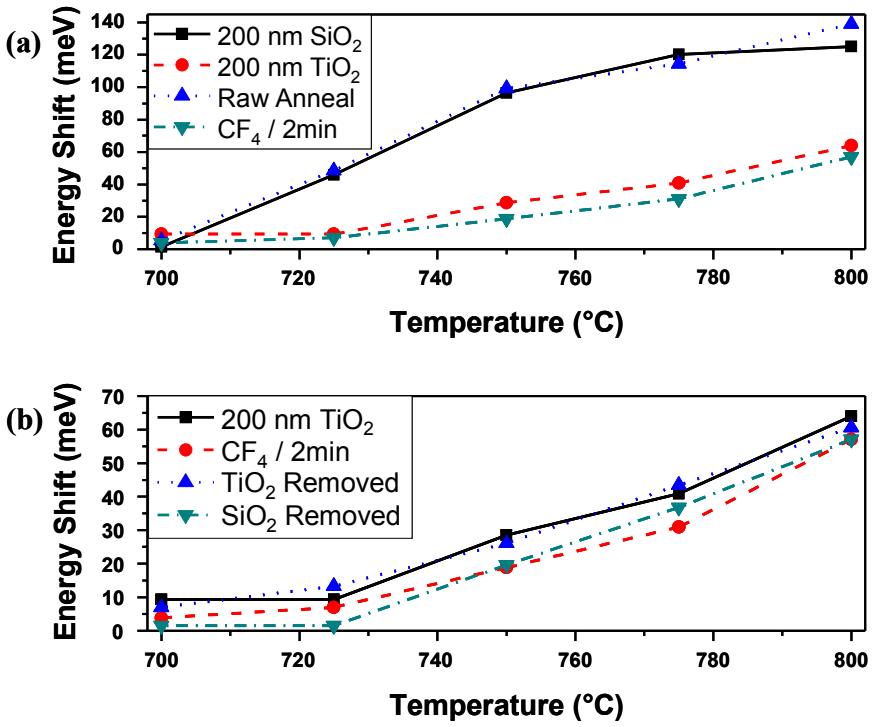

Figure 2.6 Energy shifts for (a) capped (SiO_2 and TiO_2) and uncapped (CF_4 treated and raw annealed) samples, and (b) capping removed with CF_4 plasma etch prior to annealing.

Further tests were conducted to better comprehend the limitations of the plasma treatment and its applicability to device fabrication and design. For one such test, the duration of the plasma treatment was varied for several SAQD samples. The treatment times were 1, 2, 5, and 15 minutes, after which the samples were annealed at 775 °C for 20 s. Photoluminescence measurements showed that there was no change in the degree of suppression, indicating that the full suppressive effect can be achieved in one minute or less. In the next series of tests, the RF power used to create the plasma was varied from 25 W to 175 W in intervals of 50 W. All of the samples were annealed at 775 °C for 20 seconds and no other parameters were altered. Beyond determining if altering the RF power will permit the degree of suppression to be tuned, a lower RF power should correlate to a smaller degree of damage to the wafer surface. For the recipe

given in Table 2.1 (175 W), the ablation rate for GaAs was determined to be approximately 5 nm/min. When the RF power is changed to 75 W, this is reduced to < 1 nm/min. Fig. 2.7 shows that the suppression effect is unchanged down to 75 W RF power, but that at 25 W RF power, the photoluminescence emission peak shifts abruptly to almost the same value as the raw annealed sample. It is therefore inferred that the suppression of intermixing requires a plasma process with a critical RF power of 75 W to be effective.

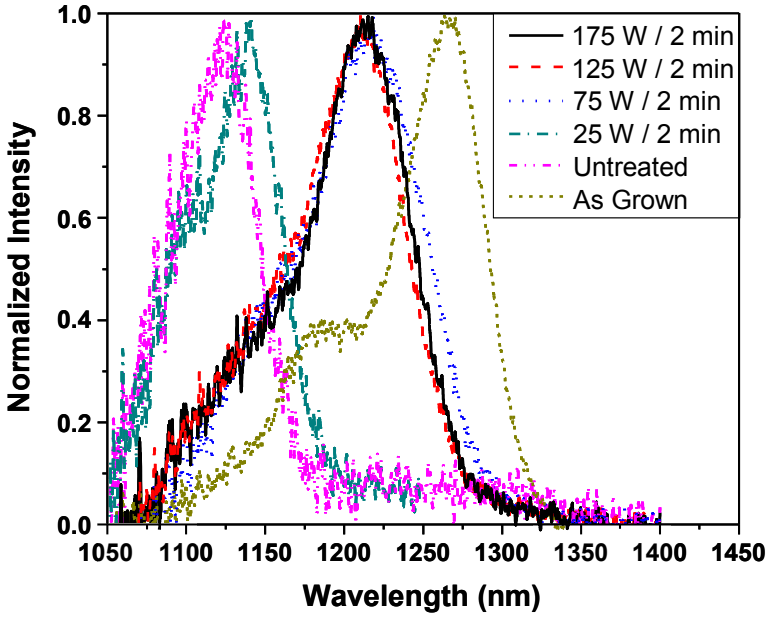

Figure 2.7 Room-temperature photoluminescence spectra for uncoated, plasma treated self-assembled quantum dots with varying RF power.

To quantify the spatial resolution of the suppression process, the uncapped samples from the test series shown in Fig. 2.5 were mounted on the photoluminescence test setup. Each sample was then scanned past the optical fiber in 1 μm increments using the xyz stage, with the boundary between the plasma treated and raw annealed sections perpendicular to the direction of

travel. For each 1 μm change in sample position, the photoluminescence spectrum was acquired. The spectrum remained unchanged until the boundary was reached, when over the course of two 1 μm steps, the whole spectrum abruptly shifted from the plasma treated state to the raw annealed state. In the middle of that 2 μm range, the spectrum was a combination of the raw annealed and plasma treated spectra. This held true for all annealing temperatures, suggesting that the spatial resolution of the intermixing process using the plasma treatment is comparable to that reported for IFVD [32, 34, 59].

The amount of suppression afforded by exposure to the CF_4-plasma is in part dependent on the annealing temperature. Duration of the exposure and the amount of RF power applied during the exposure appear to be much less important, though the exact extent in each case still needs to be determine. Initially it was hypothesized that the suppression of the bandgap energy shift was due to fluorine ions permeating the sample and acting to neutralize vacancies within the layer structure, possibly including those which form very close to the dot region due to the low temperature growth. It has been suggested in the literature that fluorine can passivate the dangling bonds on vacancies in amorphous silicon carbide [54], much as hydrogen has been shown to passivate vacancies in amorphous silicon [50] and GaN [51, 52]. Confirmation of this idea involved the creation of two additional plasma recipes. These recipes have the same parameters as the CF_4-plasma process given in Table 2.1, with the exception that the CF_4 gas is replaced with N_2 and O_2 respectively. A set of uncapped samples were prepared, with one half of each sample exposed to a particular plasma recipe for two minutes and the other half shielded from the plasma, so as to preserve the raw untreated condition. The samples were then annealed in the RTA at 775 °C for 20 s. The measured photoluminescence spectrum for each sample type

is plotted in Fig. 2.8 which clearly shows that the suppressive nature of the plasma is essentially independent of the gas used in creating the plasma. The spectra from the N_2-plasma treated sample and the CF_4-plasma treated sample overlap, with no difference in the position of the peak energy. Interestingly, the O_2-plasma treated sample shows a slight 13 meV (15 nm) blue-shift compared to the other two plasma processes, however the reason for this difference is unclear and requires further investigation. Regardless, these results negate the idea that fluorine ions are the passivating agent. Similar results were seen by T. S. Shamirzaev et al. whom conducted a series of QW photoluminescence intensity enhancement studies, though that work used noble gasses for comparison instead [55]. This suggests that there may be a connection between the QW intensity enhancement seen after CF_4 plasma etching and the QD interdiffusion suppression in this work. Based on that, we consider that the plasma treatment acts to create highly mobile point defects in the near surface region of the SAQD contact layer and upper cladding layer. These defects diffuse away from the surface and move deeper into the wafer where they form non-mobile complexes, or agglomerations, with ingrown defects [60]. While there is evidence that these defect complexes disassociate after low temperature (~400 °C / 30 s) rapid thermal annealing [60], we suspect that the complexes persist long enough to minimize vacancy induced disordering during the short duration, high temperature annealing process used in this study.

One study from the literature that bears resemblance to this work with SAQD is a H_2-plasma treatment which was reported to have suppressed bandgap shifts in GaAs/AlGaAs MQWs [61]. The MQW samples were treated with a H_2-plasma in an Oxford Plasma Technology dry etching machine using 30 W of RF power at a residual pressure of 400 mT with a 20 sccm flow. The total exposure time was 40 minutes and annealed at 900 °C for 1 minute,

producing a 33 nm shift for the raw, annealed-only sample, and a 2 nm shift for the treated sample. While superficially the published results are similar to work presented in this section, there are significant differences in the process and in the conclusions drawn by the authors. Principally, the authors' process relies on retaining the presence of the native oxide on the sample surface, which was removed in the case of the SAQDs, and on the reducing nature of hydrogen to alter the composition of the surface from As_2O_3, Ga_2O_3, and free As and Ga, into a continuous layer of Ga_2O_3 and AsH_3 gas. The authors' contend that this passivated the surface and prevented vacancy formation, thereby suppressing the bandgap shift, since Ga would not out-diffuse efficiently into its own oxide. The changes to the surface samples were confirmed by X-ray photoelectron spectroscopy [61]. However, a variant on this explanation would be that retaining the native oxides, particularly the A_2O_3, resulted in a degree of IFVD in the raw annealed sample, enhancing the interdiffusion beyond what would have occurred if the sample surface had been stripped clean. Additionally, it is presumed, but never made clear as to whether the 40 minutes exposure duration was necessary, or what results, if any, were produced by shorter durations. Finally, while it is difficult to completely prove that some of the thermal intermixing suppression seen with the $In_{0.15}Ga_{0.85}As$/GaAs SAQDs did not occur in the case of these MQWs, one must consider that a related publication utilized a short interval H_2-plasma process to enhance the intermixing in GaAs/AlGaAs MQW through PII [46]. Moreover, intermixing data for GaAs/AlGaAs MQW material presented in the Appendix, section 6.1.1, where the native oxide was removed, showed that rapid thermal annealing at 975 °C for 30 seconds produced only a 4 nm shift from the as grown condition, which is comparable to the shift reported for the H_2-plasma treated sample at a similar temperature [61].

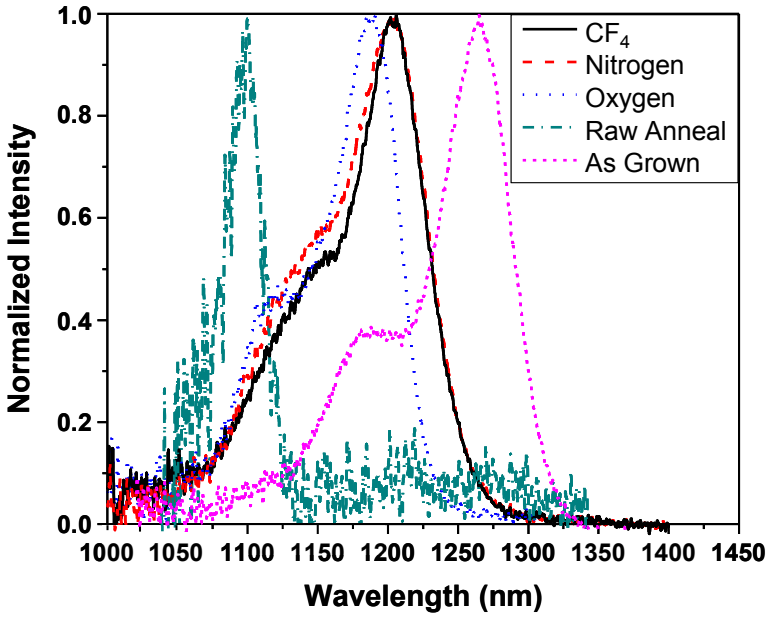

Figure 2.8 Room-temperature photoluminescence spectra for several uncoated, plasma treated self-assembled quantum dots with differing gas sources.

2.1.3 Analysis of Induced Change in Refractive Index

For many electro-optical and all-optical devices, functionality is based on the ability to invoke a change in refractive index of the constituent material. In some cases this change is uniform across the entire structure, but more often it is a localized change to a specific area or areas of the device, such as with Mach-Zehnder switches and many MMI devices. A common means by which a localized refractive index change is produced in semiconductor materials is through carrier induced nonlinearities, which principally consist of the band filling effect and the free carrier plasma effect. In GaAs based materials, both phenomenon result in a reduction in the refractive index, with the band filling effect as described in Section 2.1.1 and the free carrier plasma effect through intraband absorption of the carriers [23]. In this instance, the response of

the $In_{0.15}Ga_{0.85}As$/GaAs SAQD wafer material to electrical current injection was preliminarily investigated, and the polarity and extent of the refractive index change characterized.

2.1.3.1 Test Device Fabrication

To measure the refractive index change, a simple ridge waveguide was fashioned from the SAQD wafer material. Fabrication began with the growth of a 200 nm silicon nitride layer atop the wafer sample using a PlasmaTherm 790 plasma enhanced chemical vapor deposition (PECVD) system. The silicon nitride layer was then covered with a p-type photo-resist (Shipley S1805) using a Specialty Coating Systems P-6000 spin coater and the waveguide features were patterned with a Karl Suss MJB_3 mask aligner. The developed resist pattern was used as an etching mask for the silicon nitride layer and the pattern was transferred with a CF_4-based reactive ion etching (RIE) process (Table 2.2). Any remaining resist was removed and the silicon nitride acted as the mask for the wet chemical etching of the epitaxial layer using a solution of H_3PO_4:H_2O_2:H_2O in a volume ration of 1:5:50. The latter etch rate was determined to be approximately 368 nm per minute. The waveguides were etched down to a depth of 1450 nm below the surface and into the upper AlGaAs cladding. The remaining silicon nitride was removed with the same CF_4 etching process from Table 2.2.

Table 2.2 Silicon nitride etching process.

Silicon Nitride CF_4-Based RIE Process	
CF_4 Flow	12 sccm
O_2 Flow	1 sccm
Residual Pressure	75 mT
RF Power	100 W
Si_3N_4 Etch Rate	100 nm/min

A negative photo-resist (Futurrex NR7-1000PY) and another round of photolithography, followed by metal evaporation and liftoff, were employed to create a p-type contact (Au/Zn/Au) covering the top of each waveguide. The substrate was thinned through mechanical abrasion to a thickness of 120 nm and polished before an n-type contact layer was deposited on the substrate side of the sample (Ni/Ge/Au). The contacts were then annealed in a rapid thermal annealing furnace at 400°C for 2 minutes. Afterwards, samples were cleaved to around 935 microns in length and mounted on a copper header for testing.

2.1.3.2 Experimental Setup

The change in the refractive index was measured using a free space Mach-Zehnder setup shown in Fig 2.9. Light from a fiber coupled diode laser emitting at 1310 nm was sent through a lithium niobate modulator, and then collimated by a fiber collimator. A fiber-based polarization controller was positioned between the modulator and collimator allowing selection of either TE or TM polarized light (TE parallel to the active layer and TM perpendicular). This light was then

divided by a beam splitter into the test and reference arms of the setup. The beam in the test arm was launched into the ridge waveguide using a 40x microscope objective and was collected from the output facet using a second 40x microscope objective. The two beams were recombined at a second beam splitter and sent to a CCD camera so that the interference fringes could be viewed on a monitor. Current was injected into the waveguide, and the direction and amount of the resulting fringe shift was observed. This initial testing was done under CW conditions for both the laser source and the injected current.

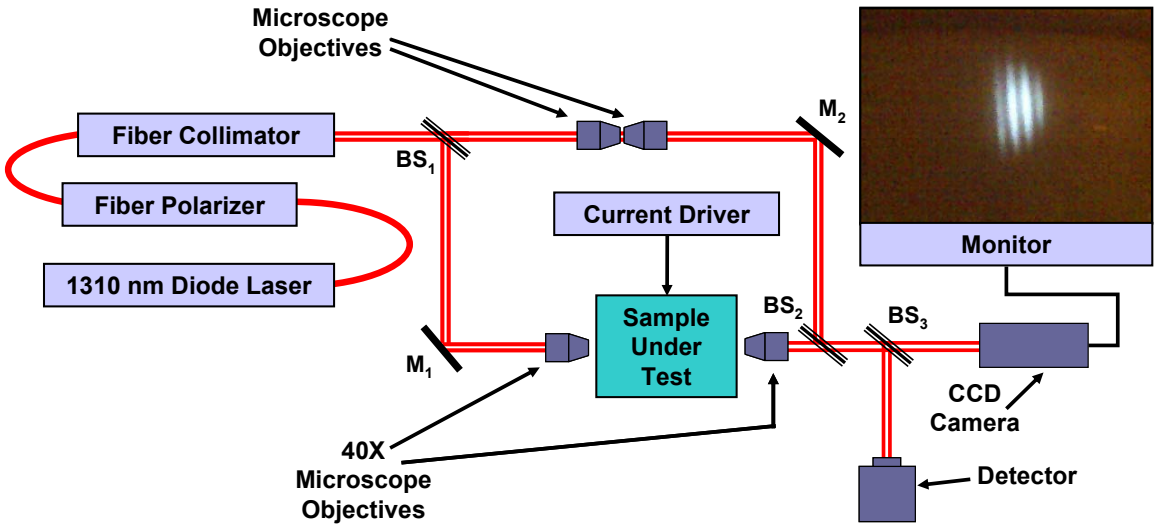

Figure 2.9 Free space Mach-Zehnder setup for index shift measurement.

2.1.3.3 Results and Discussion

In order to determine the polarity of the refractive index change, the direction of the fringe shift under current injection was compared with shifting induced by an external heat source and with that which occurred when the sample was subjected to a reverse bias voltage.

Both reference cases are known produce a positive change in the refractive index due to the thermo-optic effect and the quantum confined stark effect respectively. In contrast, carrier induced nonlinearities should yield a reduction in the refractive index. Once the direction for a positive index change was established, the waveguide was subjected to current injection, allowing the polarity and degree of the fringe shift to be measured for both TE and TM polarized light. The index change was calculated using Eqn. 2.1 for a Mach-Zehnder interferometer.

$$\Delta n = \frac{\Delta m \cdot \lambda_o}{L} \tag{2.1}$$

The results of this testing are shown in Fig. 2.10. For TM polarized light, there was an overall increase in the refractive index, save perhaps at very low current levels for which there was no discernable fringe shift. For TE polarized light, on the other hand, the initial fringe shift indicated a reduction of the refractive index at low current levels. This trend persisted until the current reach around 10 mA (118.84 A/cm^2), at which point the refractive index change abruptly reversed direction and began to recover, eventually yielding a net increase in the refractive index at 35 mA (415.92 A/cm^2).

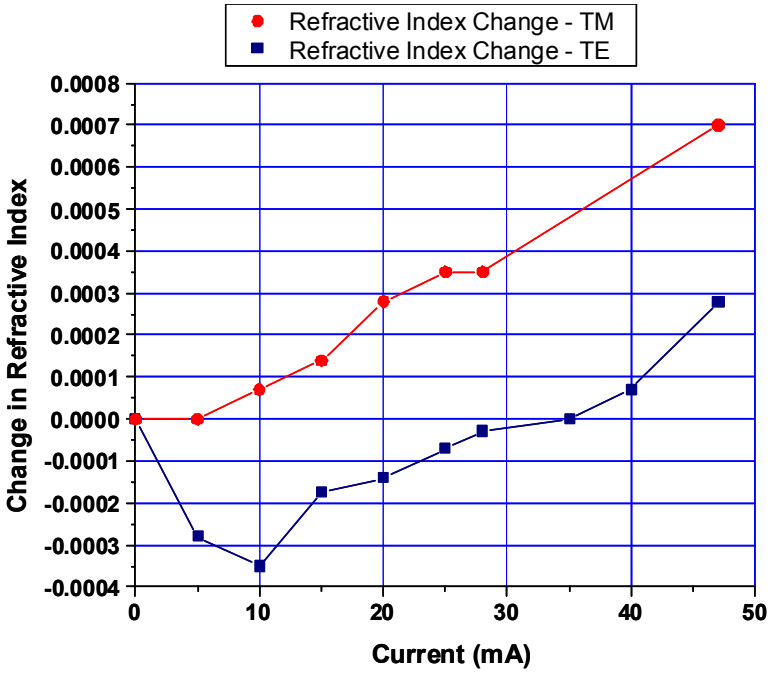

Figure 2.10 Refractive index change in SAQD wafer material.

These results suggest that under CW conditions, at least, there is significant competition between the refractive index change due to the presence of free carriers and refractive index change due to the thermo-optic effect. At low current levels, the carrier induced changes seem to dominate, while at larger current values, the thermo-optic effect is more significant. It is also interesting to note the difference between the two polarizations of the laser beam suggesting the carrier induced effect is stronger for TE polarized light, perhaps related to the anisotropy in the quantum dots physical characteristics seen by light polarized parallel and perpendicular to the growth plain [62]. As will be discussed in section 4.1.2, light polarized parallel to the growth plane is more readily absorbed by the SAQD material. Additionally, while it is anticipated that QDs will offer enhanced optical nonlinearities since the transparency of the ground state transition can be provided by a single electron-hole pair [19, 63, 64], there is some concern that

the induced refractive index change will be spread over a larger spectral range than with bulk materials or quantum wells, resulting in a smaller index change at a given wavelength [22].

2.1.4 Waveguide Loss

The optical propagation loss of the material was quantified for a single-mode waveguide by measuring the visibility of the Fabry-Perot fringes that are observed when the wavelength was scanned. The waveguides fabrication was similar to that described in section 2.1.3.1, but was 2 mm in length. Employing a fiber pig-tailed DFB laser diode, the Fabry-Perot response was measured from 1308.6 nm to 1309.4 nm with TE polarized light. From multiple measurements, the average loss was determined to be 11.51 dB/cm for TE polarized light at a wavelength of 1309 nm.

2.1.5 Waveguide Formation Employing Plasma Induced Surface Ablation

Waveguide formation through physical (sputter) etching of III-V semiconductor material was studied as an alternative to standard ion-assisted etching techniques that involve a combination of chemical and physical processes. Wet chemical etching, which is isotropic in nature, on its own cannot provide good fidelity with respect to the lateral dimensions of the devices fabricated in this work given the standard depth of the etching exceeds 1 μm. As control over the lateral dimensions was crucial to device function, a dry etching technique was

developed for transferring the waveguide patterns into the GaAs/AlGaAs structure of the QD wafer.

Based on observations of GaAs wafers following the over-etching of PECVD SiO_2 masking layers, it was speculated that GaAs based materials could be patterned using a high energy CF_4-based plasma (RF powers of 200 W to 300 W). Physical damage to the semiconductor surface due to over-etching of dielectric masks during typical RIE processing is expected [55], but the degree of material removal has generally not been discussed. Preliminary work began with the CF_4-plasma etching process given in Table 2.1, which was determined to have an approximate sputtering rate of 5 nm/min for GaAs. However, in order to produce a viable process, the rate of material removal needed to be increased. A PlasmaTherm 790 Series parallel RIE reactor was employed in creating the appropriate plasma conditions.

Since the degree of chemical interaction between CF_4-plasma and GaAs is generally non-existent [65], it was presumed that no advantage would be gained from seeking to balance the physical and chemical processes. With this in mind, the residual pressure was reduced to enhance the physical sputtering effect [66] and the RF power was increased for the same reason. CF_4 flow rates were also reduced to compensate for the lowered residual pressure. The addition of a small amount of oxygen flow (2 sccm) and nitrogen flow (3 sccm) was used to minimize the possibility of polymer formation [67]. The optimized recipe parameters are given in Table 2.3, along with the sputtering rates for different III-V semiconductor materials. The sputtering rate for both GaAs and $Al_{0.3}Ga_{0.7}As$ was 10.4 nm/min. While quite slow in relation to processes involving gasses such as Cl_2 and BCl_3, which give etch rates on the order 100 nm/min, the sputter rate is still viable for applications where shallow depths and precise etch control are required. Clearly,

for deep etching (~ 1 μm), the total time would be quite long (> 1.5 hours). However, that, in itself, is not necessarily detrimental in a research environment where long processing times are more acceptable than in manufacturing settings. Though the potential effects of etching damage would need to be considered [65, 68], the process could be of benefit in research settings where typical III-V etching gasses are not available.

Attempts to etch InGaAs and InP produced impractical etch rates of 5 nm/min and 1.5 nm/min respectively. Since the primary action is mechanical in nature and the majority of the material is being physically ablated from the semiconductor surface by the energetic ions, the lower rates are likely due to the presence of the heavier In atom. This suggests that the use of the recipe in etching In-containing semiconductor materials is only practical for relatively thin layers (~100 nm).

Table 2.3 Plasma sputtering process for the formation of semiconductor waveguides.

Plasma Parameters	
CF_4 Flow	18 sccm
N_2 Flow	3 sccm
O_2 Flow	2 sccm
Residual Pressure	20 mT
RF Power	225 W
GaAs/ $Al_{0.35}Ga_{0.65}As$ Sputter Rate	10.4 nm/min
$In_{0.53}Ga_{0.47}As$ Sputter Rate	5 nm/min
InP Sputter Rate	1.5 nm/min

2.1.5.1 Mask Development and Waveguide Formation

In order to utilize this sputtering process to fabricate waveguide structures in the $In_{0.15}Ga_{0.85}As/GaAs$ SAQD wafer, a masking layer needed to be developed which had a low reactivity with the ionized species present in the plasma, and could withstand the high energy bombardment and the necessarily long etching time, and which could be readily removed afterwards. Since CF_4 was the principal gas component of the plasma, and a typical choice in the etching of silicon based dielectrics, both SiO_2 and Si_3N_4 films offered poor selectivity, with mask thicknesses on the order of microns, if the intention were to etch through the $Al_{0.3}Ga_{0.7}As$ upper cladding (~1.7 μm). The alternative was some form of metal mask. As metal is difficult to removed from semiconductor surfaces, a layer of SiO_2 was grown prior to metal deposition. The SiO_2 could easily be etched using BOE without damaging the semiconductor surface, lifting away any remaining metal after waveguide formation was complete. Gold, investigated as a masking material, had good liftoff qualities, and it adhered well if a thin (5 nm) layer of Chromium was deposited first as an adhesion layer. However, the sputtering rate of the gold mask was > 5 nm/min, and it therefore possessed a poor selectivity with respect to the GaAs. A film thickness of at least 900 nm would have been required to etch through the upper cladding.

Chromium was considered as an alternative, given its good adhesion properties with respect to SiO_2, and its high resistance to CF_4 sputtering [67]. For the process in Table 2.3, the sputter rate of Cr was < 1 nm/min. Waveguide formation began with 400 nm of PECVD SiO_2 grown on the wafer sample. This was followed by patterning in Futurrex NR7-1000PY negative photo-resist with contact photolithography, and a 175 nm thick chromium mask was formed through evaporation and liftoff. Issues developed, however, once the pattern was transferred into

the SiO_2 film. Intermittently, the chromium mask, together with the underlying SiO_2 layer, would begin to peel away from the semiconductor surface after the uncovered SiO_2 was etched away. As chromium is known to form highly stressed metal films with tensile stress measured up to 1 MPa for films greater than 100 nm thick [69], it is speculated that for the 175 nm thick film used above, the level of stress was sufficient to overcome the adherence of the SiO_2 to the GaAs surface. The problem became significantly more acute when waveguide formation occurred after a BCB planarization step, with most attempts now resulting in the mask peeling back. It is believed that some residual polymer, or byproduct from etching the polymer, acted to reduce the adhesiveness of the SiO_2 layer.

Nickel, has similar qualities to Cr, including clean liftoff, strong adhesion to SiO_2, and better resistance to sputtering than gold, if less than Cr. However, Ni is significantly more ductile than Cr, and might be able to dissipate some of the stress in the Cr film if used in a combination. Several attempts were made which involved different groupings of Cr and Ni layers to find an arrangement which would provide the needed qualities. The final mask combination was 400 nm PECVD SiO_2, followed by thermal deposition of 40 nm Cr, 88 nm Ni, and 70 nm of Cr. The SiO_2 was easily removed after waveguide formation by immersion in HF or BOE, allowing for liftoff of unused metal. The combination of Cr/Ni/Cr, provided strong adhesion to the SiO_2, a good compromise on sputtering rate, and eliminated the problem of mask peeling. The average measured sputtering rate of the Cr/Ni/Cr film was approximately 1.1 nm/min. If BCB planarization had been used prior to waveguide formation, some peeling was still possible, but it was found that 50 nm of Si_3N_4, replacing the first 50 nm of the SiO_2 layer, provided better adhesion to the BCB modified surface, eliminating mask peel back in this instance.

Fig. 2.11 shows a SEM image of a rib waveguide structure etched into the $In_{0.15}Ga_{0.85}As$/GaAS QD wafer using the process in Table 2.3. The height of the waveguide is 1.925 μm, with the initial width of 3.4 μm. Note that the sidewalls are not vertical, but rather sloped with an angle of approximately 73 degrees. This renders the base of the waveguide 1.3 μm wider than desired. The extra width at the base is detrimental as it is enough that the waveguides displayed double mode tendencies when light was launched into the structure. This extra width can be compensated for by using a wet chemical etching solution to narrow the waveguides, reducing the lateral dimensions to approximately the desired limits. The solution was a combination of H_3PO_4:H_2O_2:H_2O in a ratio of 1:2:50 by volume, which has an etch rate of ~175 nm/min for GaAs and ~195 nm/min for $Al_{0.35}Ga_{0.65}As$.

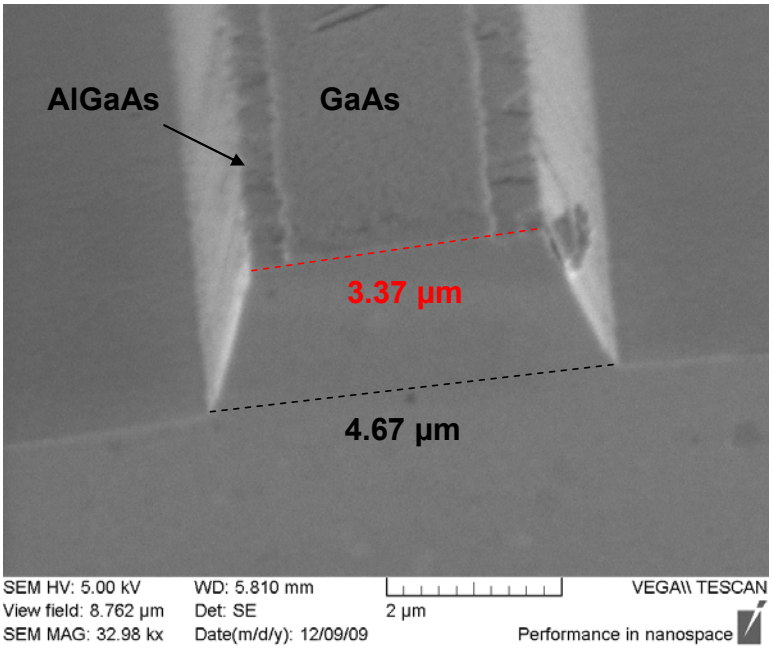

Figure 2.11 SEM image of waveguide formed in SAQD wafer material through plasma sputtering.

2.2 InGaAsP/InGaAsP Multiple Quantum Well Wafer

The InGaAsP/InGaAsP MQW wafer was grown using molecular beam epitaxy on an n+ InP substrate by IQE (Europe) Ltd. The *p-i-n* structure is shown in Fig. 2.12 and was originally designed for laser diode fabrication. Growth began with the formation of an n-type 1.5 μm InP lower cladding layer on top of the substrate, followed by an undoped 100 nm InGaAsP buffer layer. The active region contained five InGaAsP well layers, each 5.5 nm thick, which were interspaced with five InGaAsP barrier layers, each 10 nm thick. A second undoped, 70 nm thick, InGaAsP buffer layer was grown, preceding the upper cladding, which was 370 nm of p-type InP. The entire structure was capped with a 110 nm $In_{0.53}Ga_{0.47}As$ contact layer, doped p-type with a doping concentration of 1.3 x 10^{19} cm^{-3}. The doping concentration in the cladding layers was ~1 x 10^{18} cm^{-3}.

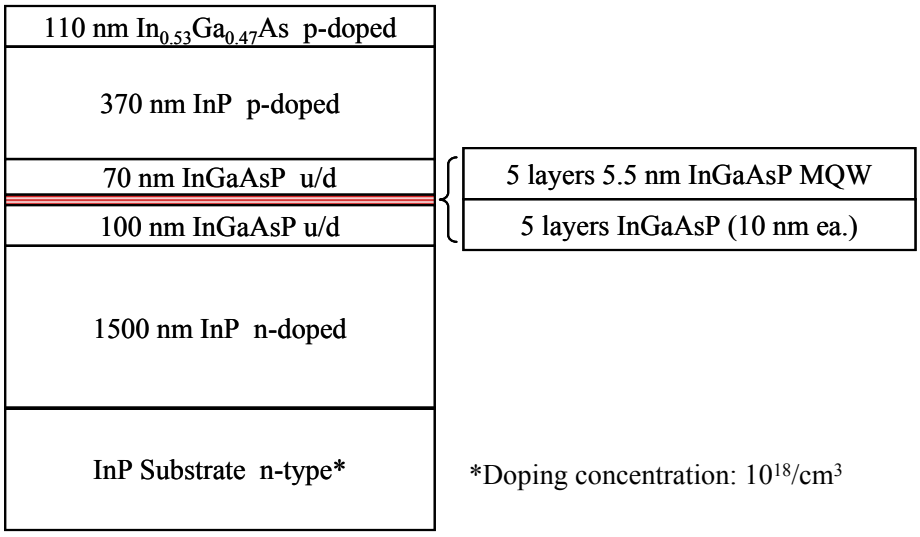

Figure 2.12 InGaAsP/InGaAsP MQW wafer structure.

2.2.1 Bandgap Tuning

2.2.1.1 Experimental Details

Post-growth intermixing tests for the InGaAsP/InGaAsP MQW wafer were carried out using a Heatpulse 210 AG Associates annealing furnace for temperature values ranging from 750°C to 850°C. The wafer samples were initially prepared by soaking in acetone and using an ultrasonic bath to remove debris and organic residue. This was followed by immersion in a buffered oxide etchant (BOE) solution to remove any native oxide. Samples were then either coated with 200 nm of SiO_2 grown at 250°C in a PlasmaTherm 790 Series PECVD system, or left uncapped. For the capped samples, the film was removed from one-half of the surface using the CF_4-plasma process from Table 2.1, with a total etching time of nine minutes. Around 2.5 minutes of over-etch were included to better approximate the conditions that might exist during device fabrication. The uncapped samples were also divided into two sections, with one-half of each sample exposed to the CF_4-plasma for three minutes, and one-half which was protected from the plasma, preserving the raw, untreated surface as a control. In order to minimize process related variations, the different sample sets were drawn from the same general area of the source wafer and annealed together for identical temperature values.

After each sample set was loaded into the RTA, the chamber was purged with N_2 for 30 minutes to remove any oxygen that might react with the material surface. The annealing time at the target temperatures was, for all cases, 20 seconds, with a rise time of approximately 7 seconds. As with the quantum dot material discussed in section 2.1.2, the samples were annealed epi-side down, between two pieces of freshly cleaned GaAs mechanical wafer, to reduce the

effects of Ar outgassing. Samples were tested at 750°C, 775°C, 800°C, 825°C, and 850°C. After annealing, BOE was used to remove the SiO_2 film from the capped sample, and all samples had the $In_{0.53}Ga_{0.47}As$ contact layer removed using a solution of H_3PO_4:H_2O_2:H_2O in a volume ratio of 1:1:30. Removal of the contact layer simplified acquisition of the photoluminescence emission, which had photon energies of 0.80 eV or greater, and was therefore highly absorbed by the $In_{0.53}Ga_{0.47}As$ which had a bandgap of approximately 0.74 eV.

The measurement setup was identical to the one described in section 2.1.2.1 (Fig. 2.4), with the exception that the Ti-Sapphire laser was replaced with a Mavericks Cr:Forsterite laser operating at 1240 nm. This was done in order to avoid the detection of the 740 nm Ti-Sapphire laser line in second order diffraction at 1480 nm, which would interfere with the acquisition of the photoluminescence spectrum for the InGaAsP/InGaAsP MQW samples.

2.2.1.2 Results and Discussion

The photoluminescence spectra for the two samples annealed at 800°C for 20 seconds are shown in Fig. 2.13. For reference, the spectrum from as-grown material was also recorded. The photoluminescence peak of the sample capped with 200 nm SiO_2 was blue-shifted approximately 19 meV (36 nm) from the as-grown. In comparison, the raw annealed sample exhibited a significantly smaller shift of 7 meV (14 nm) due to thermal intermixing. Unlike the quantum dot material in section 2.1.2, the amount of vacancy generation at the silica-semiconductor boundary was sufficient to induce an additional 12 meV of bandgap shift, reflecting the quality of the epitaxial material and the low number of innate vacancies present in the structure. Curiously, the

portion of the capped sample for which the SiO_2 film was removed prior to annealing, using CF_4-plasma etching, realized a shift in the emission spectrum of 13.5 meV (26 nm). An identical response was seen for the section of the uncapped wafer that was treated with the CF_4-plasma for 3 minutes. In contrast to the untreated wafer material, these results clearly indicate an enhanced blue-shift for those samples in which the surface has been exposed to the CF_4-plasma prior to annealing. Confirmation of this additional bandgap shift is shown in Figure 2.14, which plots the change in the peak photon energy with respect to the as-grown wafer over a temperature range of 750 °C to 850 °C. The rate of blue-shift for the SiO_2 capped sample increases suddenly when the temperature reaches 850 °C. In comparison, the rate of the CF_4 plasma enhanced bandgap shift remains steady. This difference may be due to increased vacancy generation at the SiO_2-semiconductor interface at higher temperatures.

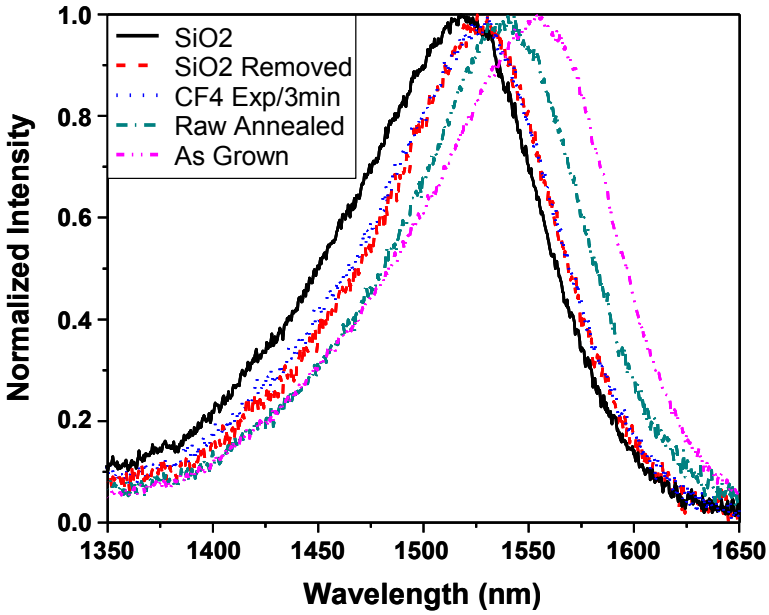

Figure 2.13 Room-temperature photoluminescence spectra for InGaAsP/InGaAsP multiple quantum wells annealed at 800°C for 20s with capped (SiO_2), cap removed (SiO_2 etched w/ CF_4 prior to annealing), and uncapped (CF_4 treated and raw annealed) samples.

Additional testing was conducted to better understand the nature of the plasma enhanced disordering effect. Two sets of uncapped samples were prepared. In the first set, one-half of each sample was exposed to the CF_4-plasma process for three minutes, while the other section was protected from the plasma, leaving the raw, untreated surface. The $In_{0.53}Ga_{0.47}As$ layer was then completely removed. In the second set, the $In_{0.53}Ga_{0.47}As$ layer was removed and then one-half of each sample was exposed to the plasma for three minutes. Both samples were then annealed at 825 °C along with a third sample. The third sample acted as a control and was divided into two sections. One section was exposed to the CF_4-plasma for three minutes, while the other section was left untreated. In this case, the $In_{0.53}Ga_{0.47}As$ layer was left intact prior to the annealing. The photoluminescence spectra acquired from these samples are shown in Fig. 2.15 and Fig. 2.16.

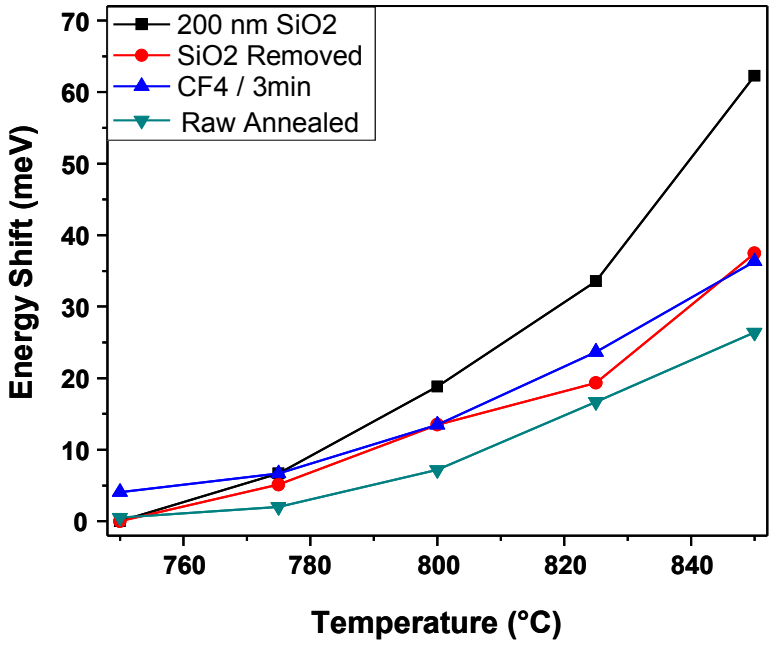

Figure 2.14 Energy shifts for capped (SiO_2), cap removed (SiO_2 etched w/ CF_4 prior to annealing), and uncapped (CF_4 treated and raw annealed) samples.

For the first sample, where the $In_{0.53}Ga_{0.47}As$ layer was removed after the CF_4-plasma treatment, but prior to annealing, the emission peaks for both the treated and untreated portions were blue-shifted 13.5 meV (26 nm) from the as-grown, with the spectra overlapping (Fig. 2.15). This is comparable to the sample that was raw annealed with the $In_{0.53}Ga_{0.47}As$ layer intact, which produced a blue-shift of 16.7 meV (32 nm). However, a 25 meV (48 nm) shift was seen for the sample where the wafer surface was treated with the plasma for three minutes and annealed with the $In_{0.53}Ga_{0.47}As$ layer intact. It is clear that the plasma enhanced blue-shift is eliminated if the $In_{0.53}Ga_{0.47}As$ layer is removed prior to the high temperature anneal. Interestingly, removal of the $In_{0.53}Ga_{0.47}As$ layer also seems to provide a slightly smaller blue-shift than the raw, annealed only state ($\Delta\varepsilon \approx 3meV$), suggesting that the $In_{0.53}Ga_{0.47}As$ layer contains a finite amount of innate defects which measurably influence the overall disordering.

For the second sample, in which the $In_{0.53}Ga_{0.47}As$ layer was removed prior to the plasma processing (Fig. 2.16), the photoluminescence peak shifted 23 meV (44 nm), almost the same amount as when the $In_{0.53}Ga_{0.47}As$ layer was left intact prior to annealing. This indicates that the magnitude of the plasma enhanced blue-shift is at least partially independent of the composition of the surface material. As with the first sample, the emission peak of the second sample's untreated section shifted only 13.5 meV (26 nm), again demonstrating that simply removing the $In_{0.53}Ga_{0.47}As$ layer will reduce the degree of thermal intermixing, if by only a few milli-electron volts.

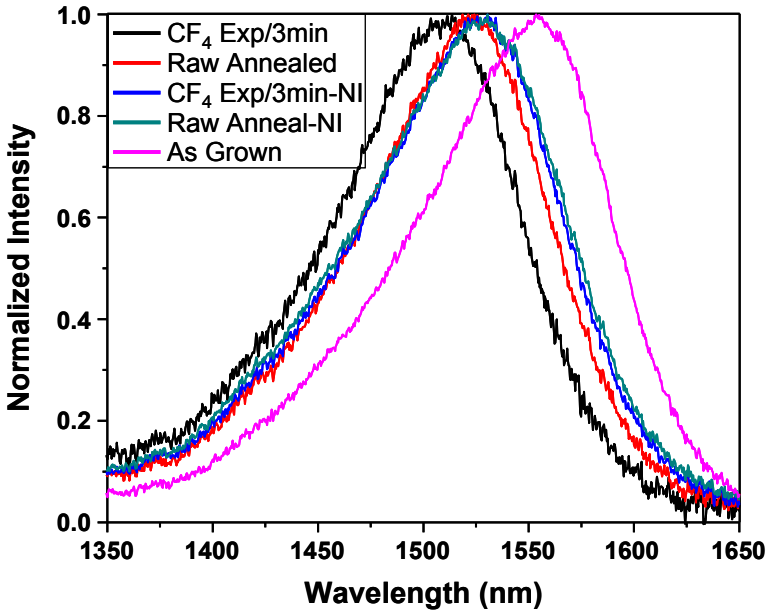

Figure 2.15 Room-temperature photoluminescence spectra for InGaAsP/InGaAsP multiple quantum wells annealed at 825°C for 20s with uncapped samples (CF_4 treated and raw annealed), and uncapped samples (CF_4 treated and raw annealed, then InGaAs removed (NI)).

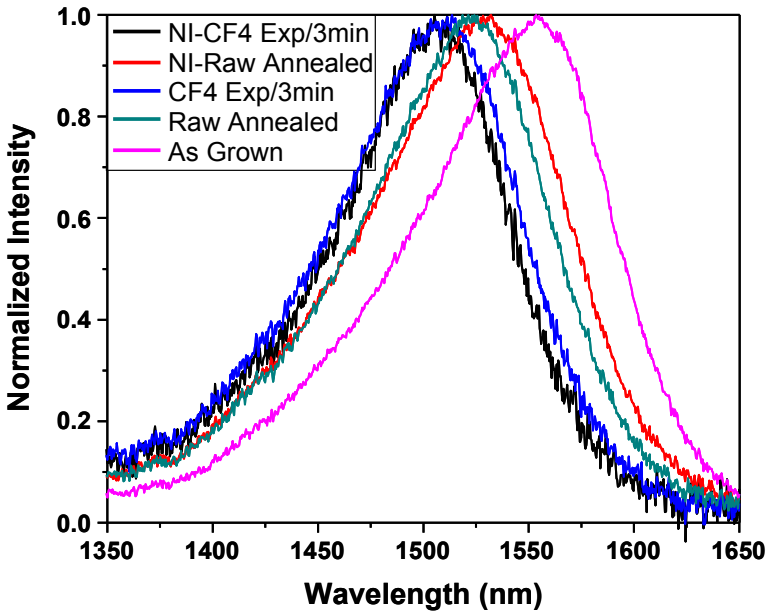

Figure 2.16 Room-temperature photoluminescence spectra for InGaAsP/InGaAsP multiple quantum wells annealed at 825°C for 20s with uncapped samples (CF_4 treated and raw annealed), and uncapped samples (InGaAs removed (NI), then CF_4 treated and raw annealed).

From the data presented, it is evident that exposure of the InGaAsP/InGaAsP MQW to CF_4-plasma prior to high temperature annealing leads to a significant enhancement of the thermal intermixing process. It is equally clear that this plasma enhanced bandgap shift is eliminated by the removal of the $In_{0.53}Ga_{0.47}As$ layer after CF_4-plasma treatment, but prior to annealing. It is concluded, that the added blue-shift is most likely caused by the creation of point defects in the near surface regions of the wafer as a result of damage induced by ion bombardment. The use of energetic plasma treatments to influence the degree of defect generation in III-V materials has been previously reported, and has been used to selectively disorder quantum well materials [45, 46, 70]. The technique, variably called plasma-induced intermixing (PII) or plasma enhanced intermixing (PEI), involves the use of plasma, generated in inductively coupled plasma reactors or in RIE chambers, to create a near-surface layer of point defects in the target structure. This is followed by an annealing step which allows the defects to diffuse down to QW region where they promote intermixing, producing a blue-shift in the bandgap energies [45, 46].

Clearly, the potential effect from the dry etching of masking layers must be taken into account during the initial characterization of any MQW or QD material system being used for fabrication. This is particularly important if the etching process is to be followed by high temperature thermal annealing. For the InGaAsP/InGaAsP system described here, definition of regions in the SiO_2 capping layer for MQW selective-area disordering should be carried out through wet chemical etching, or, if dry etching is used, by removal of all, or part of, the $In_{0.53}Ga_{0.47}As$ layer prior to annealing to realize the largest possible difference in the bandgap energies. Unlike the $In_{0.15}Ga_{0.85}As/GaAs$ SAQD structure from section 2.1.2, the defects

generated in the InGaAsP/InGaAsP MQW wafer, by the CF_4-plasma, act to enhance the thermal intermixing process as opposed to suppressing it. As the damage appears to be concentrated in the near surface region, the difference in the contact layers might be critical to the difference between suppression and enhancement. The study of low energy level argon ion bombardment of GaAs and InP suggest a significant difference in the number of atomic displacements between the two materials and in the nature of the defects generated [68]. The key question to be answered then is whether the presence of indium, which is lacking in the QD contact layer, is the prime factor in choosing between enhancement and suppression of the thermal intermixing process, or whether some other interaction between the plasma and the surface layer is responsible.

2.2.2 Wet Chemical Etching Characterization

Wet chemical etching of InP based semiconductors is a viable alternative to dry etching techniques, as these materials display crystallographically defined anisotropic etching profiles under certain conditions [71]. As has been noted in other works, for epitaxial layers grown on the {001} surface, the etch profile is dependent on both the particular crystal axis along which a waveguide is oriented, as well as the composition of the etchant [71, 72]. Waveguides can be oriented along {110} surfaces as these are the surfaces along which {001} InP naturally cleaves, providing an atomically smooth end facet. Moreover, there are several etchant combinations that allow for the selective etching of InP, but not its' ternary or quaternary compounds, which in this case are InGaAs and InGaAsP, respectively. Thus a sequence of etchants can be selected in

which the first etches the InGaAs, but is essentially nonreactive to the InP cladding layer, while a second etchant will remove the InP, but not the InGaAs.

The devices to be fabricated in this work are designed such that highly vertical etching profiles are desired, in order to more precisely match the theoretical model to the realized structure. For that reason, the InP etchant chosen was a solution of $HCl:H_3PO_4:CH_3CHOHCO_2H$ (hydrochloric acid: phosphoric acid: lactic acid) in a volume ratio of 2:5:2, as it has been shown to produce sidewalls at almost 90 degrees to the {001} surface, when the waveguide is parallel to the [110] direction [72]. The etchant for the InGaAs layer was a solution of $H_3PO_4:H_2O_2:H_2O$ (1:1:30) and is essentially isotropic. As the InGaAs layer is only 110 nm thick, this fact will not significantly affect the device dimensions. The InGaAsP of the intrinsic region is much less reactive to this etchant however, and a solution of $H_2SO_4:H_2O_2:H_2O$ (1:1:10) was used instead to provide a more efficient etching rate. The etching rates for the various layers in the corresponding solutions are shown in Table 2.4.

Table 2.4 Wet chemical etching solutions for InP based materials.

Material	Etchant	Volumetric Ratios	Etch Rate
$In_{0.53}Ga_{0.47}As$	$H_3PO_4:H_2O_2:H_2O$	1:1:30	125 nm/min
InP (P-Type)	$HCl:H_3PO_4:CH_3CHOHCO_2H$	2:5:2	145 nm/min
InGaAsP	$H_2SO_4:H_2O_2:H_2O$	1:1:10	75 nm/min

The profiles of waveguides etched along the [110] and [$\bar{1}$10] directions are shown in Fig. 2.17 (a) and Fig. 2.17 (b) respectively. The original mask width was 3 μm and the waveguide is

etched through the intrinsic region, stopping at the boundary between the lowest InGaAsP layer and InP lower cladding. As can be seen, the waveguide etched along the [110] axis presents nearly vertical sidewalls with effectively no undercut through the InP upper cladding. The InGaAsP region however shows an undercut of approximately 250 nm on each side, corresponding to a 1:1 etch ratio between the horizontal and vertical directions. With respect to device fabrication, the isotropic nature of the InGaAsP etchant will need to be accounted for when considering how variation in lateral dimensions effects device function. Finally it should be noted that the width of the InGaAs layer is reduced to ~1 μm during the etching of the InGaAsP region, as the H_2SO_4-based etchant is more reactive to the highly doped contact layer.

The waveguide etched along the [$\bar{1}$10] direction (Fig. 2.17 (b)) shows a markedly different profile. In this case, the InP layer forms a 41° angled plane with respect to the {001} surface. The closest plane that this corresponds to is the {0$\bar{1}$1} plane, though that is expected to form a 45° angle with respect to the {001} surface [71]. For this waveguide, the initial mask width was 3.5 μm. As the InP is etched, the width increases with depth, until the base of the InP layer is 4.3 μm wide. There is again an undercut during the InGaAsP etching step, though the sidewalls appear to be angled along a similar plane as for the InP layer. The actual width reduction of the intrinsic region is therefore somewhat less clear, with the width varying from 4 μm at the top to 4.3 μm at the base. Given this more angled profile, aligning the waveguides along the [110] direction should produces the most controllable results, provided the undercutting of the InGaAsP is taken into account.

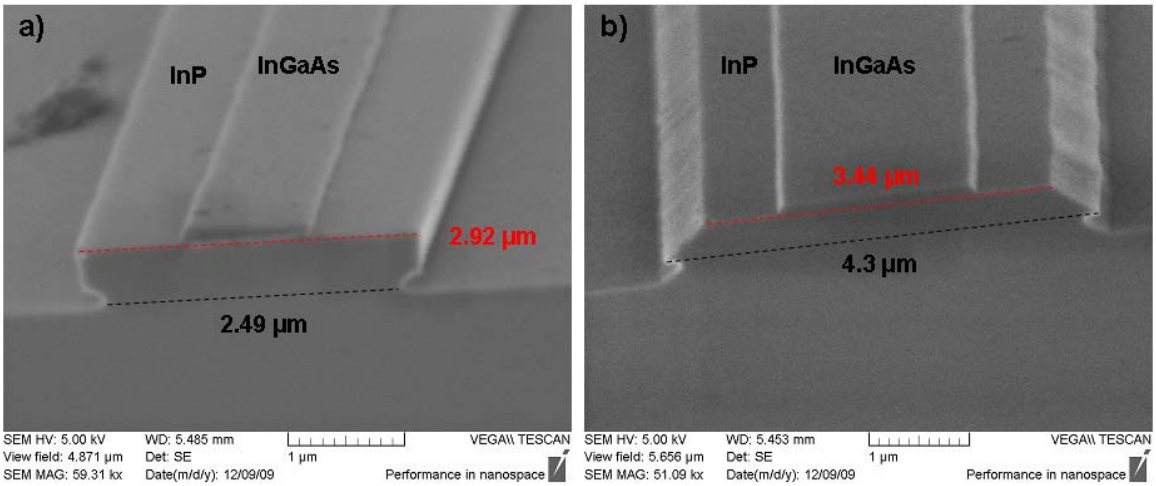

Figure 2.17 Waveguides etched in InGaAsP/InGaAsP MQW wafer structure: (a) Oriented along [110] direction; (b) Oriented along [$\bar{1}$10] direction.

2.2.3 Waveguide Loss

Single-mode waveguides, similar to the one shown in Fig. 2.17 (a), were fabricated to measure waveguide loss. The waveguides were 3 µm wide, 1.86 mm long, and etched through the InGaAsP region. A Santec TSL-210 tunable semiconductor laser was used to measure the transmitted intensity from 1540-1570 range in 10 pm steps. Losses were calculated from the measured visibility of the Fabry-Perot interference fringes. With the $In_{0.53}Ga_{0.47}As$ (0.74 eV) contact layer intact, the single-mode waveguide experiences significant absorption of light at 1550 nm (0.800 eV) and shorter. Removal of the contact layer substantially increases transmission, indicating that the guided mode penetrates through the InP cladding. The waveguide loss value for TM polarized light around 1550 nm was 4.83 dB/cm with the $In_{0.53}Ga_{0.47}As$ layer removed.

CHAPTER 3: QUANTUM DOT BASED MULTIMODE INTERFERENCE WAVEGUIDING DEVICES USING ELETRICAL CURRENT

Multimode interference (MMI) geometry offers a number of benefits compared to traditional single-mode waveguiding structures for photonic control, such as a very compact device footprint, low polarization sensitivity, large bandwidth and relaxed fabrication tolerances [73, 74]. These properties and the periodic self-imaging effects inherent to MMI structures make them especially relevant for use in optical data processing. Applications include replacing Mach-Zehnder interferometers in channel demultiplexing of optical time domain multiplexed (OTDM) signals, use as components for optical cross-connects [75], or use as power splitters with variable split ratios for planar phased-array wavelength division multiplexing (WDM) components [76]. For the latter application, some 2 x 2 MMI-based designs have utilized complex structural manipulations to produce fixed splitting ratios by altering the phase relations of the underlying modes [77, 78] or resorted to cascading multiple MMI's to achieve similar effects [79]. However these approaches face tighter fabrication tolerances due to the need to precisely define the etching depth and width of their control features. Such devices are unable to compensate for fabrication errors or changes in operational wavelength. Devices that allow for the dynamic control of the power splitting ratio possess a considerable advantage in this regard.

The inclusion of quantum dot (QD) structures as the active material in MMI-based electro-optical switching devices has so far received limited attention. Although a number of active MMI photonic switches have been realized, most have employed multiple quantum wells (MQW) [80] or bulk heterostructure material for device fabrication [81-83], while other designs have been polymer-based and relied on the thermo-optic effect to achieve device control [84,

85]. In many cases, MMI waveguides have been utilized in a purely passive roll, often as input and output couplers for Mach-Zehnder switches [86, 87], with the active portion of the device consisting of the phase shifting arms which connect the two coupler sections. Active MMI devices on the other hand can eliminate the phase shifting arms by incorporating the phase shifting region within the MMI structure [80, 82, 83]. This produces a significantly more compact device [88].

This chapter seeks to describe the theory and properties of MMI-based waveguiding devices, as well as their application to active switches. The design and fabrication of MMI devices for the testing of electro-optical properties in quantum dot materials is presented, along with experimental results. The devices to be discussed are a dynamically tunable power splitter designed around a 3-dB MMI splitter and a tunable 2 x 2 MMI cross coupler. The operation of these devices entails a modification of the refractive index at specific areas within the MMI structure. This alters the phase relations between the excited modes, which allows for control of the waveguide imaging properties and permits switching between the output ports of the device. Devices were designed to utilize current injection at precise points on the MMI surface. The carriers must be kept localized to prevent a reduction in device performance, and carrier spreading is controlled by the placement of narrow trenches around the injection sites. These trenches channel the carriers into the active region and prevent overlap of current into other injection sites.

3.1 MMI Waveguide Theory

When light from a single-mode waveguide is launched into the exact center of a MMI waveguide, numerous modes are excited and begin to interfere with one another. The field profile at any distance *z* along the MMI waveguide is given by Eqn. 3.1, with the shape of the field determined by the field excitation coefficient (c_υ) and the modal phase factor, $\varphi\ (z)$ (Eqn. 3.2). The individual modal field term is represented by $\psi_\upsilon\ (y)$. At precise intervals along the length of the MMI waveguide, the phase relationships between these excited modes are such that exact replicas of the original input signal are formed symmetrically around the central axis of the waveguide (Fig. 3.1 (a)). Both single and multiple images occur at distances defined by the mathematical relations governing multimode interference [74]. For a signal launched off-center into the MMI, the first such occurrence of a single image is reflected across the central axis, forming a cross-coupled image (Fig. 3.1 (b)). This process of image replication in MMI waveguides is called self-imaging.

$$\Psi(y,z) = \sum_{\upsilon=0}^{n-1} c_\upsilon \psi_\upsilon(y)\phi(z) \tag{3.1}$$

$$\phi(z) = e^{\left[j\frac{\upsilon(\upsilon+2)\pi}{3\cdot L_\pi}z\right]} \tag{3.2}$$

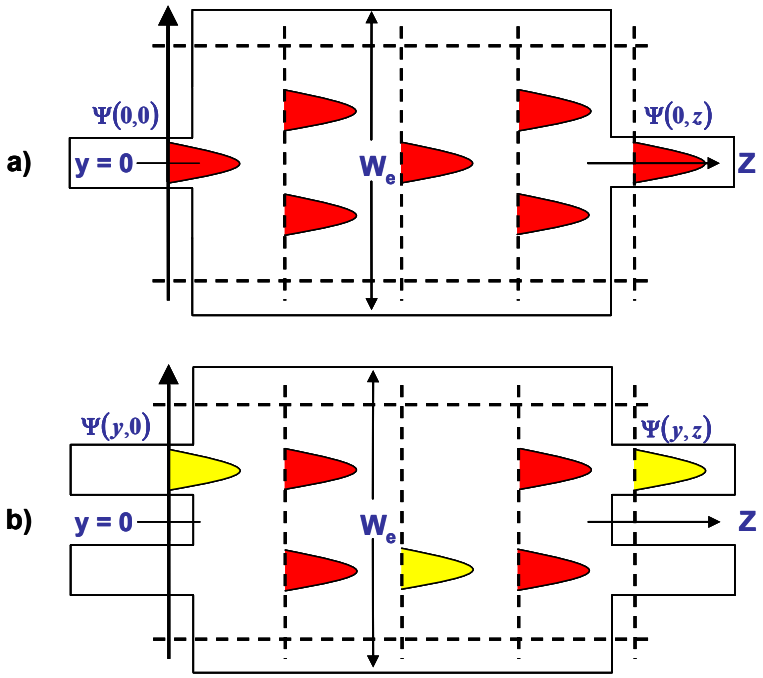

Figure 3.1 Representation of MMI field distribution: a) On-axis launch; b) Off-axis launch.

There are two interference concepts that are pertinent to MMI waveguides: General interference and restricted interference. General Interference concerns those mechanisms which operate independent of the field excitation coefficient (c_υ) and therefore depend only on the modal phase factor. Determining the distance at which an image set forms in this instance requires a relation between the phases of the input field and the resultant image set. Consider that at the input ($z = 0$), the field reduces to Eqn. 3.3. Since an occurrence of a single image at some distance $z = L$ within the waveguide is an exact replica of the input field, we can have the relation shown in Eqn. 3.4.

$$\Psi(y,0) = \sum_{\upsilon=0}^{n-1} c_\upsilon \psi_\upsilon(y) \tag{3.3}$$

$$\sum_{\upsilon=0}^{n-1} c_\upsilon \psi_\upsilon(y) = \sum_{\upsilon=0}^{n-1} c_\upsilon \psi_\upsilon(y) e^{\left[j\frac{\upsilon(\upsilon+2)\pi}{3 \cdot L_\pi} L \right]} \tag{3.4}$$

This relation has two solutions. Both of these are given in Eqn. 3.5.

$$e^{\left[j\frac{\upsilon(\upsilon+2)\pi}{3 \cdot L_\pi} L \right]} = 1 \quad or \quad e^{\left[j\frac{\upsilon(\upsilon+2)\pi}{3 \cdot L_\pi} L \right]} = (-1)^\upsilon \tag{3.5}$$

For the first solution, it can be said that at every distance $z = L$ at which all modes experience an effective 2π phase shift, there exists a direct replica of the input field. Explicitly stated, the phase differences between the interfering modes are identical to that which occurs at the input so the replicated image forms on the same side of the central axis. The second solution indicates that at intervals along z-axis, the guided modes of the MMI waveguide will see a phase difference which will alternate in even and odd multiples of π. For odd multiples of π, even and odd modes will be in phase and anti-phase respectively, which, given the symmetry response of the modal field term (Eqn. 3.6), means that the self-images will be mirrored across $y = 0$ [74].

$$\psi(-y) = \begin{cases} \psi_\upsilon(y) \; for \; \upsilon \; even \\ -\psi_\upsilon(y) \; for \; \upsilon \; odd \end{cases} \tag{3.6}$$

With respect to the relation of modal symmetry in Eqn. 3.7, the two solutions in Eqn. 3.5 will be satisfied at distances $z = L$ as given by Eqn. 3.8, where p is the occurrence of a particular image set and N is the number of duplicate images within the set.

$$\upsilon(\upsilon+2)=\begin{cases}even\ \ for\ \upsilon\ even\\ odd\ \ for\ \upsilon\ odd\end{cases} \tag{3.7}$$

$$L=\frac{p}{N}\left(3L_{\pi}\right)\quad with\quad p\ \geq\ 0\ \ \&\ \ N\ \geq 1 \tag{3.8}$$

Therefore, bar-coupled and cross-coupled single images of the input field will be formed by general interference for even and odd multiples of p when $N = 1$. Multiple images of the input field form when $N \neq p$ and N & P have no common divisor. L_{π} is the beat length between the two lowest order guided modes of the MMI waveguide and relates the distance L to the MMI effective width (W_e), the operational wavelength (λ_o), and the refractive index (n_r) of the guiding layer (Eqn. 3.9).

$$L_{\pi}=\frac{4n_rW_e^2}{3\lambda_o} \tag{3.9}$$

It is important to note however, that the distance at which a particular image set forms can be modified by selective excitation of the guided modes. If an even symmetric field, such as

a Gaussian beam, is launched into a multimode waveguide at the points $y = \pm W_e/6$ as shown in Fig. 3.2, only the first two of every three modes is excited (Eqn. 3.10). This pairing of modes is called restricted paired interference, a particular type of restricted interference, where each even mode leads its associated odd mode by a π phase shift.

$$\upsilon = (0,1), (3,4), (6,7), \ldots \tag{3.10}$$

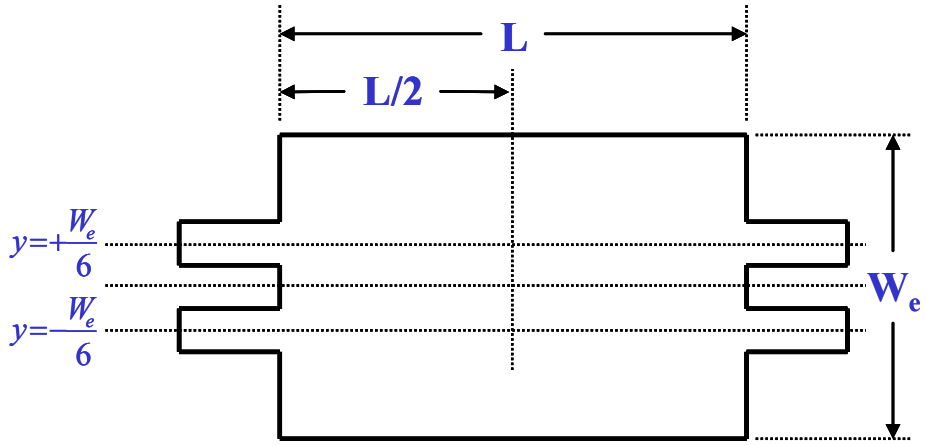

Figure 3.2 Representation of restricted pair interference launch arrangement.

Conversely, the excluded modes $\upsilon = 2, 5, 8\ldots$ present a zero with odd symmetry such that the overlap integral (Eqn. 3.11) between the even symmetric input field and the antisymmetric modal field vanishes, leaving the field excitation coefficient equal to zero for these instances.

$$c_\upsilon = \frac{\int \Psi(y,0)\, \psi_\upsilon(y)\, dy}{\sqrt{\int \psi_\upsilon^2(y)\, dy}} = 0 \tag{3.11}$$

This leads to a reduction in the distance at which a particular image set forms by a factor of 3. For restricted paired interference, the location of input field replicas is given by Eqn. 3.12. Single images of the input field will be formed by restricted paired interference when $p \geq 0$ and $N = 1$, and multiple images form when $p \geq 0$, $N \geq 1$, $N \neq p$ and N & P have no common divisor. This is shown in Fig. 3.3 which depicts the formation of single and two-fold image replicas of the input field at distances L_π & $2L_\pi$ and ½L_π & 3/2L_π respectively.

$$L = \frac{p}{N}\left(L_\pi\right) \quad with \quad p \geq 0 \;\&\; N \geq 1 \tag{3.12}$$

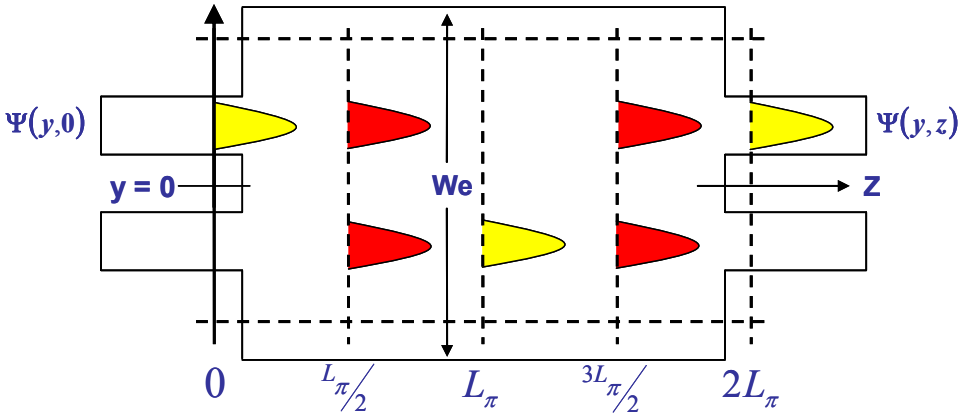

Figure 3.3 Depiction of single and two-fold image formation for restricted paired interference.

3.1.1 Phase Relationships

In order to understand how MMI waveguides can be utilized in the formation of active photonic devices, it is necessary to realize that there exists a defined phase relationship between

the input field and any set of N-images of that input. Moreover, there is a relative phase difference between each image within a particular image set. In the case of an MMI waveguide with N input ports (Fig. 3.4), where a field launched into any input port yields N-images at the output facet, there is a set of equations (Eqn. 3.13 and Eqn. 3.14) which define the phase relationship between the input field and any of the images [73, 74]. Double the MMI length and an intermediate set of N-images now exist halfway between the input ports and the output facet. The phase relations of that intermediate set with respect to both the input field and the output fields could be calculated. Shift the relative phase difference between the members of that intermediate image set, however, and the subsequent imaging characteristics of the MMI are altered.

$$\varphi_{rs} = \frac{\pi}{4N}(s-r)(2N+r-s)+\pi, \quad for\ r+s\ even \tag{3.13}$$

$$\varphi_{rs} = \frac{\pi}{4N}(r+s-1)(2N-r-s+1), \quad for\ r+s\ odd \tag{3.14}$$

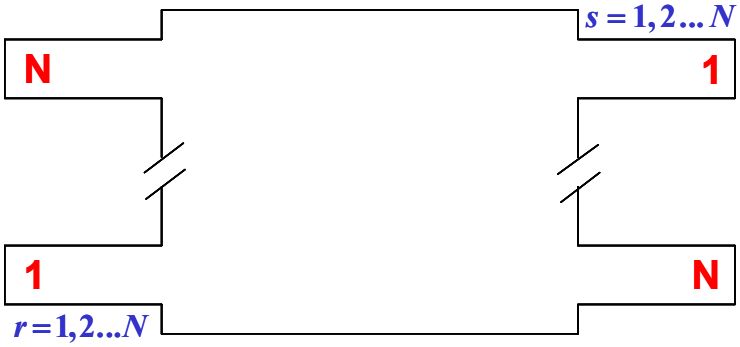

Figure 3.4 N x N MMI waveguide.

By way of example, consider the simulation of a 2 x 2 MMI switch which is shown in Fig. 3.5 (a). This switch is designed such that light launched into the upper input port is imaged to the lower output port, with a two-fold image set located halfway between the input and output ports. The relative phase shift between the input field and the top image in the two-fold set is $\pi/2$, while for the bottom image there is a π phase shift. For the complementary arrangement (Fig. 3.5 (b)), light launched into the lower input port is imaged onto the upper output port. The phase relationship between the input field and the top and bottom images of the two-fold set are reversed, being π and $\pi/2$ respectively. If the phase difference between the two images in Fig 3.5 (a) were altered to be identical to that present in Fig 3.5 (b), then light launched into the upper input port would be imaged to the upper output port. This is shown in Fig. 3.5 (c), when a π-phase shift is selectively induced in the area of the upper image. In essence, it is possible to create an active photonic switch by generating a controlled phase shift at predefined locations within the MMI waveguide.

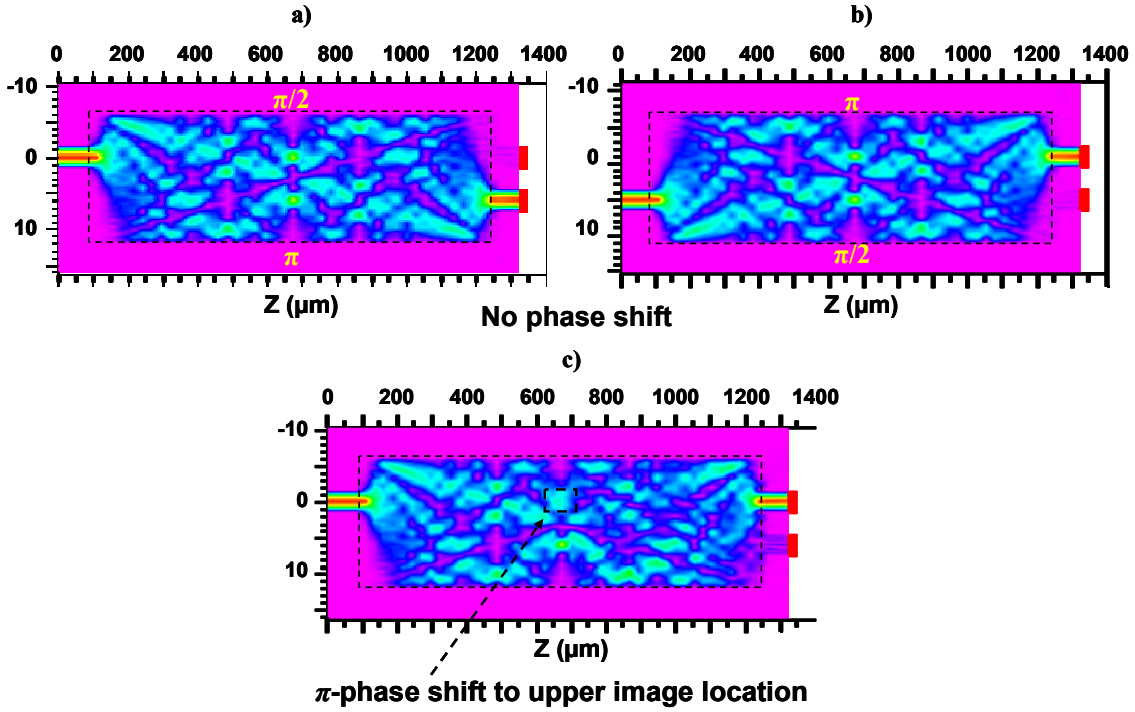

Figure 3.5 Simulation of 2 x 2 MMI light distribution for (a) launch upper input port (b) launch lower input port (c) bar-coupled signal (π phase shift) to upper index modulation zone.

3.2 MMI Based Switches: Design, Operation and Fabrication

This section begins with a discussion on the design and modeling of a half-length device that is based on a 3-dB MMI splitter, but which possesses dynamic tuning capabilities. The device, which shall be called a variable power splitter (VPS), has the potential to fully transfer light back and forth between the output waveguides, permitting a wide variety of splitting ratios. Moreover, the VPS is important in that its geometry and method of operation makes it a useful tool for apprehending certain characteristics of the active material from which it is fabricated, including the polarity of an induced refractive index change. Discussion then shifts to the design

and simulation of a 2 x 2 MMI switching device that operates as a cross-coupler in the off-state, but is also designed to be dynamically tunable, permitting the transfer of light completely from one output port to the other. This is followed by an overview of the fabrication process used to manufacture the two devices, which, aside from the choice of mask patterns, is essentially the same for both. The 2 x 2 MMI cross-coupler and the MMI VPS are both based on generic MMI structures that that have been utilized in both active [80-83] and passive form [77-79] by other authors. However, it is the simplicity and robustness of these formats rather than any claim to uniqueness which make them useful to this work.

The simulation of the device parameters was carried out using BeamProp version 5.0d FD-BPM design software produced by RSoft, Inc. To emulate the active region of the SAQD wafer, the device modeling incorporated a 421 nm thick layer with an average refractive index of 3.437. The upper and lower cladding layers were 1.5 μm thick $Al_{0.35}Ga_{0.65}As$ films with a refractive index of 3.226. The operational wavelength was chosen to be 1310 nm.

3.2.1 Variable Power Splitter with Dynamic Tuning

An MMI-based integrated variable power splitter with dynamic tuning was designed according to the equations for restricted paired interference in multimode waveguides [74]. The foundation for the device is a 3-dB MMI splitter ($p = 1$, $N = 2$), with the relationship between the device length (L_{3dB}) and the effective width (W_e) given in Eqn. 3.12. The device has an MMI length (L_{3dB}) of 575 μm and a width of 18 μm. Light can be launched through either of two 500 μm long input waveguides, symmetric around the MMI's central axis, each of which is 3 μm

wide and have an edge to edge separation of 3 μm. The output waveguides are identical to the input waveguides in dimension and initial separation, though angled so that the separation increases to 6 microns at the end facet. Device operation entails the modification of the refractive index at three particular regions along the midpoint position of the MMI waveguide that are collocated with the first occurrence of a four-fold image of the input ($N = 4$, $p = 1$). A schematic of the device is shown with the top-down view in Fig. 3.6 illustrating the placement of the index modulation regions. The outer two modulation regions are 2 μm wide (W_{ec}) and the inner region is 6 μm wide (W_{ic}), with all three regions having a length of 63 μm.

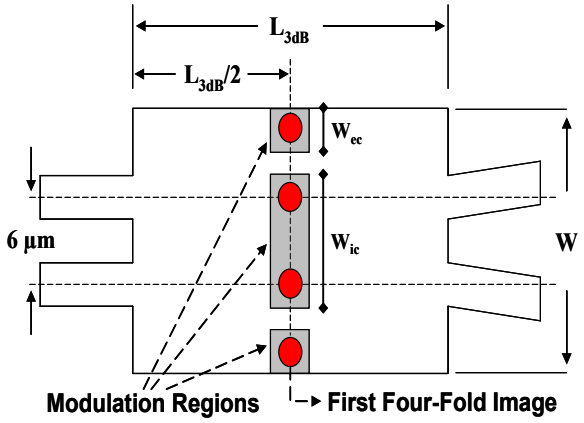

Figure 3.6 Schematic of quantum dot based MMI integrated variable power splitter.

In the off-state, the device acts as a 3-dB power splitter, but by modifying the index at the inner modulation region, the phase relation between the center two self-images and the images at the edges of the MMI is altered. If the phase change is the result of a localized reduction in the refractive index, the power is transferred to the bar output port. Conversely, by effecting a reduction in the refractive index, concurrently, to both edge regions, the power is switched to the

crossed output port. If, instead, the inner modulation region experiences a localized increase in the refractive index, then the phase change is such that the power is transferred to the crossed output port. Likewise, an increase in the refractive index at the outer index modulation regions switches the power to the bar output port. A simulation of the light distribution within the waveguide is shown in Fig. 3.7 (a) with the device in the off-state, operating as a 3-dB splitter, in Fig. 3.7 (b), for a bar-coupled signal and in Fig. 3.7 (c) for a cross-coupled signal, assuming phase changes are the result of localized reductions in the refractive index.

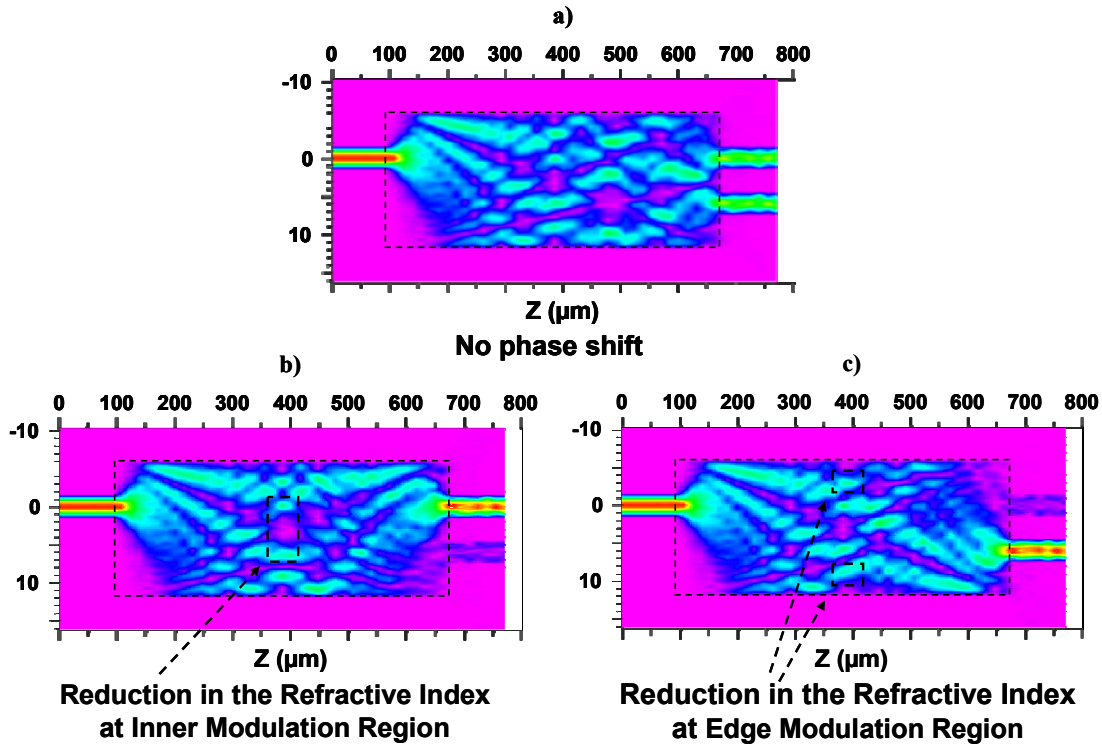

Figure 3.7 Simulation of variable power splitter light distribution for (a) 3-dB state (no phase shift) (b) bar-coupled state (phase shift to inner modulation region) (c) cross-coupled state (phase shift to outer modulation region).

3.2.2 Tunable Integrated 2 x 2 MMI Cross Coupler

The tunable 2 x 2 MMI switch design was also based on the equations for restricted paired interference in multimode waveguides and modeled using BeamProp software produced by RSoft, Inc. The relationship between the device length (L) and the effective width (W_e) are given in Eqn. 3.12. In selecting the cross coupling distance ($p = N = 1$), the device length becomes the same as the MMI beat length (L_π) and the relation reduces to Eqn. 3.9. The width of the device was selected such that the waveguide supported sufficient modes to form a well defined two-fold image of the input centered at $L/2$, with each image bisected by the central axis of one of the two access waveguides (Fig. 3.8).

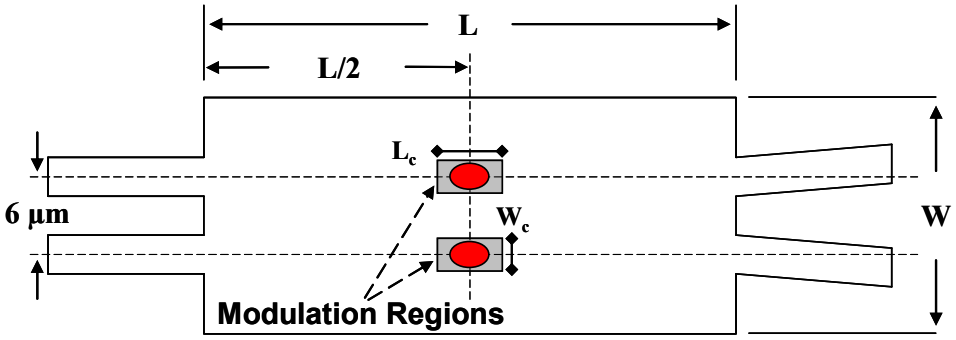

Figure 3.8 Schematic for MMI-based tunable cross-coupler switch.

The device layout consists of a MMI waveguide with a width of W = 18 µm and a length of L = 1175 µm. Light can be launched through either of two 500 µm long input waveguides, symmetric around the MMI's central axis, each of which is 3 µm wide and have an edge to edge separation of 3 µm. The output waveguides are identical to the input waveguides in dimension and initial separation, though angled so that the separation increases to 6 microns at the end

facet. Device operation involves the modification of the refractive index at either one of two specific areas along the midpoint position of the MMI waveguide that are collocated with the first two-fold image of the input ($z = \frac{1}{2}L$). In this way, a change can be induced in the phase relation between these self-images and the formation of any subsequent images is thereby altered, allowing for a signal to be switched between the two output waveguides. A simulation of the light distribution within the waveguide is shown in Fig. 3.9 (a) for a cross-coupled signal (no phase shift) and in Fig. 3.9 (b) for a bar-coupled signal (π phase shift).

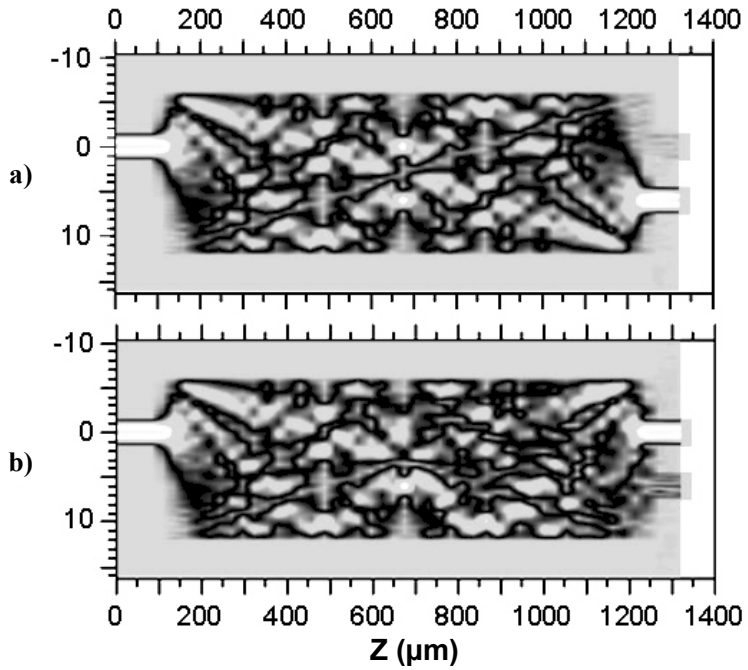

Figure 3.9 Simulation of 2 x 2 MMI light distribution for (a) cross-coupled signal (no phase shift) and (b) bar-coupled signal (π phase shift).

3.2.3 Current Injection and Isolation Trench Depth

The two MMI devices described in sections 3.2.1 and 3.2.2 were designed to use current injection to generate the necessary phase shifts. This was done so as to access the carrier induced change in refractive index properties of semiconductors. The refractive index of the semiconductor material is reduced through the band-filling and plasma effects in the presence of free carriers [23]. Since both the 2 x 2 cross coupler and the variable power splitter are designed to operate with current being injected into only one index modulation region at a time, current isolation is required to prevent these carriers from spreading to other injection sites. A similar index modification occurring in both regions would partially cancel out the desired phase shift and degrade the overall device performance. Approaches were restricted by the p-type doping of the upper cladding layer, so the utility of some current isolation techniques, such as zinc in-diffusion [89] and ion implantation, was limited. Current isolation was therefore achieved through the creation of 2 μm wide trenches surrounding each of the index modulation regions. While a narrower trench width was well within the functional limitations of contact photolithography, 2 μm was chosen for ease of fabrication.

The depth of the isolation trenches was used as a means for controlling the degree of current spreading. Maintaining the trench depth at less than the thickness of the upper cladding and permitting a small amount of carrier spreading, allows for a more robust device that is less susceptible to fabrication errors [90]. For the tunable cross coupler, electrical current could be injected through either one of two Ti/Au/Zn/Au contact stripes which overlapped the index modulation regions. The index modulation regions (and contacts) were 51 μm long and the optimum width was determined to be 3 μm (Table 3.1). In the case of the variable power splitter,

current could be injected into either the central contact or else injected, concurrently, into to the two edge contacts. The final design dimensions for the variable power splitter are shown in Table 3.2.

Table 3.1 2 x 2 MMI: Final design dimensions.

Optimum Dimensions – BeamPROP BPM Modeling	
Parameter	Dimension (μm)
MMI Length	1150
MMI Width	18
Waveguide Height	2.2
Isolation Trench Depth	1.45
Modulation Region Width	3
Modulation Region Length	51

With the addition of these trench structures to the BeamPROP model, there was a slight change in the optimum device length due to localized, but axially symmetric changes to the effective refractive index at the controlling image locations. More importantly, the model suggested that precise control of the trench depth was critical to device performance. While trenches that are too shallow will allow current to spread into other index modulation zones, thereby reducing the switching range of the device, trenches which are too deep will produce a loss in throughput intensity (Fig. 3.10). A depth of 1.45 μm was chosen as only slight transmission loss was predicted, while placing the bottom of the trench at 250 nm above the active region, minimizing current spreading. Losses related to isolation trench depth were

calculated for a depth of 1.45 μm to be only 0.25 dB for TE transmission, while at the presumed waveguide depth (2.2 μm), the losses were calculated to be 12 dB.

Table 3.2 Variable power splitter: Final design dimensions.

Optimum Dimensions – BeamPROP BPM Modeling	
Parameter	Dimension (μm)
MMI Length	575
MMI Width	18
Waveguide Height	2.2
Isolation Trench Depth	1.45
Outer Modulation Region Width	2
Center Modulation Region Width	6
Modulation Region Length	63

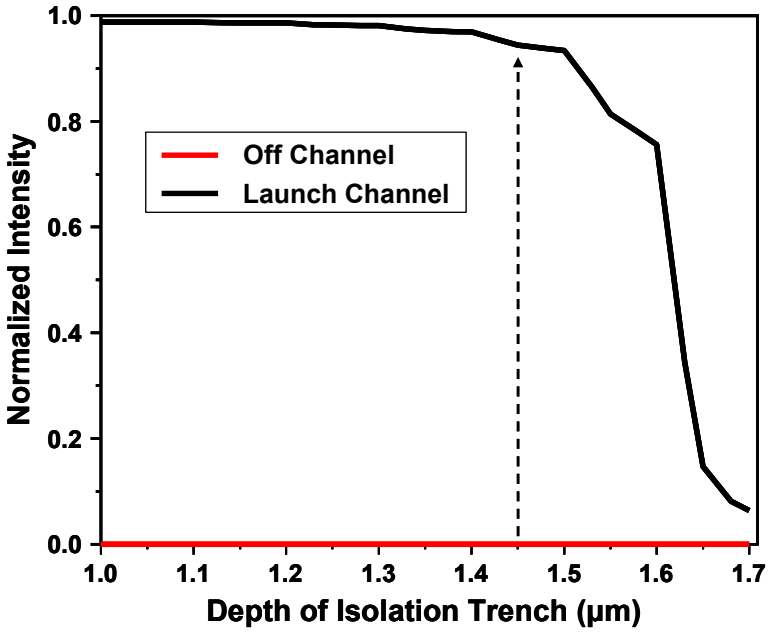

Figure 3.10 Normalized throughput intensity versus depth of isolation trenches. Dashed line indicates chosen trench depth.

3.2.4 MMI Device Fabrication

The devices were designed to operate using current injection in order to further study the electro-optical properties of the SAQD material. In this section, the fabrication processes for both the variable power splitter and the 2 x 2 cross coupler are detailed. The mask patterns were designed and then ordered from Benchmark Technologies. The fabrication steps taken were identical for the MMI variable power splitter and the tunable 2 x 2 cross coupler. Each parameter was the same, including the exposure and developing times in the photolithographic steps. Only the mask patterns employed differed.

3.2.4.1 Fabrication for Current Injection Control

Prior to device fabrication, the QD wafer sample is soaked in acetone and agitated by means of a sonic bath to degrease the surface and remove any particulates adhering to the wafer which might interfere with the fidelity of the pattern transfer. The sample is then rinsed with a sequence of acetone, methanol and isopropanol and dried with nitrogen gas. Native oxide is removed by soaking the wafer sample in a buffered oxide etch solution (BOE) for 5 minutes and thoroughly rinsing the sample in DI water. The wafer is dried with nitrogen gas and baked at 120°C for 2 minutes to remove any residual volatiles.

Fabrication began with the growth of 400 nm of silicon dioxide (SiO_2) on the surface of the QD wafer sample by means of plasma enhanced chemical vapor deposition (PECVD). Contact photolithography with Futurrex NR7-1000PY negative photo-resist was used to pattern the isolation trenches (Table 3.3) which were etched into the SiO_2 with a CF_4-based reactive ion etching (RIE) process (Table 2.1). The pattern is then transferred to the QD wafer employing a BCl_3-based etching process (Table 3.4) and a UNIAXIS ICP-RIE III-V reactor to a depth of 1.45 μm. Any remaining SiO_2 was removed through immersion in BOE. A benzocyclobutene polymer (BCB) was used to planarize the surface and a new 400 nm layer of PECVD SiO_2 was grown. The device waveguides were patterned on the dielectric surface using contact photolithography (Table 3.5) followed by metal deposition a 100 nm layer of chromium using an Edwards FL 400 thermal evaporator, and liftoff of the extraneous metal in acetone. The chromium acts as the etch mask for the SiO_2 layer, the uncovered portion of which is etched using the same CF_4 RIE process as before (Table 2.1). The pattern is then transferred into the wafer with the BCl_3 etching process. In order to maintain a sufficient number of confined modes

and reduce polarization sensitivity, the waveguides were etched completely through the active region and into the lower cladding. The overall depth from the wafer surface was 2.2 μm. All residual chromium and SiO_2 were removed with BOE immersion.

Table 3.3 Photolithographic process for current isolation trench formation.

Photolithographic Process Steps for Trench Formation	
Spin Photo-Resist (Futurrex NR7-1000PY)	4000 rpm / 50 sec.
Pre-Bake	150°C / 1 min.
UV Exposure	12 mW/cm^2 / 10 sec.
Hard Bake	100°C / 2 min
Developer (Futurrex RD-6)	14 sec.
Oxygen Plasma	40 sec.

Table 3.4 BCl_3-based ICP/ RIE etching process.

BCl_3-Based ICP/RIE Process	
BCl_3 Flow	7 sccms
Ar_2 Flow	18 sccms
Residual Pressure	10 mT
ICP Power	600 W
RF Power	40 W
GaAs/AlGaAs Etch Rate	270 nm/min

Table 3.5 Photolithographic process for metal liftoff.

Photolithographic Process Steps for Metal Liftoff	
Spin Photo-Resist (Futurrex NR7-1000PY)	4000 rpm / 50 sec.
Pre-Bake	150°C / 1 min.
UV Exposure	12 mW/cm^2 / 11 sec.
Hard Bake	100°C / 2 min
Developer (Futurrex RD-6)	14 sec.
Oxygen Plasma	40 sec.
UV Post Exposure	11 sec.
Post Bake	120°C / 2 min

Mesas were created in the same lithographic step as the waveguides to act as foundations for the eventual placement of contact pads. Situated on either side of the MMI, the mesas were separated from the waveguides by several microns. BCB polymer was used as a planarization material to provide a continuous surface for bridging between the contacts and contact pads. Afterward, a 200 nm PECVD silicon nitride (Si_3N_4) layer was grown to ensure electrical isolation. Windows for the contacts were opened in the Si_3N_4 layer with contact photolithography and a separate CF-based RIE process designed for the etching of Si_3N (Table 2.2). P-type Ti/Au/Zn/Au contact stripes and pads were then created using contact lithography followed by metal deposition and liftoff. The sample was annealed inside a rapid thermal annealing furnace for 1 minute at 400°C to anneal-in the contacts. With the contact pads as a mask, the uncovered Si_3N_4 and BCB films were removed by an oxygen-based RIE process with a 30% mixture of CF_4 (Table 3.6). Finally, the substrate side of the sample was lapped down to a

thickness of 120 µm and polished to a mirror finish. Ni/Ge/Au n-type contacts were deposited on the back side using thermal evaporation and annealed-in at 400°C for 2 minutes. The device was then cleaved and mounted on a copper header for testing. A composite photograph of a completed 2 x 2 tunable cross coupler device is shown in Fig. 3.11.

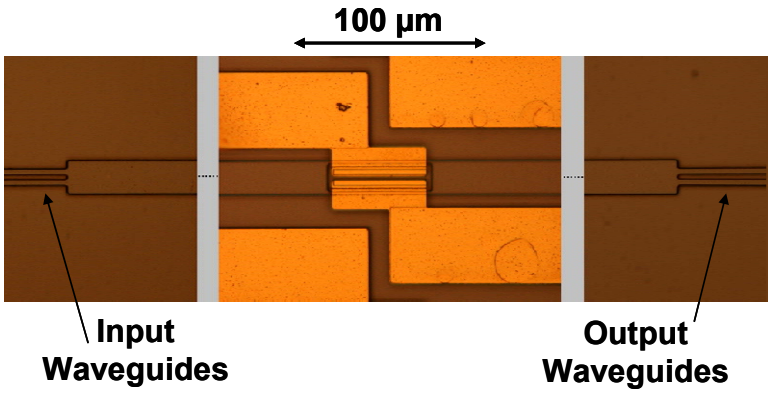

Figure 3.11 Photo of a completed 2 x 2 MMI cross-coupler switch.

Table 3.6 Benzocyclobutene polymer CF_4-based etching process.

Benzocyclobutene Polymer Etching Process	
CF_4 Flow	5 sccm
O_2 Flow	10 sccm
Residual Pressure	50 mT
RF Power	100 W
BCB Etch Rate	156 nm/min

3.3 Experimental Setup

3.3.1 Experimental Setup for Sub-Microsecond Time Scales

The experimental setup depicted in Fig. 3.12 was utilized for testing the MMI variable power splitter in order to determine the extent of the carrier induced effects in the InGaAs/GaAs SAQD material, and its application to the fabrication of MMI switching devices. Testing was done using sub-microsecond current pulses and a CW light source. Light was emitted from a fiber pigtailed laser diode operating at a wavelength of 1310 nm. The beam then passed through a lithium niobate modulator and then through a fiber polarization controller to allow selection of either TE or TM polarized light (TE parallel to the active layer and TM perpendicular). From the polarizer, the optical beam was then sent into a SMF-28 lensed fiber and end-fire coupled into the input port of the variable power splitter. Light from the output facet was collected by a matching lensed fiber and passed through a semiconductor optical amplifier (SOA) to enhance the signal. Finally the signal passed to an InGaAs photodetector (Thorlabs PDA-255A) and the data was gathered with a HP 83480A digital communications analyzer. A narrow band fiber Bragg grating filter, placed between the SOA and the photodetector, was used to remove the amplifier noise. Electrical current injection was supplied by a Phillips PM5712 pulse generator.

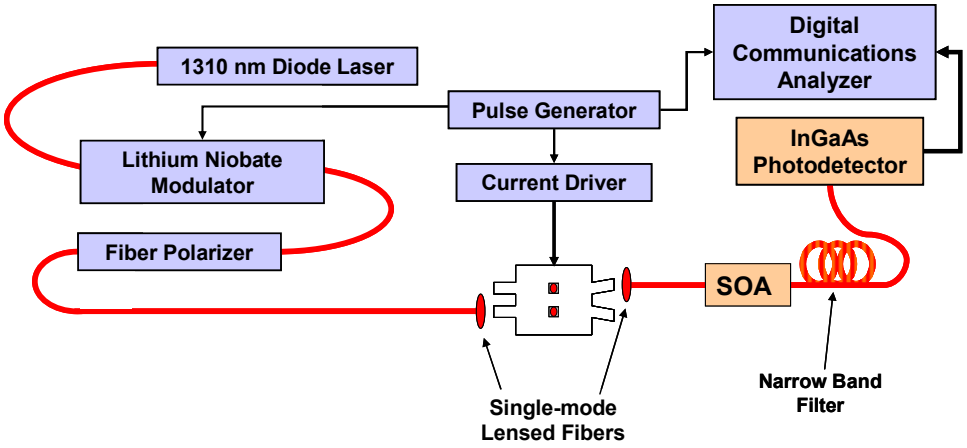

Figure 3.12 Experimental setup for pulsed and CW testing of MMI waveguide devices.

3.3.2 Experimental Setup for Device Switching

Device testing could be done using either CW light with DC current, or using both pulsed current and optical signal. The experimental setup is depicted in Fig. 3.13. Light from a fiber pigtailed laser operating at a wavelength of 1.31 μm was sent through a lithium niobate modulator and then collimated by a fiber collimator. A fiber-based polarization controller was positioned between the modulator and collimator allowing selection of either TE or TM polarized light. The optical beam was then end-fire coupled into the input waveguide using a 40x microscope objective. The device output facet was imaged onto an infrared camera (MicronViewer 7290A) using a second 40x microscope objective while a beam splitter placed before the CCD camera allowed measurement of the transmitted signal using an InGaAs photodetector (Thorlabs PDA-255A). Electrical current injection is supplied either by a Keithley 2400 source meter for DC current testing or by a Philips PM5712 pulse generator during pulsed

operation. Data was gathered from a TDS2012 Tektronix oscilloscope using a Labview 7.0 based data acquisition program.

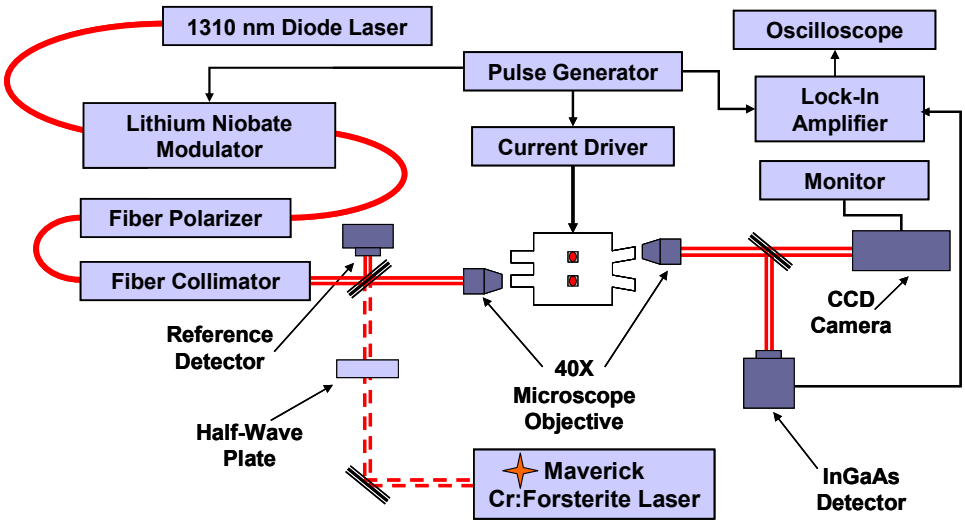

Figure 3.13 Experimental setup for pulsed and CW testing of MMI waveguide devices. The dashed lines represent the alternative beam path when the Cr:Forsterite laser is used.

The device could also be probed near the bandedge of the QD's, using a Mavericks tunable Cr:Forsterite laser operating over a range of 1240 nm to 1280 nm. Since this laser was not fiber coupled, the testing setup was slightly modified to accommodate the new laser, with a half-wave plate used to alter the polarization of the injected laser light. The dashed line in Fig. 3.13, passing from the Cr:Forsterite laser to the beam splitter, shows the alternate beam path that exists when that laser was in use.

3.4 Current Injection: Carrier versus Thermal Nonlinearities

In section 2.1.4.3, analysis of current injection into a ridge waveguide, using CW light and dc current, suggested that the carrier induced changes to the refractive index saturated at a relatively low current density. Moreover, the evidence indicates that the index change due to thermal nonlinearities could grow large enough to overwhelm the carrier induced effects as the current density was increased. As noted in that section, the refractive index change for the two effects is of opposite sign in semiconductor materials, with carrier injection resulting in a reduction in the refractive index while the thermo-optic effect produces an increase in the refractive index. The MMI variable power splitter (VPS) is a convenient tool for investigating the extent of each of these effects as the device's response differs depending on the polarity of the refractive index change at the index modulation regions. Fig. 3.14 (a) shows a simulation of the VPS in the off-state, with no phase change induced at either of the index modulation regions, and thus functioning as a 3-dB splitter. Fig. 3.14 (b), on the other hand, simulates the results of a negative refractive index change at the center contact (light shifts toward the bar port) and Fig. 3.14 (c) simulates the results of a positive index change at the same contact (light shifts toward the crossed port). Consequently, an electrical current pulse applied to the center contact will produce an up-pulse at the bar output port for carrier induced nonlinearities and a down-pulse for thermal nonlinearities.

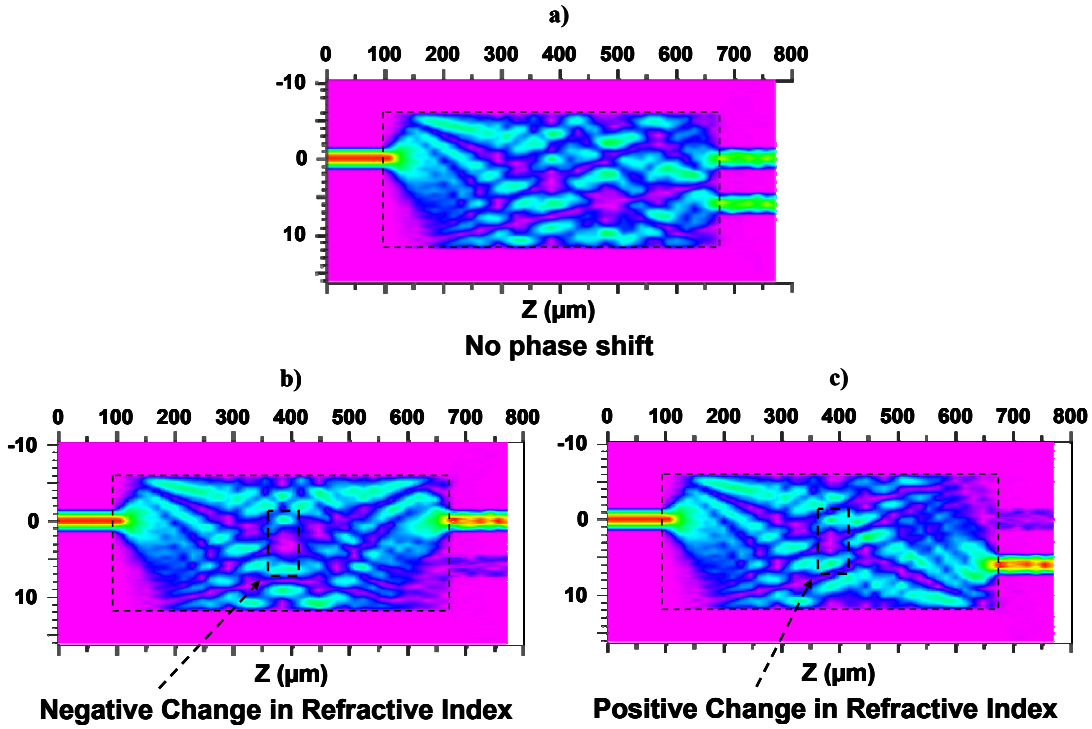

Figure 3.14 Polarity of refractive index change with (a) 3-dB state (no phase shift) (b) reduction in refractive index at inner modulation region (bar-coupled state) (c) increase in refractive index at inner modulation region (cross-coupled state).

Testing was carried out using the experimental setup in section 3.3.1. A sub-microsecond electrical pulse was used to probe the device response to current injection at one of the two index modulation regions. In the first test, the change in transmission at the device's two output ports was measured while a 250 ns current pulse was applied to the contact pad connected to the inner index modulation region. Starting with an applied current of 200 µA, the level was increased in steps of 200 µA up to 3.0 mA while TE polarized CW light at a wavelength of 1310 nm was launched into the right-hand input port. The results are shown in Fig. 3.15 (a) for the bar output port, and Fig. 3.15 (b) for the crossed output port. Similar results were seen for the left-hand input port.

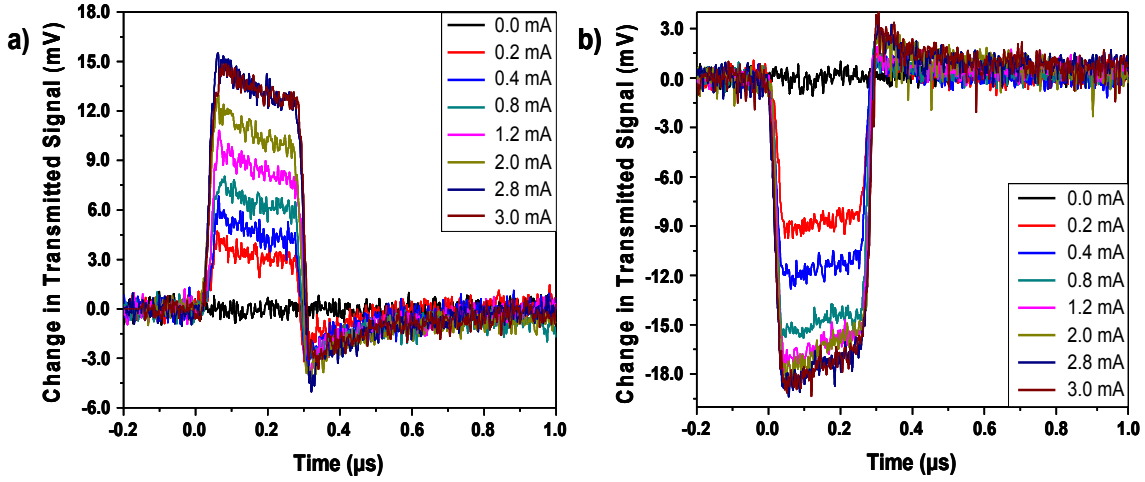

Figure 3.15 Carrier induced change in transmission for the variable power splitter with current applied to the inner modulation region. Measurements taken at the (a) bar output port and (b) crossed output port. Vertical axes cover the same range for (a) and (b).

It can be seen that the carrier induced change in the refractive index saturates rapidly, with the largest change in the transmission occurring with the application of the first 200 µA of current (52.9 A/cm^2). The rate of the change in transmission then drops with increasing current, and the carrier induced change saturates at approximately 2.8 mA of applied current (740.7 A/cm^2). As anticipated for a reduction in the refractive index at the center modulation region, light is shifted from the crossed output port to the bar output port. In each tested VPS device on the wafer sample, differences were seen in the magnitude of the transmission change measured at the crossed versus the bar output ports for a given change in the applied current. These differences are attributed to errors that accrued during fabrication. Contributions by electroluminescence were determined to be negligible.

Interestingly, as the applied current increases, the pulse profile begins to distort, with the pulse floor (or ceiling) beginning to slope in the direction opposite the carrier induced transmission change. This is the beginning of a thermal response, which, due to the opposite change imparted on the refractive index by the thermo-optic effect, transfers the light to the crossed output port. The distortion indicates that the conflict between the two forces is occurring even during the extent of the current pulse (250 ns). When the current pulse ends, the transmission does not return to the pre-pulse level immediately. Rather an overshoot is observed, with the amount of overshoot initially corresponding to the degree that the carrier induced response was distorted by the thermal response. The rise and recovery times of the carrier induced switching event are clearly on the order of nanoseconds, matching the expectation that they be proportional to the carrier lifetime and limited only by the rise and fall times of the electrical control pulse (~ 20 ns). However, the recovery time for the overshoot, as determined by an exponential fit to the decay curve, is approximately 200 ns, and is therefore much longer than the carrier lifetime. This adds support to the idea that the pulse distortion and post-pulse overshoot are due to the buildup of thermal energy from current injection at the inner modulation region.

In order to determine the extent to which the carrier induced change in the refractive index affects the transmission at the output ports, as well as the efficacy of the quantum dot material for fabricating MMI-based electro-optical switches, the change in the device transmission at the two output ports must be compared to the dc transmission levels. The normalized throughput intensity for the VPS output ports, including the dc level, is shown in Fig.

3.16. Though the off-state splitting ratio is not fully 3-dB, it is clear that the degree of switching is insufficient for most applications involving active MMI's.

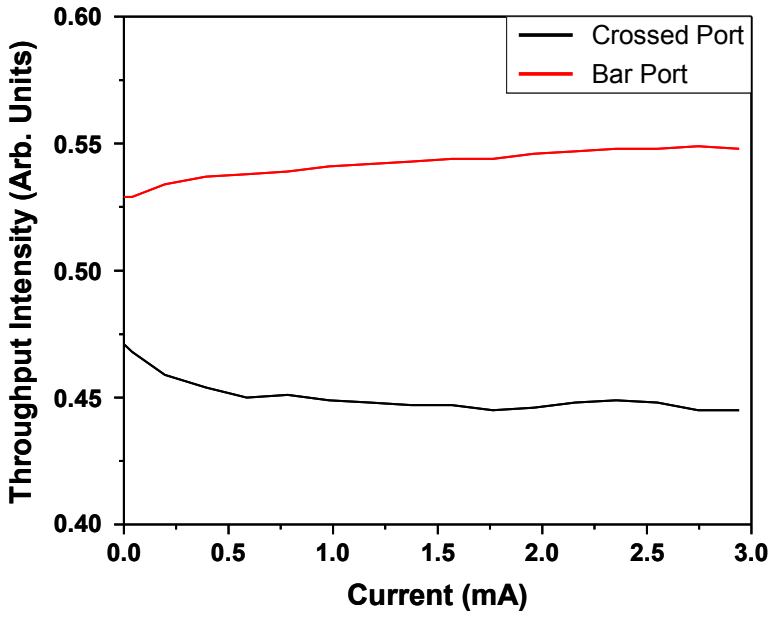

Figure 3.16 Plot of normalized throughput intensity for the variable power splitter.

Increasing the value of the applied current beyond 3 mA further distorts the signal pulse, with the degree of overshoot that occurs at the termination of the electrical pulse continuing to grow in magnitude. The carrier induced change in the transmission is eventually dominated by the opposing thermal response as current levels exceed 8 mA (2.12×10^3 A/cm^2). The overshoot recovery now appears to consist of two components, a sharp, fast initial response, and then a much slower, gradual relaxation back to the pre-pulse level (Fig. 3.17). When a double exponential decay is fitted to the curve, the initial recovery time is about 62 ns. The relaxation time of the slower component is about 991 ns. The presence of these two components can be explained by considering that the current isolation trench is not only a barrier to the injected

current, but also to the thermal energy produced by that current. Whether the thermal energy is generated near the surface as would be the case with a resistance heater, or whether the thermal change is produced deep inside the epitaxial structure, the trench acts to concentrate the thermal energy, creating a temperature gradient with the maximum temperature change centered directly below the inner contact. Move away from that central position and the magnitude of the temperature change should drop rapidly as the accessible volume of the material increases. The degree that the refractive index changes with the change in temperature is given by $\Delta n = \Delta T(dn/dT)$, thus Δn also rapidly drops as the distance from the center of the contact location increases. When the current pulse is terminated, so is the source of the thermal change and the slope of the gradient is quickly reduced as the temperature begins to equalize due to the high thermal conductivity of the semiconductor material. This corresponds to the fast component of the recovery curve. The more gradual decay in the transmission change is associated with the remaining thermal energy being dispersed into the substrate as the temperature returns to the background level.

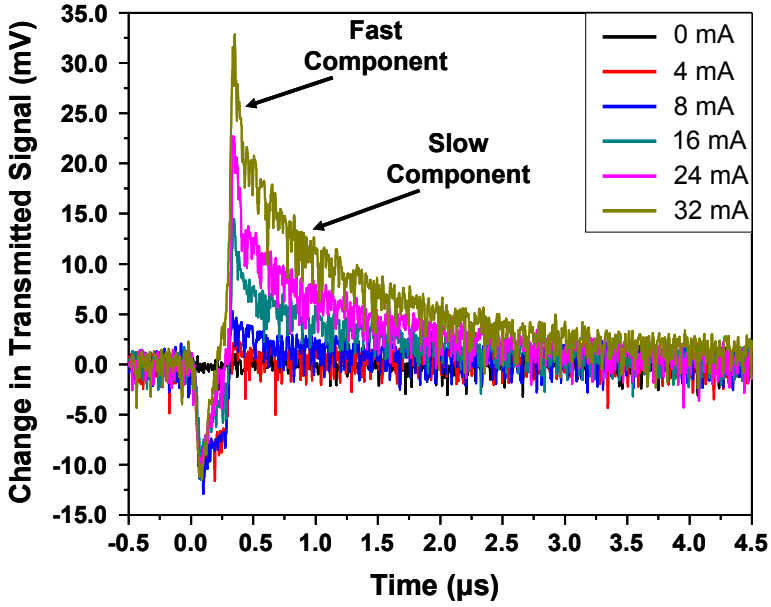

Figure 3.17 Change in the transmitted signal for the variable power splitter measure at the crossed output port to selected values of injected current at the inner modulation region.

In order to better understand the consequences of the current isolation trenches which bordered the index modulation regions, additional devices were built that were essentially identical in all dimensions, but lacked the presence of these trenches. Electrical current pulses, with a width of 300 ns, were applied to the inner contact. The change in transmission at the output ports of these new devices was monitored as the applied current was changed from 0 mA to 32 mA in 8 mA increments (Fig. 3.18).

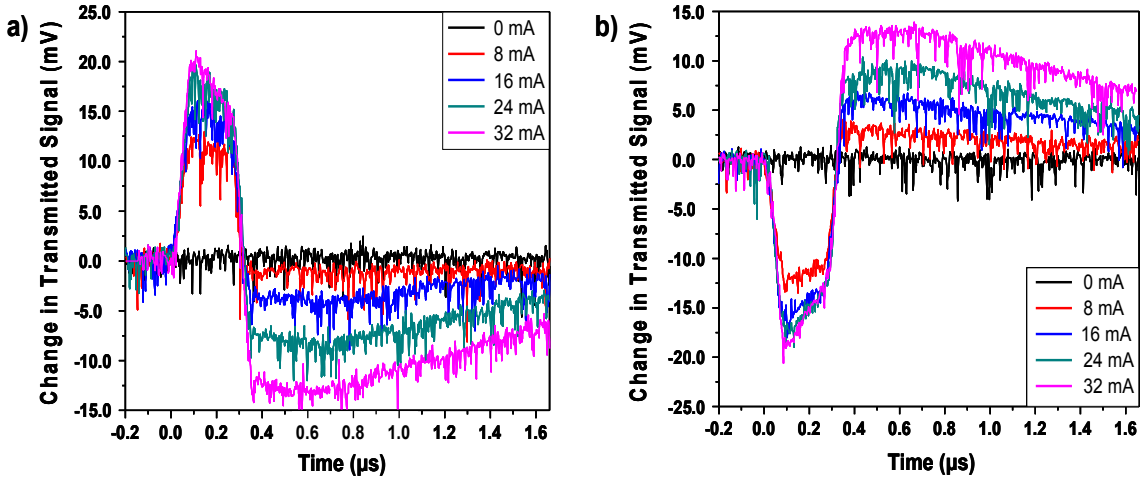

Figure 3.18 Variable power splitter without current isolation trenches with (a) bar output port and (b) crossed output port.

For these devices, the carrier induced effects saturated at a much higher level of applied current which was expected as the lack of confinement allows the carriers to diffuse laterally, lowering the overall current density in the index modulation regions. The carrier induced change in the refractive index produces no more switching range in these devices than in the devices that had current confinement trenches. Pulse distortion due to the buildup of thermal energy is also reduced since the temperature gradient is no longer as sharp for a given applied current. Even without the current isolation trenches the magnitude of the thermal response is comparable and the recovery time is still on the order of 1 µs. However, without the current isolation trench, there is no fast component to the thermal overshoot, instead the thermal response plateaus for approximately 400 ns before gradually decaying back to the pre-pulse level.

3.4.1 Discussion

With respect to device operation, the rapid saturation of the carrier induced nonlinearities in SAQD posses a problem for MMI device application. The phase shift necessary for switching requires a much longer interaction distance than is available in MMI structures, where it is set by the length of the images created through the self-imaging process. Additionally, there is the accompanying thermal response at high current values which began to work against the current induced response, distorting the pulse profile and washing out the signal even for sub-microsecond current pulses. Increasing the duration of the current pulses further allows for an even larger buildup in the thermal energy. As an example, a 32 mA (8.47×10^3 A/cm$_2$) pulse was applied to the VPS fitted with current isolation trenches, and measurements were taken as the duration of the pulse was increased in increments of 100 ns, from 300 ns to 1 μs. The plots in Fig. 3.19 (a) and Fig. 3.19 (b) show that while the carrier induced change in the refractive index has saturated, the thermal response has not, and is currently limited by the duration of the electrical pulse rather than the amount of applied current. There is little variation in the response times as the electrical pulse duration increases, with the rise time averaging around 900 ns and the slow component of the recovery time averaging about 1.2 μs. If an electrical pulse with a greater width is applied (60 μs), such that the thermal change in the refractive index has saturated, then the true rise and recovery times can be measured. Using an exponential fit to the curves in Fig. 3.20, these times are determined to be 920 ns and 1.63 μs respectively, which are quite close to times measured for the sub-microsecond current pulses.

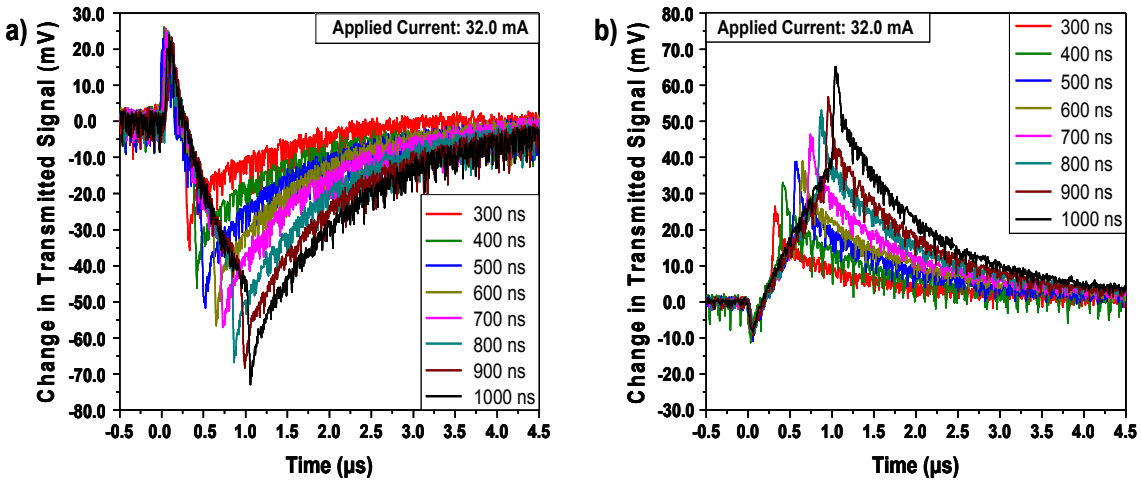

Figure 3.19 Response of the variable power splitter to increases in electrical pulse duration as applied to the inner modulation region and measured at (a) the bar output port and (b) the crossed output port.

Therefore, while the prospects for MMI switches operating through electrical current injection are limited, there is the option of employing them as thermo-optic devices. A number of active MMI photonic switches have relied on the thermo-optic effect to achieve device control. Many of these were fabricated from polymers [85, 91] or polymer-silica hybrids [92-94]. The use of III-V semiconductors on the other hand allows for ease of integration into more complex device structures that also contain active components such as laser diodes, semiconductor optical amplifiers, and photodiodes. III-V semiconductors are also typically more resistant to environmental extremes such as temperature and pressure, and can operate at higher power levels than polymer based devices. Compared to silica based dielectrics, III-V semiconductors possess a thermo-optic coefficient ($dn/dT \approx 2.5 \times 10^{-4}/°K$) that is an order of magnitude greater, resulting in a larger change in the refractive index [95]. The higher thermal conductivity of semiconductors materials, an order of magnitude larger than either polymers or silica [91, 95],

also results in a faster device response time and a shorter recovery time. Sections 3.5 and 3.6 will illustrate the VPS and the 2 x 2 MMI cross-coupler as functional thermo-optic switches.

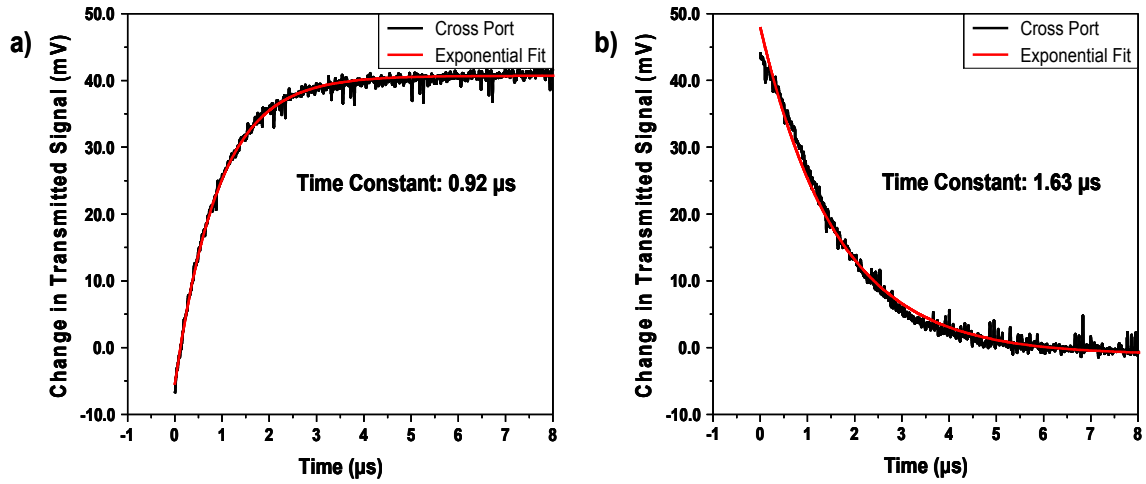

Figure 3.20 Determination of the thermal rise and fall times for a 60 μs duration pulse of 32 mA is applied to the center contact of a variable power splitter with current isolation trenches. Measurements at the cross output port showing the (a) response and (b) recovery curves.

3.5 MMI-Based Variable Power Splitter

The device was tested using the experimental setup shown in Fig. 3.13 with dc current and CW light. Measurements were taken using the Mavericks Cr:Forsterite laser operating at a wavelength of 1262 nm with the light TE polarized. The results are shown in Fig. 3.21. First, it should be noted that, in the absence of any applied current, the device did not exhibit true 3-dB power division. This discrepancy is presumed to be due to simple manufacturing errors which introduced an asymmetry into the device structure. However it was easily corrected to a 50-50 power split by applying 4.3 mA to the inner contact. With additional current applied to the inner contact, the device was continuously tunable to a 1:8 splitting ratio at 28 mA. When current was

applied to the contact pad connected to the outer modulation region contacts, the power splitting ratio was tunable to 11:1 over a range of 0 mA to 28 mA.

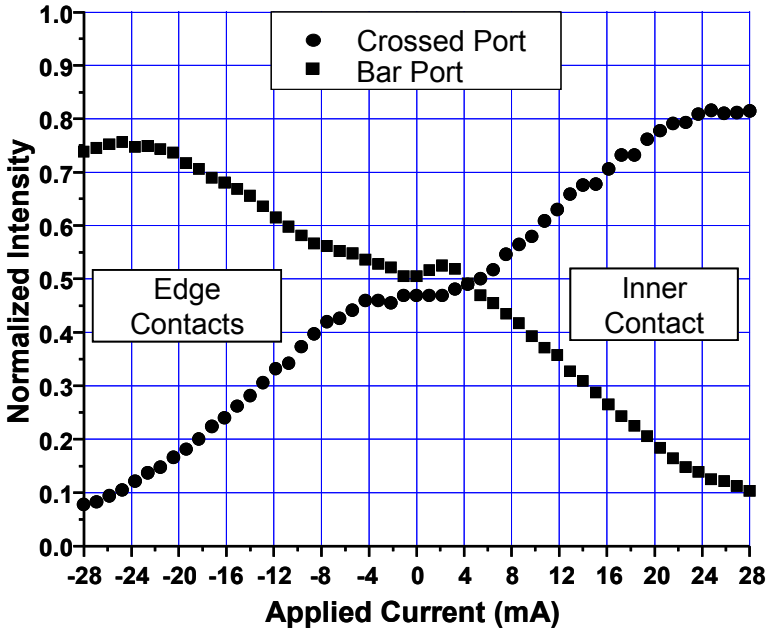

Figure 3.21 Measured tuning response of quantum dot based integrated variable power splitter at $\lambda = 1262$ nm for TE polarization.

Unsurprisingly, comparing the results in Fig. 3.21, with the simulation of the variable power splitter in Fig. 3.7, makes it is immediately clear that the device behaves in a manner which is consistent with an operational nonlinearity that is thermo-optic in nature. This was anticipated from the examining the competing thermal and carrier induced effects in section 3.4. Interestingly, the device response over the range from 0 mA to approximately 3 mA (for either contact) suggests an attempt to switch as predicted for carrier based nonlinearities. However, even if that is the case, the effect is quickly overwhelmed by the thermal response at higher current levels.

As a thermo-optic device, the VPS exhibits a tuning range suitable for use in diversified applications. The tuning capabilities not only allow for correction of the splitting ratio, improving the device tolerance to fabrication errors, but also for real-time correction to counter environmental effects, including external temperature fluctuations. It is hypothesized that the device performance can be enhanced by improving the isolation between the index modulation regions to prevent changes to refractive index from extending to encompass the self-images associated with nearby modulation regions. In the VPS, the modulation regions are placed much closer together than is the case with the corresponding regions of the 2 x 2 MMI cross-coupler switching device, which also exhibits a much broader switching range as will be shown in section 3.6. The simplest way to test this idea would be to construct a larger version of the VPS in which the index modulation regions would be positioned at greater distances from each other due to matters of scale.

3.6 Tunable 2 x 2 MMI Cross Coupler

Testing was carried out with both pulsed current and dc current. However, while switching was attainable with dc current, a measureable degradation of the device switching range was observed at higher current values when compared to pulsed operation. This degradation was attributed to a thermal buildup in the area around the index modulation regions, beyond what could be drawn off by the substrate. This heating appeared to be influencing the structure in a near uniform manner, altering the device effective length and consequently the distance at which output signal was imaged. As such, the majority of measurements were taken

with pulsed current and light using the experimental setup shown in Fig. 3.13. The pulse period was 1.4 ms, with the electrical pulse width set to 50 μs and the width of the light pulse to 30 μs. These values were sufficient to eliminate the unwanted heating effects noted during dc current operation. When probing the device with a 1.31 μm wavelength DFB laser, the optimum splitting ratio for the crossed-coupled state occurred at a non-zero current value for the TE polarized light, with a ratio of 1:29 at 2.9 mA. For TM polarization the off-state splitting ratio was 1:48. With the application of current through either one of the electrodes, the power splitting ratio was continuously adjustable to a 49:1 split ratio with a current of 26.8 mA for TE polarization and a 38:1 split ratio at a current of 25.7 mA for TM polarization. A 50:50 split ratio was reached at a value of 17 mA for both polarizations. Full switching crosstalk values better than -15 dB were achieved in both cases, with -16.9 dB for TE and -15.8 dB for TM. The device switching response is shown in Figs. 3.22 and 3.23 for TE and TM polarization respectively. Same channel extinction was also measured at each output port. For TE polarization, the crossed port extinction was -16.7 dB and the bar port extinction was -14.7 dB. TM polarization yielded a crossed port extinction of -15.8 dB and a bar port extinction of -16.8 dB. The insertion losses of the device were measured for both polarizations at 1310 nm, and, when surface reflections for input and output facets were taken into account, were found to be 9.3 dB (TE) and 8.6 dB (TM). As per design, current can be applied to either contact, though only one contact is employed at a time. The device was observed to be highly symmetrical in response, and nearly identical results were obtained regardless of which contact was used.

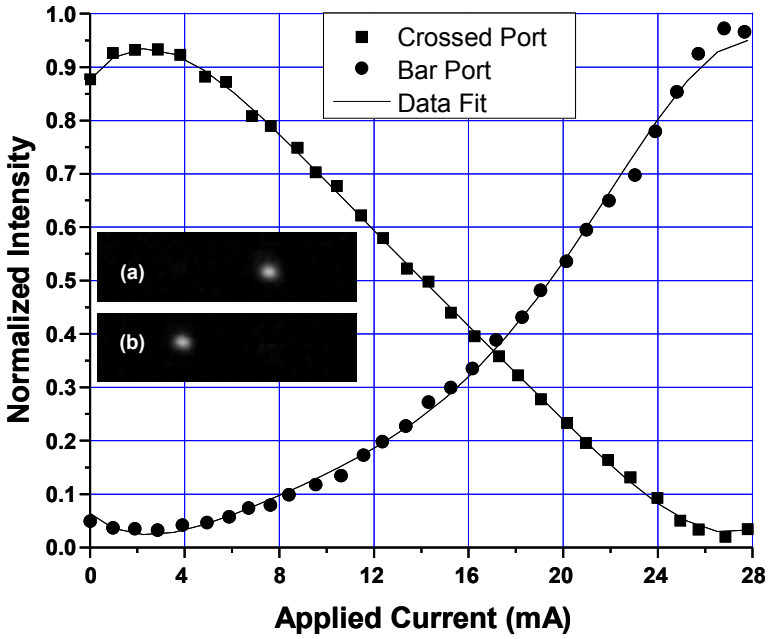

Figure 3.22 Measured tuning response of quantum dot based 2 x 2 switching device at λ = 1310 nm for TE polarization. The inset shows the near field image of the device output facet with (a) the optimum switching to the crossed-port and (b) the optimum switching to the bar-port.

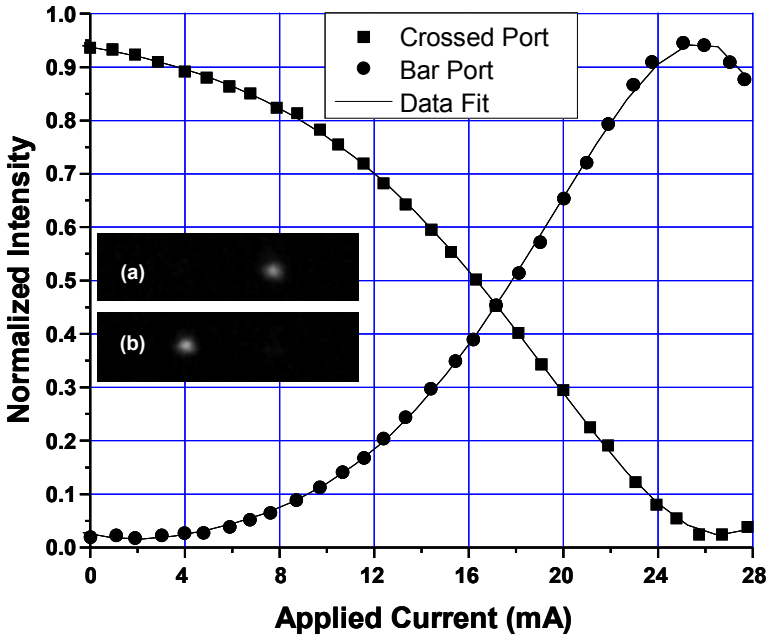

Figure 3.23 Measured tuning response of quantum dot based 2 x 2 switching device at $\lambda = 1310$ nm for TM polarization. The inset shows the near field image of the device output facet with (a) the optimum switching to the crossed-port and (b) the optimum switching to the bar-port.

Additional testing showed that the device response and recovery time constants were both on the order of 1 μs. An exponential fit was applied to the leading and trailing edges of the device response to the pulsed electrical current (square pulses) under CW laser conditions. The device response and recovery times were determined to be approximately 1.1 μs and 1.7 μs respectively, closely matching those values measured for the VPS in section 3.4.1. The short recovery time, only slightly longer than the response time is indicative of the fast heat dissipation properties of the GaAs/AlGaAs material system. These results are comparable, and in some cases better than, the response times seen for thermo-optic switches based on silicon-on-insulator (SOI) materials [87, 96, 97], and orders of magnitude better than for polymer and polymer-silica hybrid devices, which operate on the scale of milliseconds and hundreds of microseconds

respectively. Beam prop simulations of the device suggested a $\Delta n \approx 0.019$ was need for full switching. Assuming this to be correct and using an approximate value of the thermo-optic coefficient for GaAs-based materials ($dn/dT \approx 2.5 \times 10^{-4}/°K$), as well as the relation for temperature induced index change ($\Delta n = \Delta T\ (dn/dT)$), then the calculated change in temperature would be roughly 80 °K.

The device was also probed near the bandedge of the QD's, using the Mavericks Cr:Forsterite laser operating at 1265 nm. Since this laser was not fiber coupled, the testing setup was slightly modified to accommodate the new laser, with a half-wave plate used to alter the polarization of the injected laser light (Fig. 3.13). The results for device testing at 1265 nm are shown in Fig. 3.24 and Fig. 3.25, for TE and TM polarization respectively. The power splitting ratio for the device under these conditions were from 1:34 to 11:1 over a range from 0 mA to 25 mA for TE polarized light, and from 1:116 to 8:1 with a current range of 0 mA to 24 mA for TM polarized light. This corresponds to a channel-to-channel crosstalk of -10.5 dB (TE) and -9.1 dB (TM). A 50:50 split ratio was reached at a value of 15.7 mA for both polarizations. Operation at wavelengths near the bandedge yielded a significant increase in the measured insertion loss for TE polarize light as compared to TM polarized light. The insertion losses of the device, when measured at 1265 nm with surface reflections taken into account, was found to be 33.9 dB (TE) and 17.5 dB (TM).

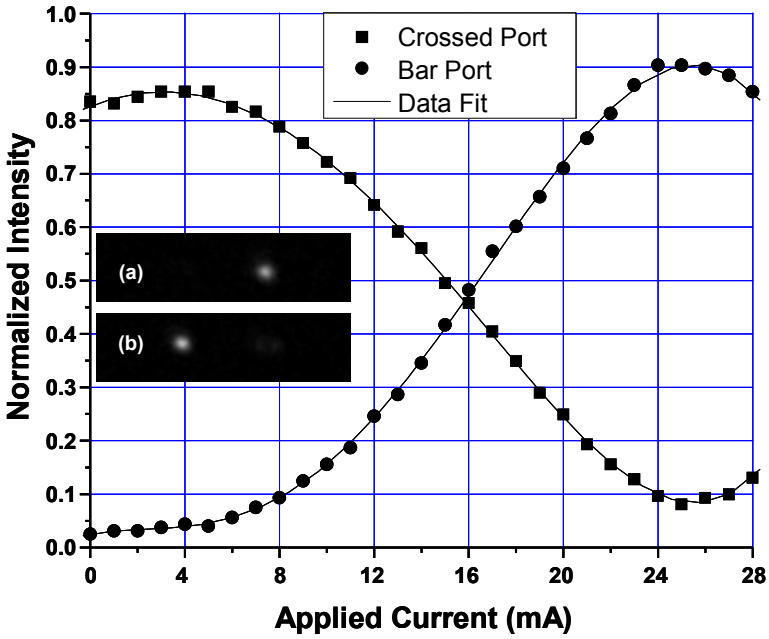

Figure 3.24 Measured tuning response of quantum dot based 2 x 2 switching device at λ = 1265 nm for TE polarization. The inset shows the near field image of the device output facet with (a) the optimum switching to the crossed-port and (b) the optimum switching to the bar-port.

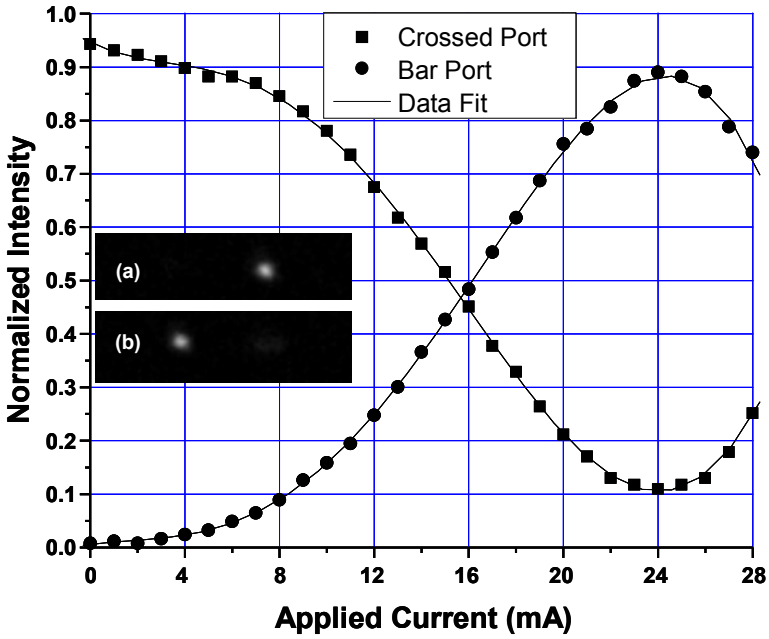

Figure 3.25 Measured tuning response of quantum dot based 2 x 2 switching device at λ = 1265 nm for TM polarization. The inset shows the near field image of the device output facet with (a) the optimum switching to the crossed-port and (b) the optimum switching to the bar-port.

Though the switching range does not match that seen at 1310 nm, the tuning is still broad enough at over 40 nm from the optimum wavelength to be useful for a number of applications, such as a tunable power splitter. The device could also be used as a modulator or variable optical attenuator given the low crosstalk in the off-state (-15.3 dB – TE and -20.6 dB – TM) and utilizing only the bar port in the on-state. The bar-port extinction for TE and TM is -15.6 dB and -20.4 dB respectively. Additionally, the device length can be adjusted for improved operation at this wavelength. At greater issue is the losses measured at the tested wavelength (1265 nm) for this device. While some of the losses can attributed to a non-optimum device length for the tested wavelength, the large difference between values reported for the two polarizations cannot. This discrepancy in optical losses near the absorption bandedge is not unexpected, however, as it

has been previously reported in the literature [62, 98]. This is principally due to the anisotropy between the lateral and vertical dimensions of most quantum dots grown with the Stranski-Krastanow growth mode, as well as the induced compressive strain inherent to the process. QD's formed in this fashion typically take the form of a flattened pyramid with relative dimensions between the height and width being 1:4, resulting in a stronger electronic confinement in the growth direction. As a result, the QD's have a heavy hole valence-band ground state which does not couple to light polarized perpendicular to the growth surface, leading to a reduction in the TM polarized absorption [62]. However, for QD based switches, this disparity provides an opportunity to explore the nonlinear characteristics of the material for application to all-optical switching.

CHAPTER 4: ALL-OPTICAL MUTLIMODE INTEREFENCE SWITCHING DEVICES

The rapid saturation of the carrier induced change in the refractive index in self-assembled quantum dots (SAQD's) has been shown to severely limit its application in active multimode interference (MMI) switching devices which have very short interaction lengths. The few reports of MMI devices that have incorporated SAQD materials utilized a basic MMI Mach-Zehnder configuration where the active components were the nonlinear phase shifting arms situated in-between the passive MMI-couplers [17, 18], permitting a larger degree of phase accumulation. Optical control was employed in both cases, with one inducing self-phase modulation in an optical combiner [17] and with the other using a vertical, off-plane, excitation of the Mach-Zehnder phase shifting arm [18]. Creating a compact all-optical active MMI switch, however, requires incorporating the phase shifting component into the MMI waveguide itself, and consequently there is a need for a wider range of control over the refractive index change than is possible with QD materials through carrier induced nonlinearities. MQW's, on the other hand, permit a much larger change in the refractive index for a given current density [22], and functional, current controlled, 2 x 2 MMI devices which take advantage of the carrier induced change in the refractive index in MQW's have previously been realized [80]. MQW's are therefore a more suitable material for the construction of all-optical, MMI switches.

In this chapter, active MMI-based switching devices were studied in relation to their response to the optical generation of carriers through in-plane excitation. The devices are a variation on the tunable 2 x 2 MMI cross coupler discussed in section 3.6, configured to operate with an optical pump beam launched into the same access port as the signal beam. Selective area

disordering of the bandgap was used to minimize carrier generation outside the designated modulation regions. A single modification to the MMI structure allows for control over the distribution of optically induced carriers. Prior to examining the all-optical switches, a simple Fabry-Perot etalon, fabricated using the $In_{0.15}Ga_{0.85}As/GaAs$ SAQD wafer material, is discussed as an extension of the work in section 3.4. Then a 2 x 2 MMI device was built from the same SAQD material to act as a comparison to the MQW based devices, as an attempt to measure the extent of the all-optical response. Finally, in order to demonstrate the efficacy of the all-optical MMI switch design, devices were fabricated using InGaAsP/InGaAsP MQW material, and were tested at wavelengths in and around 1550 nm.

4.1 Optical Pumping: SAQD Ridge Waveguide

As part of investigating the SAQD material response to optically generated carriers, a ridge waveguide was fabricated using the same method as was presented in Section 2.1.3.1. The waveguide was 935 μm long and had a ridge height of 1.45 μm. Metal contacts along the length of the device allowed for the application of current as well as a means for monitoring the photocurrent on a Keithley source meter. The Fabry-Perot response was measured and the waveguide was used to demonstrate simple wavelength conversion. The response to an applied reverse bias was also studied.

4.1.1 Experimental Setup

The experimental setup is depicted in Fig. 4.1. Light from a fiber pigtailed DFB laser diode operating at a nominal wavelength of 1.31 μm (signal beam), and in CW mode, was sent through a fiber-based polarization controller which enabled selection of either TE or TM polarized light (TE parallel to the active layer and TM perpendicular). The optical beam then passed into a 2 x 1 power combiner so that it could be copropagated with femtosecond light pulses (pump beam) from the mode-locked Mavericks Cr:Forsterite laser. From the power combiner the two beams passed into a SMF-28 lensed fiber which end-fire coupled the light into the device input port. Transmission from the device output facet was collected with a matching lensed fiber and sent to a semiconductor optical amplifier (SOA) to enhance the detection of the modulated signal beam. The light then passes through a narrow band fiber Bragg grating filter to remove any remaining pump beam light as well as the SOA noise due to amplified spontaneous emission before being captured by a 50 GHz InGaAs photodetector (Discover Semiconductors, Inc Lab Buddy). Electrical bias could be supplied by a Keithley 2400 source meter if contacts were present on the device being tested. Data was gathered from a HP 83480A digital communications analyzer. When mode-locked, the Maverick Cr:Forsterite pump laser had a pulse repetition of 75.4 MHz and a peak power at around 1240 nm (slightly shorter than the SAQD photoluminescence peak at 1267 nm). Upon leaving the cavity, the pump beam was coupled into a single-mode fiber with a 40x microscope objective and then passed through a fiber-based polarization controller, thereby allowing a selection of TE or TM polarization. The pump then entered the 2 x 1 power combiner where it was coupled into the same lensed fiber as the signal beam before being launched into the device input port.

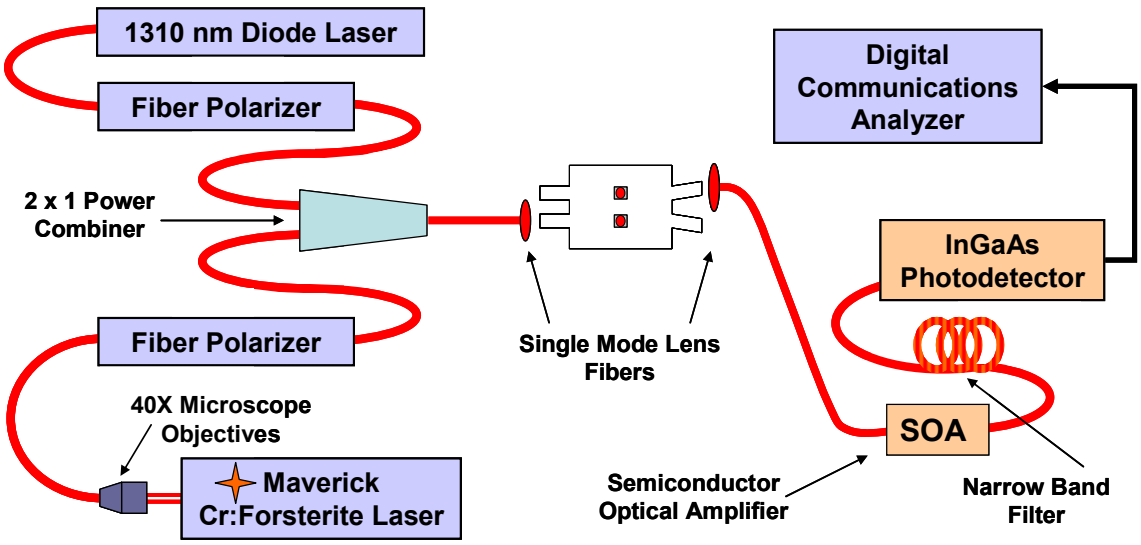

Figure 4.1 Experimental setup for optical pulse testing of SAQD waveguide devices.

4.1.2 Results and Discussion

As part of the device characterization, the photocurrent response was investigated for both signal and pump beams. Unsurprisingly, given the large differences in insertion losses noted in section 3.6 between the TE and TM polarizations at 1265 nm, the photocurrent measurement was highest for TE polarized light and lowest for TM polarized light. This was true irrespective of wavelength. For the pump beam (1240 nm), the ratio of the photocurrent produced by TE and TM polarized light was roughly 6:1. For the signal beam (1310 nm) the ratio was approximately 4:1. The quantity of free carriers produced by the TE polarized pump beam would then be estimated to be roughly an order of magnitude larger than for the TM polarized pump beam, given equivalent input power. This difference should also be reflected in the magnitude of the

signal beam response to carrier induced changes in the refractive index. As an aside, the connection between polarization and photocurrent was also useful in that the device itself could act as a polarization monitor, eliminating the need to remove the output lensed fiber in order to verify the polarization with a free space polarization analyzer.

The DFB laser diode was used as the source for the CW signal beam, and could be tuned from approximately 1308.5 nm to 1309.5 nm by adjusting the laser driver current over a range from 20 mA to 70 mA. This was used to scan the ridge waveguide for a Fabry-Perot response. The results of the scan for TE polarized light are shown in Fig. 4.2 with both the output power and photocurrent response plotted. Since the ridge waveguide is in effect a Fabry-Perot etalon, strong transmission resonance is not surprising. Using the device length and the given wavelength range, it was relatively simple to fit the equation for Fabry-Perot transmission to the data, excluding absorption, (Fig. 4.3) and to extrapolate an effective index for the guiding region ($n_{eff} = 3.339$) of the ridge waveguide. This value is in good agreement with the effective index calculated for TE polarized light using the BeamProp software ($n_{eff} = 3.338$). Interestingly, the photocurrent response very closely matches that of the transmission, with peak and troughs occurring at approximately the same wavelengths.

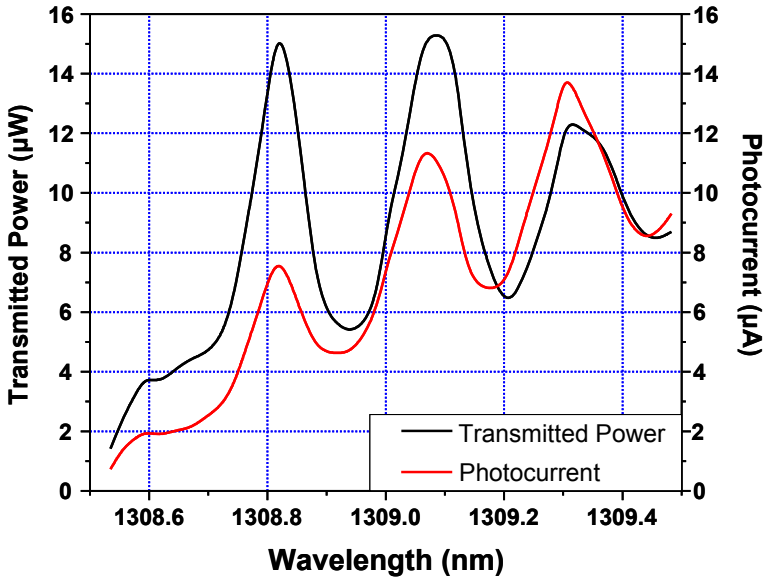

Figure 4.2 Ridge waveguide Fabry-Perot and photocurrent responses.

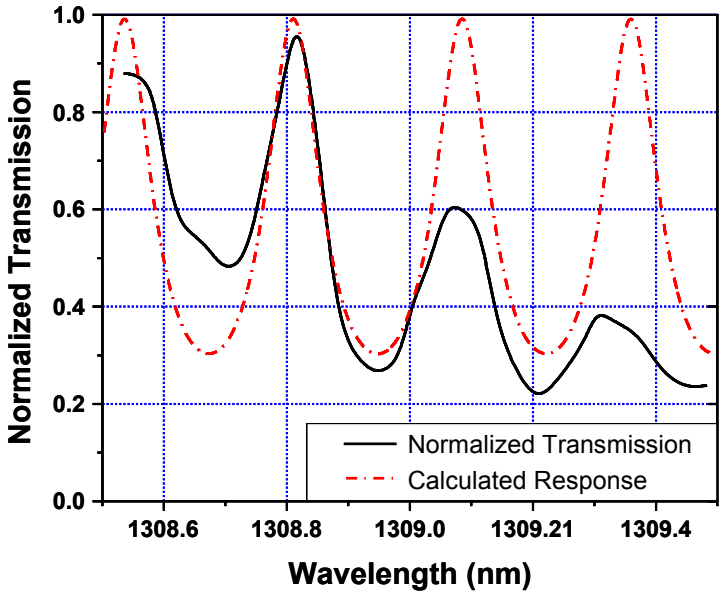

Figure 4.3 Ridge waveguide Fabry-Perot model vs. measured transmission.

Both the CW signal and pulsed pump beams were launched into the waveguide using a single-mode lensed fiber, as described in the experimental setup in section 4.1.1. Nonlinearities induced by the femtosecond pulses of the Cr:Forsterite laser is expected to lead to a modification of the waveguide refractive index. These perturbations cause intensity changes in the signal beam that are captured by the InGaAs photodetector. The pulse repetition time of the pump beam *(~13.2 ns*) is sufficiently long so as to allow time for the carriers to relax before the next pulse arrives.

When the signal and pump beams were coupled into the ridge waveguide, with both beams TE polarized, a series of pulses were detected on the oscilloscope which exhibited the same repetition frequency as the pump source. The existence of these pulses was confirmed to be tied to the presence of the signal beam and an Agilent 86146B optical spectrum analyzer was utilized to show that the pump beam was being completely blocked by the narrow band fiber Bragg grating filter. The polarity of the pulse response (up or down) was dependent on the precise wavelength of the signal beam. When wavelengths that corresponded to the peaks of the Fabry-Perot response (Fig. 4.3) were chosen, down-pulses were measured, while wavelengths corresponding to the troughs produced up-pulses. The modification of the waveguide refractive index by the pump beam excitation, led to changes in the phase difference between the internal reflections from the waveguide facets, thereby shifting the Fabry-Perot response of the waveguide. With the transmission at an extremum for these wavelengths any index change would create a corresponding reduction (at resonance peaks) or increase (at transmission troughs) in the throughput intensity. Most subsequent measurements were done at these broad extremum points, where the pulse profile was relatively stable. Away from these points the pulse

profile was more susceptible to variation over time due to minute changes in device temperature or slight shifts in the signal beam wavelength.

The outcome of changing the input polarization for the signal beam is shown in Fig. 4.4. The same pump power was used in each case (1.665 mW measured after the 2 x 1 combiner and before the SMF-28 lensed fiber). The wavelength of the signal beam was set at 1309.083 nm (Fabry-Perot resonance peak), and gives the expected down-pulse when both pump and signal beams were TE polarized. A maximum transmission change of 13% from the pre-pulse level was measured. Using an exponential decay fit, the recovery time constant of the pulse was determined to be 727 ps, which is on the order of the recovery time due to carrier recombination as reported in pump-probe experiments involving QD SOAs [99]. However, full signal recovery does not occur for several nanoseconds, extending beyond the range of the plot. This is likely due to the large number of photogenerated carriers and the screening of the built-in electric field by carriers that have escaped from the QDs [100]. Keeping the pump beam TE polarized and changing the signal beam to be TM polarized (Fig. 4.4), results in a much weaker response. The profile is very similar to that which occurs when both pump and signal beams are TE polarized. When normalized to the same magnitude the pulses roughly overlap. The exponential decay fit to the pulse recovery yielded a time constant of 569 ps, though again full recovery of the pulse extended several nanoseconds. The significant decrease in TM polarized signal pulse bears strong similarity to the measurements taken of the index change for TE and TM polarized light due to electrical carrier injection in section 2.1.3.3. In that case, there appeared to be distinct reduction in the carrier induced change in refractive index experienced by the TM polarized signal beam for a given current density. This nonlinear TE/TM signal change is most likely

caused by the high degree of dichroic absorption in the quantum dots due to the asymmetric geometry of the nanostructures. Basically the TM polarized signal does not sense the change in the heavy-hole exciton caused by the presence of the free carriers. Since the light hole exciton is further detuned from the signal beam photon energy, the nonlinear effect is much reduced. These results confirm that the free carrier plasma effect contributes significantly less to the overall nonlinear refractive index changes.

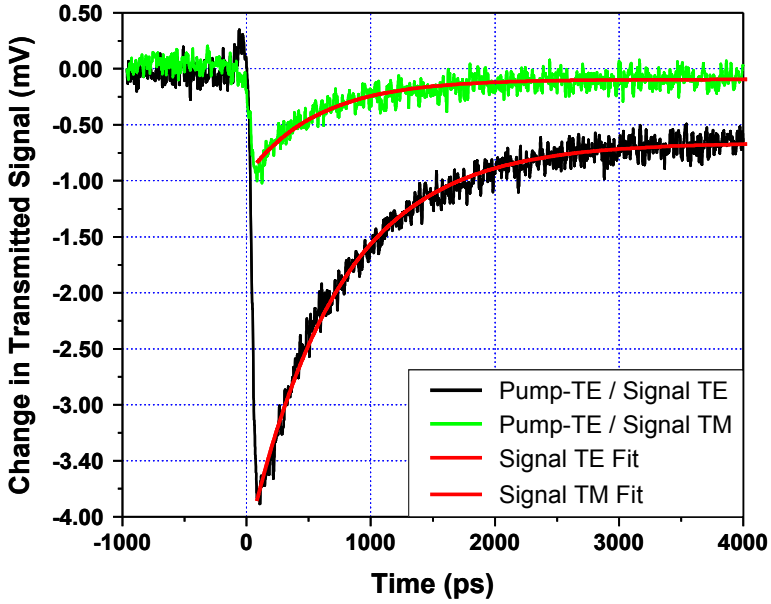

Figure 4.4 Ridge waveguide response to changes in the signal beam polarization with the pump beam TE polarized.

A reverse bias field was applied across the waveguide contacts, perpendicular to the growth layer, to attempt a carrier sweep-out and to determine the effect on the pulse profile. The application of the reverse bias acted to tune the Fabry-Perot etalon and shift the pulse polarity. The evolution of the switching response to the increasing reverse bias potential with the pump and signal beams both TE polarized is shown in Fig. 4.5. By increasing the voltage value from 0

V to 6 V in 500 mV intervals, the pulse traverses one complete cycle of the Fabry-Perot etalon. Calculating from the model used in Fig. 4.3 suggests that an increase in the refractive index of $\Delta n \approx 7\times10^{-4}$ was required to complete that cycle. Time constants for 0 V, 1 V, 2 V, and 6 V were found using an exponential fit to the pulse recovery and are 727 ps, 497 ps, 485 ps, and 346 ps respectively, showing a decrease in the initial recovery time. However, in each case, full recovery still extended out over several nanoseconds. The corresponding change in the pre-pulse transmission level with increasing reverse bias is shown in Fig. 4.6. A representation of how the phase of the Fabry-Perot position is affected by the combination of reverse bias and optically generated carriers is shown in Fig. 4.7. For the TE pump and TM signal combination the general response was similar, though the amplitude range was significantly smaller for the same pump and signal beam average powers.

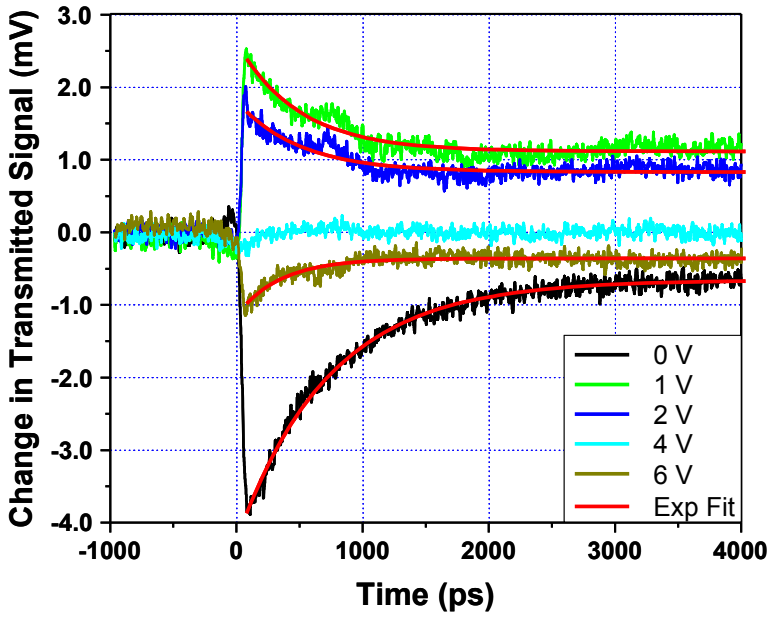

Figure 4.5 Evolution of the ridge waveguide switching response to increasing reverse bias, with both pump and signal beams TE polarized.

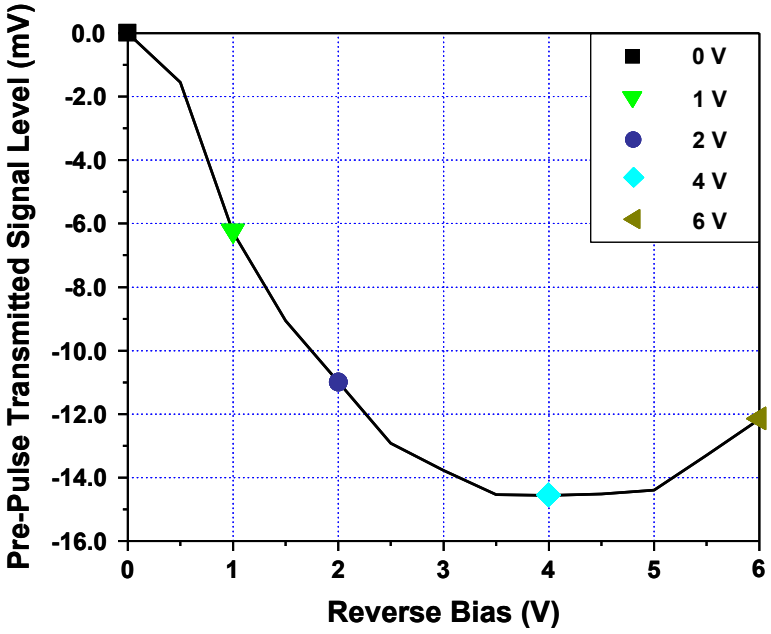

Figure 4.6 Change in the ridge waveguide pre-pulse transmission due to the applied reverse bias.

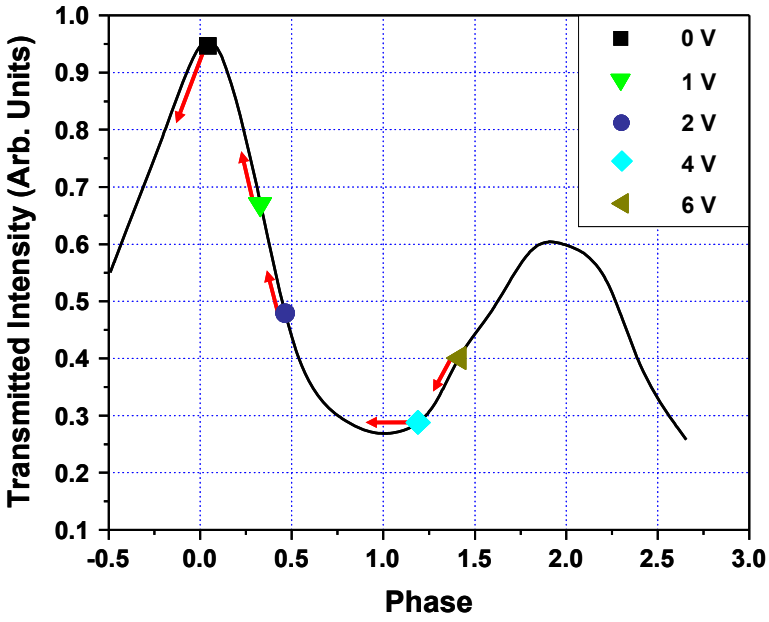

Figure 4.7 Representation of the change in the relative position of the DC-level and the switching response with respect to the Fabry-Perot curve. The red arrows depicts shift due to optically generated carriers, though are not indicative of precise values.

4.2 General Design and Operation of All-Optical MMI Switching Devices

Modifying the 2 x 2 MMI cross-coupler switch from section 3.6 into a device using all-optical control required changes to be made to the device architecture. The general layout and the relative dimensions of the device remained the same. Restricted paired interference was used and light could be launched through either of the two input waveguides, which were centered at $\pm W/6$ with respect to the central axis of the MMI waveguide. Both the input and output waveguides were 3 µm wide and 500 µm long. The output waveguides were angled so that the edge-to-edge separation increased from an initial 3 µm at the MMI to 6 µm at the end facets. In order to produce a device that could be more readily integrated into a planar chip structure, the switch

was limited to operating using in-plane excitation, as opposed to using a format which depended on excitation from an off-plane source.

In order to realize all-optical switching with the MMI-based device, there were two main issues to be dealt with. First, index modulation regions needed to be defined and a method for selectively distributing the optically generated carriers between them needed to be realized. In this case it was convenient to utilize the same modulation regions that were employed in the 2 x 2 MMI cross-coupler devices, thereby limiting the number of areas where carrier control was necessary. As noted there, these modulation regions were located at the first occurrence of the two-fold image set, with each modulation region centered on one of the two images. Regulating the distribution of the optically generated carriers between the modulation regions allowed for optimum control of the relative phase difference between the images of the two-fold set. The second concern was the need to limit absorption loss and unwanted carrier generation in the input waveguides and other regions within the MMI outside the index modulation regions. Large amounts of extraneous carrier generation have the potential to inhibit effective phase control at the designated index modulation regions and to degrade the device performance. Each of these issues will be addressed in turn.

4.2.1 Control Over the Distribution of Optically Generated Carriers

When a light beam is launched into one of the MMI waveguide's access ports, regions of high carrier density naturally form at the locations corresponding to the various self images of the input field. The concentration of carriers generated can be maximized by orienting the light

to the TE polarization and by choosing a wavelength which falls within the absorption bandedge of the material. However, each image set that forms will have the input beam power distributed equally between all of the images belonging to that particular image set. Therefore, the concentration of optically generated carriers will be approximately the same at each of those locations that correspond to the images within that set. Though for devices with an off-center launching point this is not completely true, any variation in the power distribution is expected to be minute and to decrease rapidly with propagation distance. In an attempt to produce a more efficient device, a deliberate imbalance was created in the distribution of these optically generated carriers between two specific areas along the midpoint line of the MMI waveguide. Each of these areas overlaps the position of one of the two images in the first two-fold image set ($p = 1, N = 2$). By manipulating the carrier distribution, the refractive index at these two locations can be modified by different amounts, which leads to an alteration of the phase relation between the corresponding images. The change in this phase relation also affects the formation of all subsequent images in the direction of propagation, allowing for a signal to be switched between the two output ports. A general schematic showing the device layout is given in Fig. 4.8.

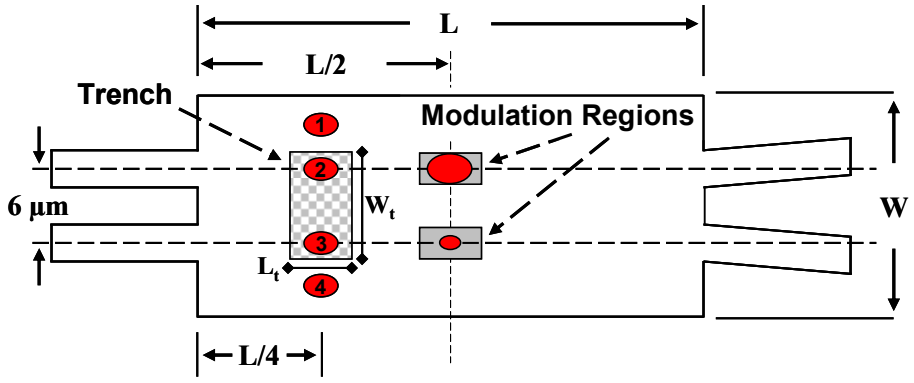

Figure 4.8 Schematic for multimode interference all-optical switching device.

To create an imbalance in the carrier distribution at the two-fold image set, a trench was etched at *L/4*, and centered such that it overlapped the positions of the 2nd and 3rd images in the first four-fold set (*P = 1, N = 4*) as shown in Fig. 4.8. The trench width was 10 μm (W_t) and the length was 54 μm (L_t). By controlling the precise depth of the trench, any fixed power ratio between the two-fold images can be obtained. For the SAQD wafer structure, simulations (BeamProp 5.0) of the light distribution in a 2 x 2 MMI cross-coupler are presented in Fig. 4.9 (a) without trenches, in Fig. 4.9 (b) with trenches etched down to within 315 nm of the intrinsic region, and in Fig. 4.9 (c) with trenches etched to within 265 nm of the intrinsic layer. The dimensions of the MMI waveguide were 1175 μm long and 18 μm wide. As can be seen, the power balance at L/2 is significantly altered when these trenches are incorporated into the structure of the MMI waveguide. If the pump beam, which is used to create the carriers, is pulsed, it will cause periodic changes to the refractive index difference between the two index modulation areas. A CW signal beam, sent through either input port, will then "see" the index changes and respond by shifting from the crossed output port (off-state) to the bar output port (on-state). As the carriers generated by the pump pulse decay, the signal beam will begin to switch back to the crossed output port, with full recovery dependent on the carrier lifetime, which is expected to be on the order of nanoseconds.

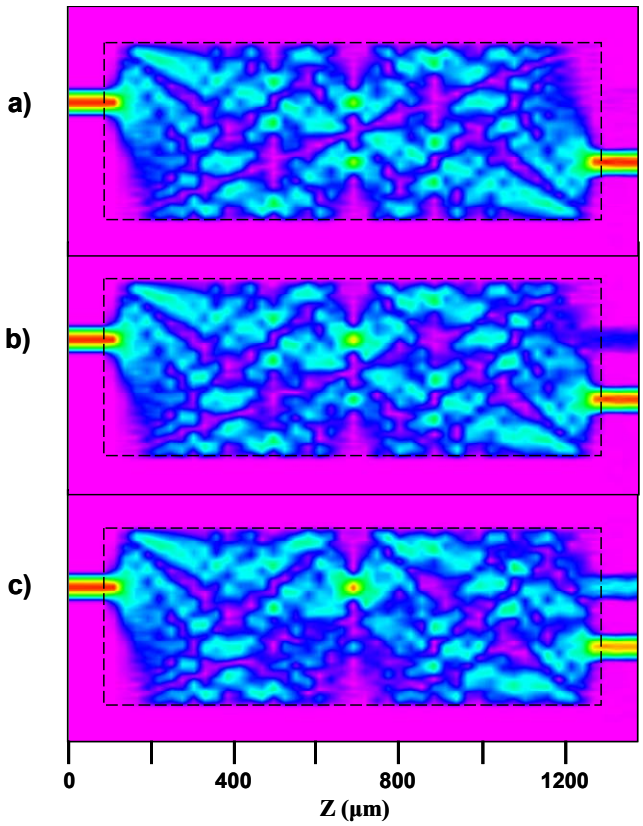

Figure 4.9 Simulations for MMI-based tunable cross-coupler switch (a) without trenches, (b) trench depth within 315 nm of intrinsic region, and (c) trench depth within 265 nm of intrinsic region. $In_{0.15}Ga_{0.85}As/GaAs$ SAQD wafer structure was used.

The design for the MQW-based version of the all-optical MMI switching device is in essence identical. Adjustments were made to the device length in order to compensate for differences in the refractive indices of the epitaxial layers. The depth of the index modification trench was also altered due the differences in the wafer material (Fig. 2.11). The device layout consists of an MMI waveguide with a width of W = 18 µm and a length of L = 955 µm. All of the other dimensions were the same. BeamProp scans were also run for the InGaAsP/InGaAsP MQW wafer structure. A simulation of the light distribution without trenches is shown in Fig. 4.10 (a), and with trenches etched down to 255 nm above the InGaAsP region in Fig. 4.10 (b).

For the MQW wafer structure used in this study, the presence of the trench significantly distorts the power distribution at the output facet, with more of the light directed to the bar output port, however the majority is still coupled to the cross port. In this case, as with the SAQD device, when the signal beam sees the index changes induced by the pump beam, it responds by shifting from the cross output port (off-state) to the bar output port (on-state). As the carriers generated by the pump pulse decay, the signal beam will begin to switch back to the coss output port, with full recovery again dependent on the carrier lifetime.

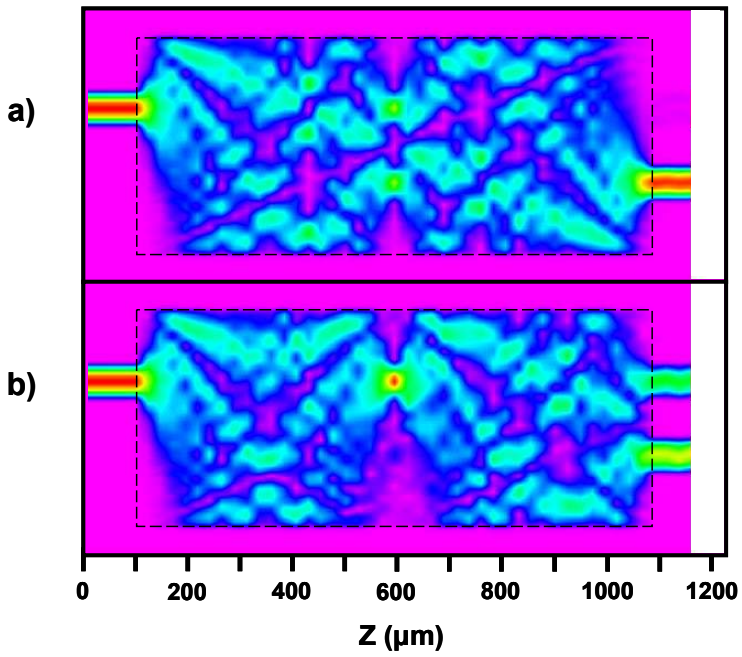

Figure 4.10 Simulation of light distribution in the multiple quantum well, all-optical switching device for (a) no trench (b) trench floor at 245 nm above the InGaAsP region.

4.2.2 Selective-Area Bandgap Tuning

If the device is fabricated from either wafer in the as grown condition, light from the pump beam will also be absorbed within the input waveguide and in parts of the MMI outside the designated index modulation regions (Fig. 4.8). This will lead to carrier generation, and in turn, index modification, in sections of the device where it could degrade the overall performance. Furthermore, as a result of this unwanted carrier generation, device power requirements would need to be increased in order to compensate for the associated losses. To avoid these difficulties, selective intermixing of the devices was undertaken to shift the bandgap of the materials to higher energies, increasing the transparency for both the pump and signal beams in the areas outside the index modulation regions. For the SAQD material, this can be accomplished by capping the majority of the wafer sample with SiO_2 grown by PECVD, while leaving only the index modulation regions uncapped (Fig. 4.11). The uncapped regions are then treated with the CF_4-plasma process (Table 2.1) which was demonstrated in section 2.1.2 to significantly inhibit thermal intermixing in the exposed regions of $In_{0.15}Ga_{0.85}As$/GaAs SAQD's when done prior to high temperature annealing.

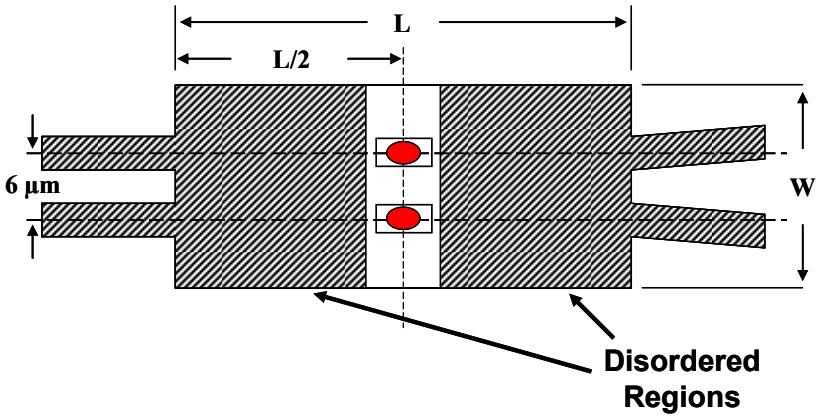

Figure 4.11 Schematic showing intermix regions of the 2 x 2 MMI all-optical switch.

For the InGaAsP/InGaAsP MQW sample, section 2.2.1 demonstrates that selective bandgap tuning can be accomplished by capping the majority of the wafer sample with PECVD grown SiO_2, and again leaving only the index modulation regions uncapped. In this case, exposure to RF generated plasma is avoided as it will enhance the thermal intermixing process prior to the high temperature annealing. Dielectric etching for this step is done using wet chemical etching. The regions of the device that were disordered by IFVD are shown in Fig. 4.11 with diagonal lines.

4.3 Device Fabrication

The methods for fabricating the MMI waveguiding structures were significantly different for the two wafer structures. The following two sections (4.3.1 and 4.3.2) give the processing steps used for the $In_{0.15}Ga_{0.85}As$/GaAs SAQD wafer and the InGaAsP/InGaAsP MQW wafer respectively.

4.3.1 Fabrication of Self-Assembled Quantum Dot MMI Waveguides

Prior to device fabrication, the SAQD wafer sample was cleaned in acetone using an ultrasonic bath to remove debris and organic residue from the surface. Native oxide was then removed by soaking the wafer sample in a buffered oxide etch solution (BOE) for 7 minutes and thoroughly rinsing the sample in DI water. The wafer was dried with nitrogen gas and baked at 120°C for 2 minutes to remove any residual volatiles.

Fabrication began with the growth of 200 nm of PECVD SiO_2 on the SAQD wafer sample. Contact photolithography with Futurrex NR7-1000PY negative photo-resist (Table 4.1) was used to define the location of a 100 μm long thermal intermixing trench center at *L/2* and which was then etched into the SiO_2 using the CF_4-plasma process in Table 2.1. The photo-resist was removed and the sample was placed inside the RTA furnace where it was arranged with the epitaxial side facing down in-between two pieces of freshly cleaned GaAs mechanical wafer. The chamber was purged with N_2 gas for 30 minutes to remove any oxygen that might interact with the semiconductor surface and the sample was annealed at 725 °C / 20 seconds. The expected shifts in the peak photoluminescence for the section of the device capped with SiO_2 and for the uncapped section exposed to the CF_4-plasma can be seen in Fig. 2.5 (a).

Table 4.1 Photolithographic process steps for trench formation.

Photolithographic Process Steps for Trench Formation	
Spin Photo-Resist (Futurrex NR7-1000PY)	5000 rpm / 50 sec.
Pre-Bake	150°C / 1 min.
UV Exposure	12 mW/cm^2 / 24 sec.
Hard Bake	100°C / 2 min
Developer (Futurrex RD-6)	14 sec.
Oxygen Plasma	120 sec.

After the annealing step, the SiO_2 layer was etched in a RIE chamber with the CF_4-plasma process in Table 2.1 for 7 minutes. In addition to removing the SiO_2, the process ablated about 35 nm of the contact layer in the uncapped areas of the sample, transferring the alignment marks, and the intermixing window, into the surface. A new 200 nm layer of PECVD SiO_2 was then grown, and the pattern for the index modulation trenches was formed using contact photolithography and Futurrex NR7-1000PY negative photo-resist. The CF_4-plasma etching process was again used to transfer the pattern into the SiO_2 layer. The photo-resist was removed and the trench pattern was etched deep into the AlGaAs upper cladding layer using a solution of H_3PO_4:H_2O_2:H_2O (1:2:50). Some devices on the wafer sample were protected with negative photo-resist to act as controls. The current SiO_2 masking layer was removed with BOE, and the sample was then coated with 100 nm of Si_3N_4 which provided better adhesion for the BCB planarization layer than bare GaAs. The BCB polymer was used to fill in the trenches and provide a continuous surface for further processing.

Formation of the MMI and access waveguides followed the process described in section 2.1.5. A combination of 50 nm of PECVD Si_3N_4 and 350 nm of SiO_2 were deposited on the sample. The waveguides were patterned for metal lift-off with negative photo-resist and contact photolithography (Table 3.5). Then a sequence of 40 nm of Cr, 88 nm Ni, and 70 nm Cr was thermally evaporated onto the sample and the extraneous metal was lifted off in resist remover. The dielectric layer was then etched with a highly anisotropic CF_4-plasma process designed to produce nearly vertical sidewalls (Appendix: Table 6.1), and the waveguide was etched using the sputtering process outlined in Table 2.3 to a depth of about 1900 nm. Next, the sample is placed in etching solution of H_3PO_4:H_2O_2:H_2O in a volume ratio of 1:2:50 for 4 minutes to narrow the waveguides by approximately 1.6 μm to compensate for the angled sidewalls produced by the sputter etching. The remaining metal and dielectric are then removed by soaking the sample in BOE. At this point, the substrate side of the sample was lapped down to a thickness of 120 μm and polished to a mirror finish. Finally, the device was cleaved and mounted on a copper header for testing. A complete device is pictured in Fig. 4.12.

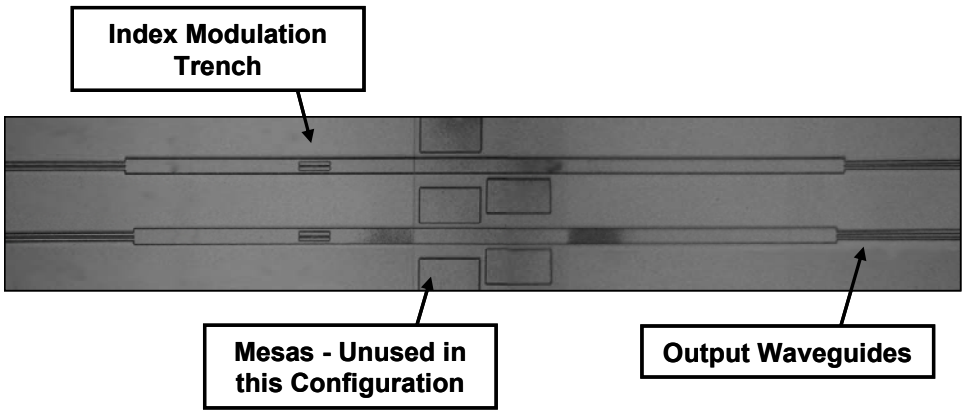

Figure 4.12 Photograph of a finished SAQD all-optical switch.

4.3.2 Fabrication of Multiple Quantum Well All-Optical MMI Device

The MQW wafer sample was prepared by cleaning in acetone using an ultrasonic bath to remove debris and organic residue from the surface. Native oxide was then removed by soaking the wafer sample in a buffered oxide etch solution (BOE) for 7 minutes and thoroughly rinsing the sample in DI water. The wafer was dried with nitrogen gas and baked at 120°C for 2 minutes to remove any residual volatiles. Fabrication began with the growth of 200 nm of PECVD SiO_2 on the MQW wafer sample. Contact photolithography with Futurrex NR7-1000PY negative photo-resist (Table 4.2) was used to define the location of a 100 μm long thermal intermixing trench (centered at *L/2*) which was then etched into the SiO_2 by suspending the sample in BOE for 75 seconds. The use of wet chemical etching (WCE) avoids the deleterious effect of plasma enhanced intermixing as discussed in section 2.2.1.2. The photo-resist was removed and the sample was placed inside the RTA furnace, arranged with the epitaxial layer face down, between two pieces of freshly cleaned GaAs mechanical wafer. The chamber was purged with N_2 gas for 30 minutes to remove any oxygen that might interact with the semiconductor surface and the sample was annealed at 800 °C for 20 seconds. The measured photoluminescence spectra for the section of the device capped with SiO_2 and the section which was uncapped are shown in Fig. 4.13.

Table 4.2 Photolithographic process steps for trench formation.

Photolithographic Process Steps for Trench Formation	
Spin Photo-Resist (Futurrex NR7-1000PY)	5000 rpm / 50 sec.
Pre-Bake	150°C / 1 min.
UV Exposure	12 mW/cm^2 / 26 sec.
Hard Bake	100°C / 2 min
Developer (Futurrex RD-6)	16 sec.
Oxygen Plasma	80 sec.

After annealing, the exposed portion of the $In_{0.53}Ga_{0.47}As$ layer was etched for 15 seconds in a solution of H_3PO_4:H_2O_2:H_2O in a volume ratio of 1:1:30, removing 30 nm of the contact layer and transferring the alignment marks into the surface. The existing SiO_2 mask layer was removed with BOE immersion and a new 200 nm layer of PECVD SiO_2 was grown. The pattern for the index modulation trenches was then formed using contact photolithography and Futurrex NR7-1000PY negative photo-resist. The CF_4-plasma etching process from Table 2.1 was used to transfer the pattern into the SiO_2 layer. The photo-resist was removed and the pattern etched completely through the $In_{0.53}Ga_{0.47}As$ contact layer using a solution of H_3PO_4:H_2O_2:H_2O (1:1:30). Some devices on the wafer sample were protected from further etching with negative photo-resist to act as references. The remaining devices were etched for 1 minute in a solution of HCl:H_3PO_4:$CH_3CH(OH)COOH$ (hydrochloric acid : phosphoric acid : lactic acid) in a volume ratio of 2:5:2, which removed 125 nm of InP and places the trench depth to within 245 nm of the

InGaAsP region. The current SiO_2 masking layer was removed with BOE, and a new 250 nm PECVD SiO_2 film was grown on the sample surface.

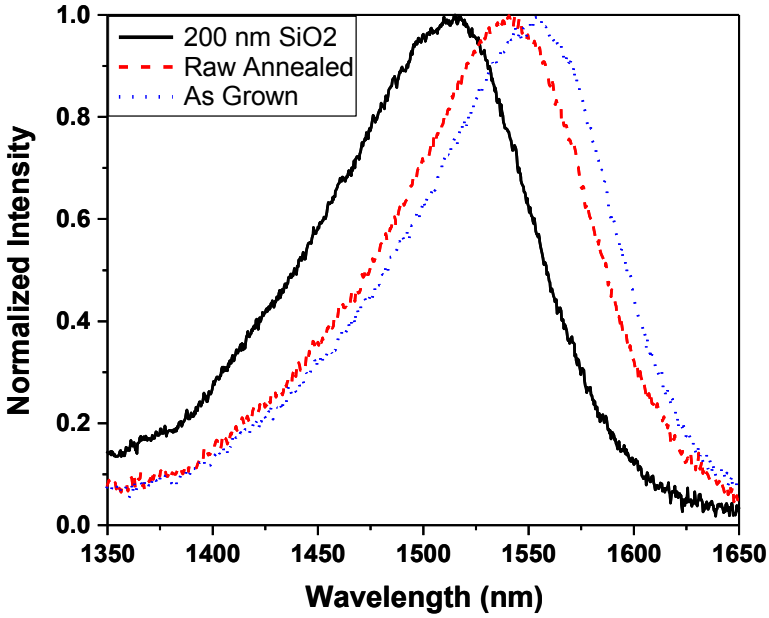

Figure 4.13 Room-temperature photoluminescence spectra for InGaAsP/InGaAsP multiple quantum wells annealed at 800°C for 20s with capped (SiO_2) and raw annealed sections.

The MMI and its access waveguides were defined using contact photolithography and Shipley S1805 positive photo-resist (Table 4.3) with the waveguides parallel to the [110] direction. The waveguide patterns were then transferred into the SiO_2 layer using the CF_4-plasma etch from Table 2.1. Any remaining photo-resist was removed by soaking in acetone. Use the SiO_2 as a mask, WCE was applied to delineate the waveguides into the wafer, with the $In_{0.53}Ga_{0.47}As$ contact layer (110 nm) etched using a solution of H_3PO_4:H_2O_2:H_2O (1:1:30), followed by etching through the InP upper cladding (370 nm) with a solution of HCl:H_3PO_4:$CH_3CH(OH)COOH$ (2:5:2). The InGaAsP region acted as an etch stop. Both solutions were selective, with the InP layer unaffected by the InGaAs etchant and vice versa. The

waveguides were then etched through the InGaAsP layer (240 nm) using a solution of H_2SO_4:H_2O_2:H_2O (1:1:10). The rates for each etching solution are given in Table 2.4.

Table 4.3 Photolithographic process steps for all-optical MQW-based MMI waveguide.

Photo-resist Patterning Steps for MMI Waveguide	
Spin HMDS (Adhesion Promoter)	5000 rpm / 50 sec
Spin Photo-Resist (Shipley S1805)	5000 rpm / 50 sec.
Pre-Bake	105°C / 5 min.
UV Exposure	12 mW/cm^2 / 8 sec.
Developer (Futurrex RD-6)	80 sec.
Oxygen Plasma	50 sec.

After the waveguides were created, the SiO_2 layer was removed by soaking in BOE. In order to prevent the large transmission losses noted in section 2.2, the $In_{0.53}Ga_{0.47}As$ layer was completely removed with an H_3PO_4:H_2O_2:H_2O (1:1:30) etching solution. The substrate was then thinned through lapping and polishing to a thickness of 150 μm. Afterwards, the sample was cleaved and mounted on a copper plug for testing. Fig. 4.14 shows a nearly complete device in which the InGaAs layer remains intact to allow definition of the thermally intermixed region surrounding the index modulation areas.

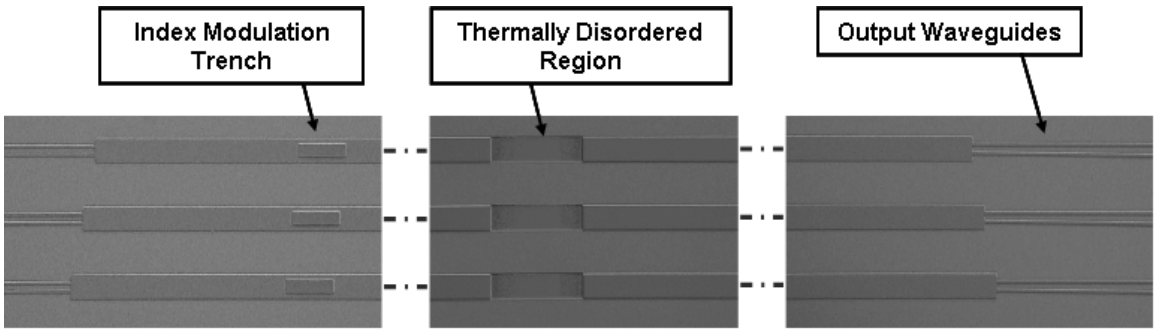

Figure 4.14 Composite photograph of a nearly finished MQW all-optical switch. At this point the $In_{0.53}Ga_{0.47}As$ layer remains intact, allowing definition of the thermally intermixed region around the index modulation areas.

4.4 Self-Assembled Quantum Dot Multimode Interference Waveguides

4.4.1 Half-Length Device with Index Modifying Trenches

In order to control the power distribution between the two index modulation regions that are positioned at the first two-fold image location, a trench was etched into the device surface such that it overlapped the 2nd and 3rd images in the first four-fold image set (Fig. 4.8). By manipulating the depth of the trench and pushing the trench floor closer to the intrinsic core region, the effective index at that location should be reduced, resulting in the light being directed from the crossed modulation area to the bar modulation area (Fig. 4.9 (b)). The efficacy of this approach was tested by fabricating a set of half-length MMI devices which, in the absence of the trench, are intended to act as 3-dB splitters. The devices were built using the $In_{0.15}Ga_{0.85}As$/GaAs SAQD material. The fabrication process was essentially the same as that presented in section 4.3.1, except that no bandgap tuning was carried out. Three sets of devices were made: one with the trench floor set at 295 nm above the intrinsic region (1420 nm from surface), another with the

trench floor set at 410 nm above the intrinsic region (1305 nm from surface), and finally a set without trenches to act as references. The devices were then placed in the test setup (Fig. 4.1) to characterize their splitting ratios when CW light was launched into one of the input ports. The wavelengths tested were 1310 nm (signal) and 1240 nm (pump) under CW conditions. A composite picture of the output facets for a 588 μm long device is shown in Fig. 4.15 for all three trench conditions at wavelengths of 1310 nm and 1240 nm. For light at 1310 nm (Fig. 4.15 (a)), the device without the trenches appears to be functioning as a near perfect 3-dB splitter, which is confirmed by the separate intensity profile measurements shown in Fig. 4.16 (a) from an optical spectrum analyzer. For a device with the trench floor etched down to 410 nm above the intrinsic layer, most of the light is transferred from the crossed port to the bar port as predicted. The intensity profiles at the output ports of this device are shown in Fig. 4.16 (b). As might be expected, when the trench floor is etched down to 295 nm above the intrinsic layer, even more of the light is transferred to the bar port, however the difference is minimal at this point. There appears to be some discrepancy between these results and Fig. 4.9 with respect to the amount of light transferred between the index modulation regions for the real and the simulated structures, but this may in part be due to the presence of output waveguides on the actual sample as opposed to the undistorted light distribution in the simulation.

Fig. 4.15 (b) shows the same set of devices but with the input wavelength at 1240 nm. It seems to indicate that the light distribution is no longer quite 50-50 at this wavelength, which is not unexpected. As the wavelength changes, so does the image location, and for a wavelength blue-shift of 70 nm, simulation suggests that the two-fold image would move approximately 30 μm in the direction of propagation, and that the crossed port image would be slightly stronger

than the bar port. With the trenches present, the light is again transferred from the crossed port to the bar port. For the device in which the trench floor is etched down to 295 nm above the intrinsic layer, the images have become distorted, almost as if the waveguides were on the verge of supporting two modes. This was the case for all devices tested at 1240 nm with trenches etched down to 295 nm above the intrinsic layer. It was not seen for trenches at shallower depths.

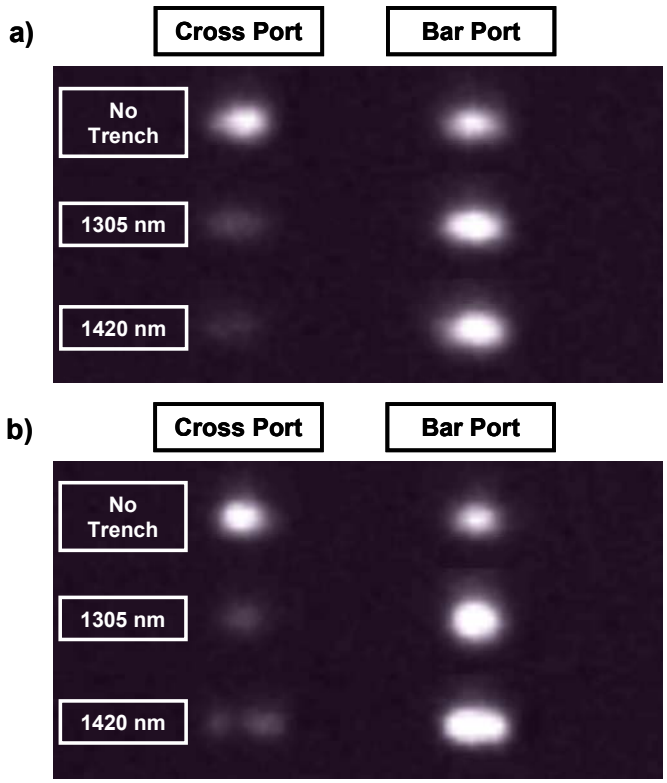

Figure 4.15 Near field image of the device output facets for devices with no trench, a trench 1305 nm deep, and a trench 1420 nm deep with the input wavelength at (a) 1310 nm and (b) 1240 nm.

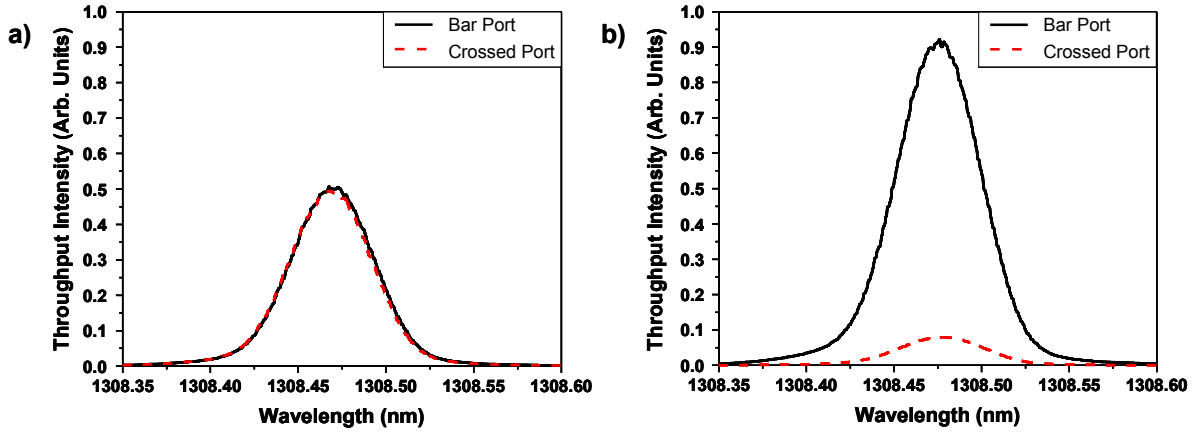

Figure 4.16 Measurement of the relative intensity profile from the output facets of devices with (a) no trench and (b) a trench 1305 nm deep. The input wavelength was 1310 nm.

4.4.2 Self-Assembled Quantum Dots 2 x 2 All-Optical MMI Device

2 x 2 MMI devices were built with the $In_{0.15}Ga_{0.85}As/GaAs$ SAQD's as described in section 4.3.1. All portions of the device outside the index modulation regions including the access waveguides were tuned to higher bandgap energies to improve transparency and reduce unwanted photo-carrier generation. Only the index modulation regions retained a bandgap close to the as grown state and would see high levels of absorption. Trenches were etched into the MMI waveguides, as was demonstrated in section 4.4.1, to control the power distribution at L/2. Testing was conducted with the experimental setup show in Fig. 4.1. When only the CW signal beam was launched into the device, the light was coupled to the crossed output port. With the addition of the pump beam launched into the same input waveguide, and with both beams TE polarized, measurements were taken at the output facets. However, no discernable switching event was detected between the output ports. Only faint changes in the transmission were

detected, and these were believed to be due to changes in the Fabry-Perot response of the device, as opposed to switching as a result to alterations to the phase relation between the two images in the index modulation region.

It was understood, given work with current controlled SAQD devices in section 3.4 which showed that the carrier induced change in the refractive index rapidly saturates, that the device interaction length was too short to produce the necessary phase shift to switch the light between the output ports. However, some detectable amount of light transfer was expected. This lack of such a response may be due to the actual interaction length potentially being shorter than anticipated. Basically, the maximum interaction distance in the MMI waveguide is set by the length of the self-images at the index modulation region and by the degree of overlap between the signal and pump beam images. For the pump beam at 1240 nm, there is a roughly center-to-center offset of 30 μm from the 1310 nm image location. Moving the pump beam to longer wavelengths reduces this, but may also reduce the strength of the nonlinear response. If the pump is set to a central wavelength of 1260 nm, then the separation between the images for the two wavelengths reduces to about 20 nm. The image length is roughly 45 μm, so there is overlap regardless of the pump wavelength, but the amount of photogenerated carriers seen by the signal beam images may be far less than then number of carrier electrically injected during the tests in section 3.4.

4.5 Multiple Quantum Well All-Optical 2 x 2 MMI Device: Single Control Pulse

4.5.1 Experimental Setup

The experimental setup for the all-optical MQW-based MMI switching device is depicted in Fig. 4.17. Light from a Santec TSL-210 tunable, semiconductor laser, with an wavelength range of 1515 nm to 1595 nm (CW signal beam), was sent through a fiber-based polarization controller which allowed selection of either TE or TM polarized light. The optical beam then passed into a 2 x 1 power combiner so that it could be copropagated with picosecond light pulses (pump beam) from an actively mode-locked erbium-doped fiber laser shown in Fig. 4.18. These two beams then passed from the power combiner into a SMF-28 lensed fiber which end-fire coupled the light into one of the device's two input waveguides. Light from the device output facet was collected with a matching lensed fiber and sent to an erbium doped fiber amplifier (EDFA) to enhance the signal pulse. The signal then passed through a DiCon tunable fiber bandpass filter ($\Delta\lambda_{bandwidth} \approx 3\ nm$) to remove any light remaining from the pump laser, as well as the EDFA noise. The signal was read by a fiber pigtailed, 8 GHz InGaAs photodetector (Ortel Corporation model #2860A receiver module). Data was gathered from a HP 83480A digital communications analyzer. The pulse repetition rate of the fiber laser (pump) was adjustable from 41 MHz to 1 GHz for an operating wavelength of 1543 nm. Upon leaving the cavity, the pump beam passed through a second EDFA to increase the pump power, and then through a DiCon tunable fiber bandpass filter ($\Delta\lambda_{bandwidth} \approx 1\ nm$) to remove the EDFA noise. The pump pulses then passed through a fiber-based polarization controller, allowing a selection of TE or TM

polarization. Finally, the pump entered the 2 x 1 power combiner where it was coupled into the same lensed fiber as the signal beam.

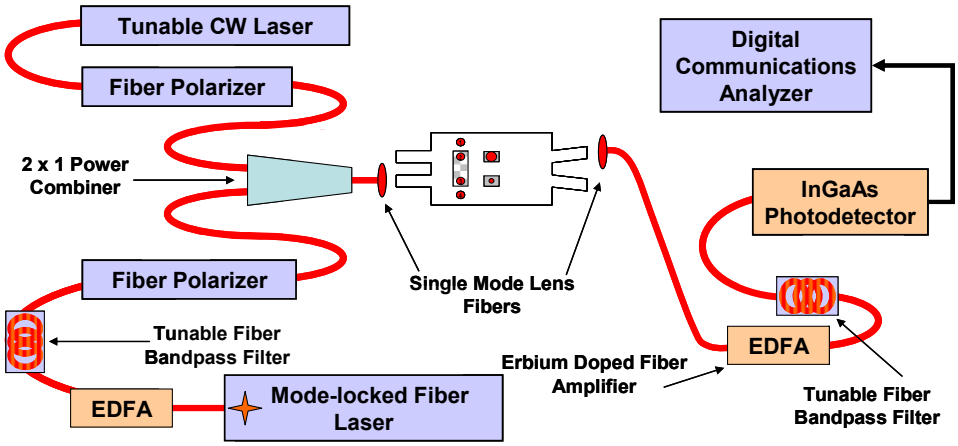

Figure 4.17 Experimental setup for single path control of the multiple quantum well-based MMI all-optical switching device.

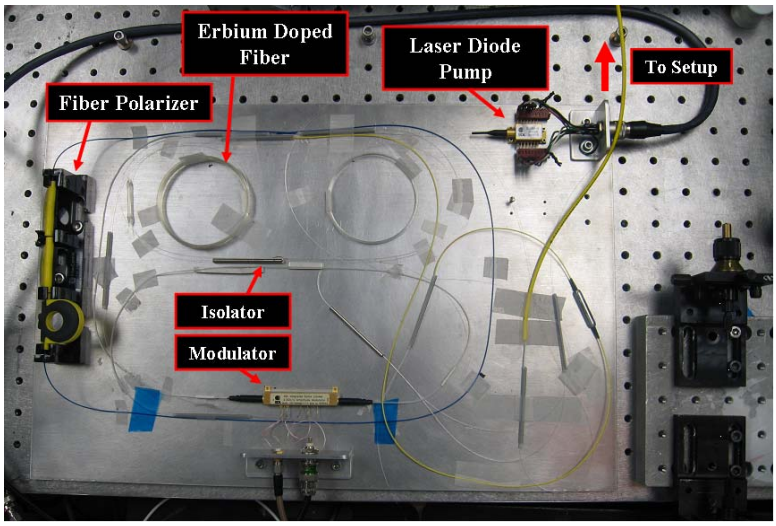

Figure 4.18 Harmonically mode-locking fiber laser.

4.5.2 Results and Discussion

In the first device, the waveguides were etched completely through the intrinsic core region down to the top of the lower InP cladding layer, giving a final ridge height of 610 nm. The access waveguides were about 3.5 μm wide at the guiding layer. The index modification trench was placed at $L = L/4$, and centered laterally so that it overlapped the second and third images of the first four-fold image set. The trench floor was positioned 255 nm above the uppermost InGaAsP layer. Testing was carried out using the experimental setup in Fig. 4.17. The pump beam was set to a wavelength of 1543 nm, and TE polarized to maximize carrier generation at the designated index modulation regions located at $L = L/2$ within the MMI waveguide, with the pump power at 7 mW when measured after the power combiner and before the lensed fiber. The signal beam from the tunable laser was set for a wavelength of 1556 nm and was TM polarized to minimize unwanted carrier generation within the device. When the signal beam was launched into either input waveguide, the majority of the light was directed to the crossed output port, with a splitting ratio of approximately 8:1.

Pump pulses with a repetition rate of 73 MHz were then launched into the same input port, and the switching response at the two output ports was measured. For this configuration, it is expected that the index modification trench will result in a carrier imbalance at the index modulation region, creating a localize change in the refractive index and altering the phase relation between the two images of the first two-fold image set for the signal beam. With the change in the phase difference, the 1556 nm signal light is transferred from the crossed output

port to the bar output port. This is clearly demonstrated in Fig. 4.19 which shows the up-pulse measured at the bar port and the down-pulse detected at the crossed port, with the transmitted signal wavelength confirmed using an optical spectrum analyzer to be 1556 nm. The recovery time of the switching pulses was determined to be 2.15 ns by applying an exponential fit to the decay curve. Higher repetition rates are possible if the pulse frequency of the mode-locked laser is adjusted. Fig. 4.20 shows 761.8 MHz switching pulses, though at this frequency, the carriers do not have time to fully decay before the next pulse arrives (1.31 ns). If the signal beam wavelength is varied, then the relative magnitudes of the switching pulses were altered, each one oscillating at intervals of 184 pm from maximum to minimum to maximum. This was determined to match the Fabry-Perot resonance of the device which had a total length from input facet to output facet of 1.86 mm.

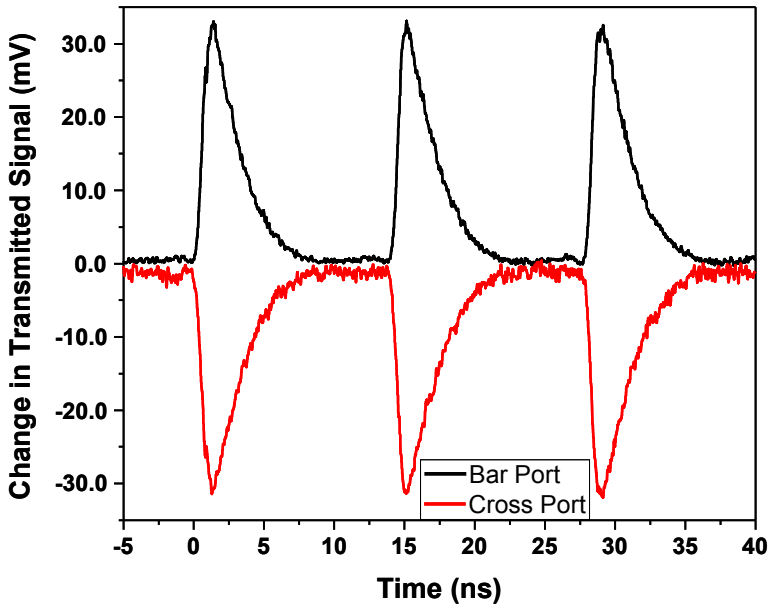

Figure 4.19 Switching response of multiple quantum well all-optical 2 x 2 MMI switch.

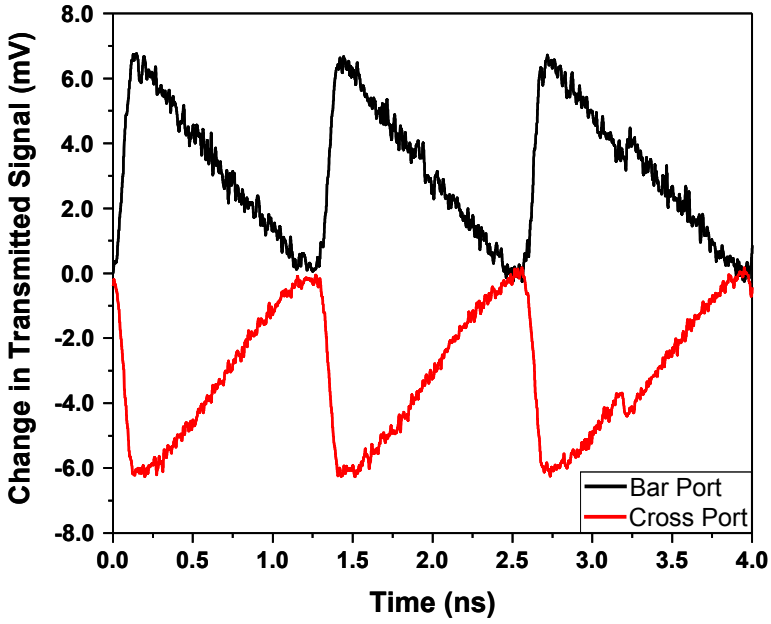

Figure 4.20 Switching response of multiple quantum well all-optical 2 x 2 MMI switch for 761.8 MHz pump beam with signal beam wavelength at 1555.25 nm.

4.6 Multiple Quantum Well All-Optical 2 x 2 MMI Device: Dual Control Pulses

4.6.1 Experimental Setup

In order to demonstrate that the device switching time could be improved through the use of dual pump (control) pulses, simultaneous access was required to both input ports. However, the separation between the input waveguides was not sufficient for employing more than one lensed fiber at a time. Therefore the experimental setup was reconfigured to accommodate free

space operation at the input side of the device which allowed both ports to be exploited during a single switching event.

The modified experimental setup is depicted in Fig. 4.21. Light from a Santec TSL-210 tunable, semiconductor laser, with an wavelength range of 1515 nm to 1595 nm (CW signal beam), was sent through a fiber-based polarization controller which allowed selection of either TE or TM polarized light. The optical beam then passed into a 2 x 1 power combiner so that it could be copropagated with picosecond light pulses from the pump beam. The pump (control) pulses from the actively mode-locked fiber laser passed through an EDFA to increase the pump power, and then through a DiCon tunable fiber bandpass filter ($\Delta\lambda_{bandwidth} \approx 1\ nm$) to remove the EDFA noise. The pulses passed into a power splitter to divide the beam into two separate control pulses (path *A* and path *B*). The polarization of the control pulses in each branch could be manipulated by a dedicated fiber polarizer. Path *A* contained a fiber delay so that the relative time delay between the control pulses could be adjusted. The control pulses in path *A* were then sent to a 2 x 1 power combiner where the picosecond pulses were copropagated with the CW signal beam. These two beams then passed from the power combiner into a fiber collimator, after which the beams were directed by mirrors to a 40 x microscope objective that end-fire coupled the light into one of the device input waveguides. The pump light in path *B* left the power splitter and was collimated by a second fiber collimator and directed by mirrors to the second device input waveguide. Light from the device output facet was collected with a SMF-28 lensed fiber and sent to an EDFA to enhance the signal pulse. The signal then passed through a DiCon tunable fiber bandpass filter ($\Delta\lambda_{bandwidth} \approx 3\ nm$) to remove any light remaining from the pump laser, as well as the EDFA noise. The signal was captured with a fiber pigtailed, 8 GHz InGaAs

photodetector (Ortel Corporation model #2860A receiver module). Data was gathered from a HP 83480A digital communications analyzer. The setup was arranged such that each pump beam could be disengaged without hindering propagation of the signal beam or the other pump beam. This allowed measurements to be taken with both pump beams at once, only one pump active at a time, or with the signal beam only.

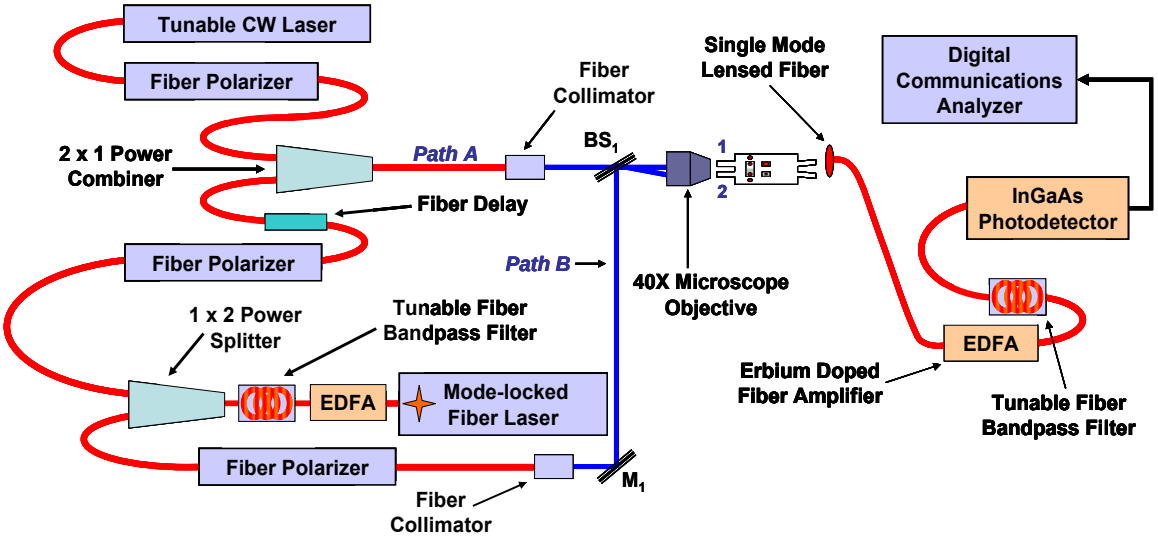

Figure 4.21 Experimental setup for dual path control of the multiple quantum well all-optical MMI switching devices.

4.6.2 Results and Discussion

Testing was conducted using the setup depicted in Fig. 4.21, with the pump beam set to a wavelength of 1543 nm and operating at a pulse frequency of approximately 73 MHz. Both pump beams (path A and path B) were TE polarized to maximize absorption, and therefore carrier generation, at the designated index modulation regions collocated with the first two-fold image at $L = L_\pi/2$ within the MMI waveguide. The waveguide was etched through the upper

cladding, giving a rib height of 370 nm. The signal beam from the Santec tunable laser was set for around 1556 nm and was TM polarized to minimize unwanted carrier generation. Due to the change in ridge height and the depth of the index modification trenches located at $L = L_{\pi}/4$ (235 nm above the InGaAsP layer), the phase relationships between the inner and outer images of the four-fold image set was altered such that the majority of the transmitted light was directed to the bar output port as opposed to the crossed port. The resulting split was approximately 7:1 between the two output ports.

With only the signal beam operational and launched into the device, the CW light is directed to the bar port at the output and no switching response is detected. If a control pulse is then sent into the same waveguide (port 1) along with the signal beam, a switching response is detected at the output, with light being transferred from the bar port to the crossed port, represented by a down-pulse measured at the bar output port. Blocking the control pulse from entering port 1 while maintaining the CW signal beam and sending a control pulse into the second input waveguide (port 2) results in an opposing response, and the light now shifts from the crossed port toward the bar port. For the purpose of comparison, the two switching responses measured at the bar output port are displayed in Fig. 4.22 in terms of the absolute value of the change in transmission. As can be seen, the control pulse sent into port 2 was time delayed by approximately 600 ps from the pulse sent to port 1. Additionally, the relative pump beam intensities were adjusted so that the amount of transmission change was precisely the same over the temporal range for which the two switching pulses overlapped. The duration for each switching pulse is set by the carrier lifetime, and the recovery time was calculated by fitting an exponential decay to the curve. The average recovery time for both output signals was

determined to be 1.65 ns, which is equivalent to the carrier lifetime and similar to the results from Fig. 4.19.

When the control pulses are each launched into their corresponding input waveguides (ports 1 and 2) with the same 600 ps time delay between them, the width of the switching pulse is reduced to ~ 600 ps (FWHM), as shown in Fig. 4.23. A smaller switching pulse width should be possible if better control over the relative delay between the control pulses is exercised. The lower limit of the temporal width is set by the control pulse duration (Fig. 4.24) which was measured to be 470 ps (FWHM), and the upper limited is dependant on the carrier lifetime. Thus, for the arrangement as-is, it is expected that the width of the switching pulse could be reduced to around 500 ps. If the width of the control pulses is also reduced, then double or single digit, picosecond switching pulses may be possible.

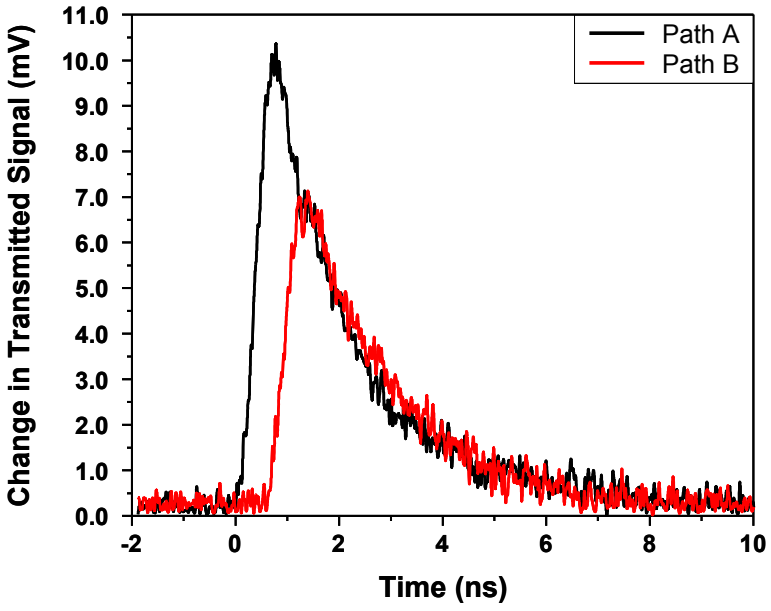

Figure 4.22 Output signals measured at the bar output port when control pulses are launched into either port 1 or port 2. Note the 600 ps time delay between the two pulses.

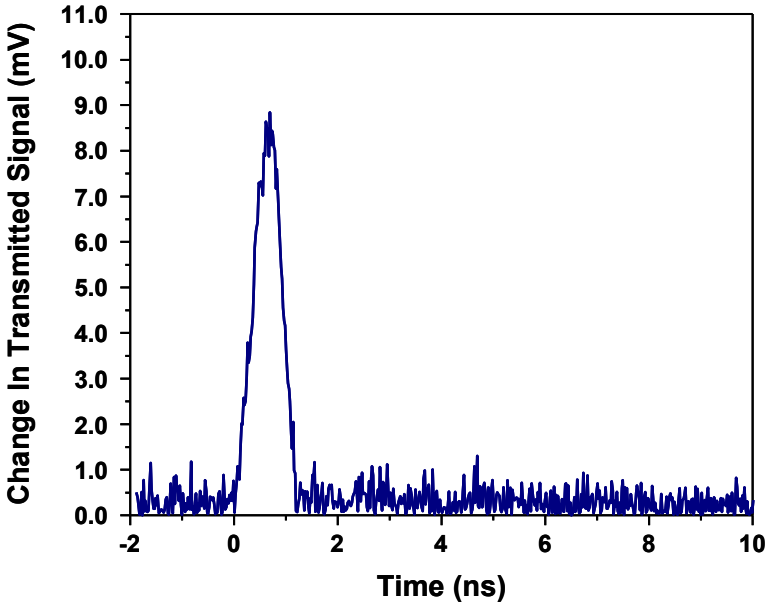

Figure 4.23 Output signal at λ = 1556 nm when control pulses are launched into both input ports.

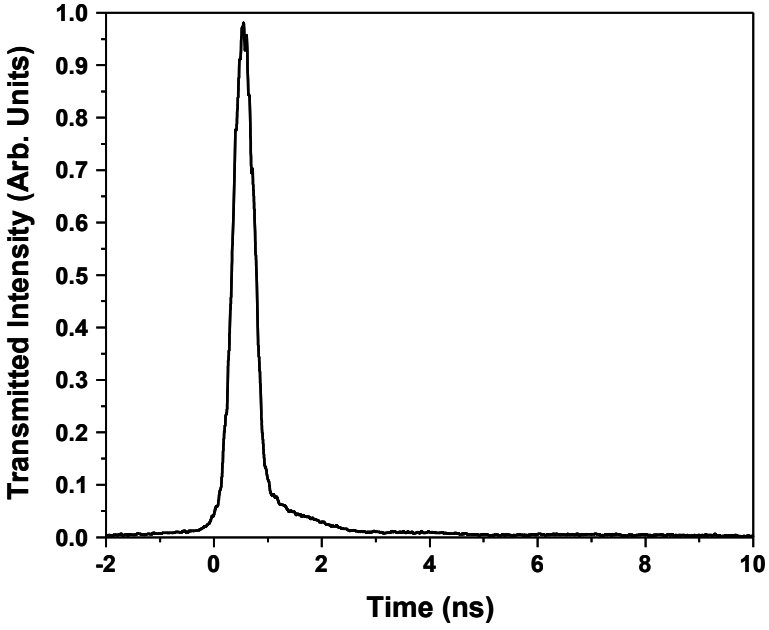

Figure 4.24 Profile of a control pulse at when the pulse repetition rate is 73 Mhz.

CHAPTER 5: SUMMARY AND FUTURE WORK

Part of this work was devoted to the expansion of post-growth material processing techniques in III-V semiconductors for the purpose of providing additional options in the monolithic integration of optoelectronic devices. Investigations into the difficulties of bandgap tuning in self-assembled quantum dots lead to the development of a low pressure, CF_4-based plasma treatment which was demonstrated to reliably inhibit the interdiffusion of In and Ga atoms in $In_{0.15}Ga_{0.85}As/GaAs$ self-assembled quantum dot wafer structures subjected to rapid thermal annealing at temperatures between 700°C and 800°C for a duration of 20s. This method was used to supplement the area selectivity of the impurity free vacancy disordering and provided improved control over the degree of bandgap shift. A bandgap differential of 84 meV (94 nm) was observed between wafer sections that were uncapped and treated with the CF_4 plasma versus sections that were raw, annealed-only, when annealed at 775°C for 20 seconds. These results were evaluated against capping the wafer material with TiO_2 [39, 43], a prominent technique for suppressing thermal disordering in quantum dots, and found to be comparable, with the plasma treatment shown to be slightly more effective for the samples studied. It was observed that the same plasma treatment when applied to InGaAsP/InGaAsP MQWs, which were then subjected to rapid thermal annealing, produced an additional blue-shift in the bandgap emission compared to raw, annealed only samples. It was hypothesized that the interaction of the plasma with the wafer surface differs substantially for the two material systems, one which is GaAs based (SAQD) and the other which is InP based (MQW). This reasoning is supported by studies on plasma damage [68] which noted differences in the types of defects formed in GaAs

and in InP. Characterization of plasma-surface interactions is shown to be critical in selecting which fabrication methods to employ for work conducted prior to high temperature annealing when dealing with III-V MQW and SAQD.

In addition, a sputter etching process was developed for ridge waveguide formation in GaAs/AlGaAs material systems as an alternative to standard ion-assisted etching techniques that involve a combination of chemical and physical etching. The masking layer was specifically developed to provide good selectively (1:10) with respect to the wafer material and to be easily removed after etching was complete. The rate of material removal was quite slow, with an etching rate of 10.4 nm/min, but this was found to be adequate for fabricating the SAQD waveguide structures used in section 4.4 when combined with wet chemical etching to compensate for the angled sidewall. While impractical for manufacturing settings, the procedure is suitable in research environments and is extremely useful for situations where typical GaAs/AlGaAs etching gasses are not available and long etching times can be accommodated.

In the second part of this dissertation work, tunable 2 x 2 MMI couplers were fabricated to study the effects of current injection in self-assembled quantum dot devices. The tunable variable power splitter was used for this task as the device's transmission response differed depending on the polarity of the refractive index change. Sub-microsecond electrical current pulses applied to this device demonstrated that the carrier induced change in the refractive index rapidly saturates, limiting the applications of self-assembled quantum dots in the production of efficient active multimode interference switching devices which have a short interaction length. However, the thermo-optic response was shown to be quite large and the tuning range of the variable power splitter was comparable to MQW devices using a similar design [80, 90]. A

broadly tunable 2 x 2 MMI cross-coupler switching device fabricated with $In_{0.15}Ga_{0.85}As/GaAs$ SAQD wafer material was also demonstrated. Designed for current injection control, the operative nonlinearity for the device was predominately thermo-optic in nature. When probed with a 1.31 μm wavelength laser beam, the device showed similar responses for TE and TM polarization with initial split ratios of 1:29 (TE) and 1:48 (TM) that were continuously adjustable to a 49:1 (TE) and 38:1 (TM) split ratios when a current change from 0 mA to 24 mA was applied to one of the electrodes. A 50:50 split ratio was reached at a current of 17 mA and crosstalk values better than -15 dB were achieved. The response time was shown to be on the order of 1 μs, which is several orders of magnitude longer than the carrier induced effects. In spite of that limitation, there are a number of possible applications including use in add-drop multiplexers for wide-area and metro-area networks, as components in optical cross connects, as a variable power splitter and variable optical attenuator, and in place of Mach-Zehnder switches in channel demultiplexing of OTDM signals.

The third portion of this work dealt with all-optical control of MMI switching devices. In order to produce these devices, two major issues were resolved to allow use of in-plane excitation of the all-optical switch. First the bandgap tuning techniques from section 2.1.2, and section 2.2.1, were employed to shift the bandgap of the SAQD and MQW materials to higher energy. This increased transmission of the pump and signal beams through the device, and eliminated unwanted carrier generation outside the index modulation regions. The second challenge was the need to control the distribution of photogenerated carriers between the two index modulation regions at *L/2*. An imbalance in the carrier distribution was required to create the necessary phase shift between the images at the first two-fold image set. A simple

modification to the waveguide structure was used to create this disparity in power distribution without significantly changing the device function. In the case of the tunable 2 x 2 MMI cross-coupler, narrow trenches overlapping the center two images at the four-fold image location and etched down to within several hundred nanometers of the intrinsic region altered the power distribution between the images of the two-fold image set at the index modulation region. By controlling the precise depth, any fixed power ratio between the two-fold images was obtainable. Combining these two approaches together into a variation of the 2 x 2 MMI cross-coupler produced a working all-optical switch using MQWs as the active material. Additional investigations into the response of $In_{0.15}Ga_{0.85}As/GaAs$ SAQD to photogenerated carriers utilized a simple Fabry-Perot etalon. Wavelength conversion was demonstrated and the effect of an applied reverse bias field was documented.

5.1 Future Work: Bandgap Control in Self-Assembled Quantum Dots

Testing is required to quantify the full extent to which the RF power level influences the suppressive nature of the CF_4 plasma treatment in regards to $In_{0.15}Ga_{0.85}As/GaAs$ SAQD. In section 2.1.1.1, an applied RF power of 75 W was suggested as the critical value for suppression of thermal disordering. However, the possibility remains that there is a continuum of change, as opposed to an abrupt cut-off, between 25 W and 75 W. If such a continuum exists then it would provide a means of tuning the degree of suppression. Further investigation should also be carried out to determine whether suppression or enhancement of the thermal disordering is observed in other III-V material systems, as well as for more exotic materials such as gallium nitride and

indium gallium nitride. This would provide a means of confirming the hypothesis presented in section 2.2.1.2 regarding surface composition being the determining factor in the differences observed between the $In_{0.15}Ga_{0.85}As$/GaAs SAQD and the InGaAsP/InGaAsP MQW when exposed to the CF_4 plasma.

5.2 Future Work: SAQD Based Thermo-Optic Switches

The use of the current isolation trenches offers some interesting prospects for manipulating the gating widow of the 2 x 2 MMI cross-coupler devices presented as a thermo-optic switch in section 3.6. The presence of the trenches was shown to produce an initial fast component to the thermal recovery. If electrical current pulses are applied to both contact pads, and a slight time delay (~ 200 ns) is imposed between the control pulses, then the index change due to the thermal nonlinearities should cancel out, eliminating the thermal recovery tail that extends out for several microseconds after the electrical pulse is terminated. Sub-microsecond thermo-optic based pulse switching should then be possible.

5.3 Future Work: MQW Based All-Optical MMI Switching

Refinement of the all-optical MQW-based MMI switching device to better control the depth of the index modulation trench at *L/4* and therefore the power distribution at the index modulation regions should still provide adequate index change but minimize the degradation of the off-state splitting ratio. Additionally, applying the use of the index modulation trenches to an

MMI Mach-Zehnder will allow in-plane all-optical switching using SAQD. The phase-shifting arms of the Mach-Zehnder will permit sufficient accumulation of a phase difference between the two images that was not possible in the compact MMI device when SAQD were used as the active material.

CHAPTER 6: APPENDIX – LATERAL CONFINEMENT AND THE FABRICATION OF ETCHED QUANTUM BOXES

Quantum dots exhibit several distinct advantages over quantum wells, including enhanced optical and electro-optical nonlinearities [19-21] and a controllable alpha parameter [101], which are properties pertinent to the fabrication of devices for signal generation as well as all-optical and electro-optical switching. However, the most successful approach for creating QD semiconductors is the Stranski-Krastanow self-assembled growth method. QDs formed in this manner often exhibit significant size distribution and therefore a broadening of the absorption transitions. This fact renders self-assembled quantum dots (SAQD) less than suitable for use in electro-optical and all-optical switching devices, despite the high success of these structures in the fabrication of other optoelectronic devices such as quantum dot laser diodes [12, 13] and quantum dot infrared photodetectors [102, 103].

We propose to utilize an alternative scheme, by which layers of QD arrays are produced by electron beam lithography coupled with the reactive ion etching (RIE) of epitaxially grown multiple quantum wells (MQW) [104]. These etched quantum dot arrays show a high degree of size uniformity and, consequently, a low spread of the electron transitional energies. Several past attempts to capitalize on this technique [63, 105, 106] have not been pursued in more recent times, because the high density of non-radiative defects that are created during the etching process result in low internal quantum efficiency for light emission and photon detection. In contrast, the non-radiative recombination is not a hindrance for electro-optic and all-optical devices, and could in fact be advantageous for fast device recovery times [107, 108].

At further issue is the number of SAQD layers that can be stacked. This can be limited by strain accumulation in the active region which leads to a buildup of point defects in the QD layers [109]. As a consequence, limitations on the number of SAQD layers would restrict the

size of the active region and reduce the extent of the third order nonlinear effect imparted by the QDs. One of the principle benefits of the etched quantum boxes will be the ability to tailor the vertical dimension and composition of the structures through standard epitaxial deposition (MOCVD & MBE) of the multiple quantum well material. The formation of high quality, quantum well stacks with any particular number of layers can be readily achieved with current growth techniques. Therefore the potential exists for the formation of uniform, three dimensional quantum box arrays which, in the presence of an electric field applied parallel to the growth direction, can realize an enhanced shift in the bandgap energy compared to SAQD, and thereby lead to smaller, more energy efficient devices.

6.1 GaAs/$Al_{0.3}Ga_{0.7}$As Multiple Quantum Well Wafer

The GaAs/$Al_{0.3}Ga_{0.7}$As MQW wafer (W1218), was grown using molecular beam epitaxy on an n+ GaAs substrate. All layers were n-type, except for the active region which is nominally undoped (Fig 6.1). Growth began with the formation of a 3.0 μm $Al_{0.3}Ga_{0.7}$ As buffer layer on top of the substrate, followed by a 400 nm $Al_{0.3}Ga_{0.7}$ As lower cladding layer. The active region contained ten GaAs well layers, each 8 nm thick, which were interleaved with eleven $Al_{0.3}Ga_{0.7}$As barrier layers, also each 8 nm thick. The upper cladding was 500 nm of $Al_{0.3}Ga_{0.7}$As and the structure was capped by a 50 nm GaAs contact layer. The room temperature photoluminescence peak was measured at 839 nm with a FWHM of 18 nm (Fig. 6.2). The doping concentration in the contact layer was 5 x 10^{14} cm^{-3} and the concentration in the AlGaAs

cladding layers is approximately 5 x 10^{14} cm^{-3} for the upper cladding and 1 x 10^{17} cm^{-3} for the lower cladding.

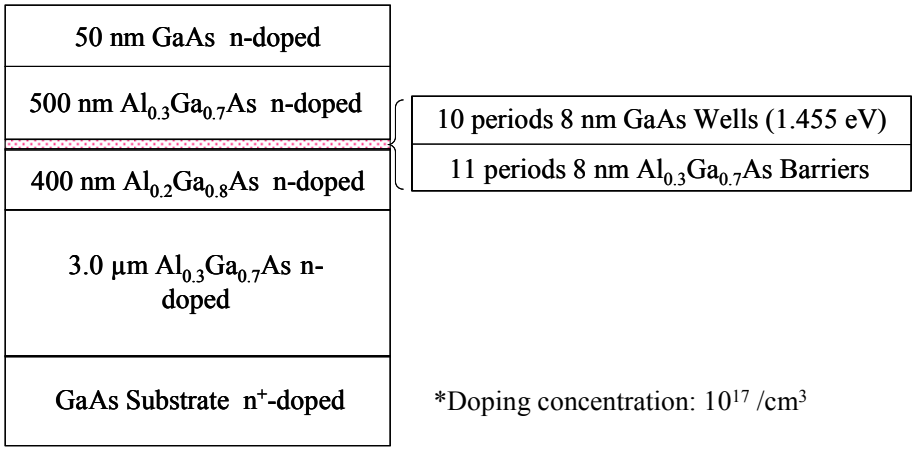

Figure 6.1 GaAs/$Al_{0.3}Ga_{0.7}As$ MQW wafer structure.

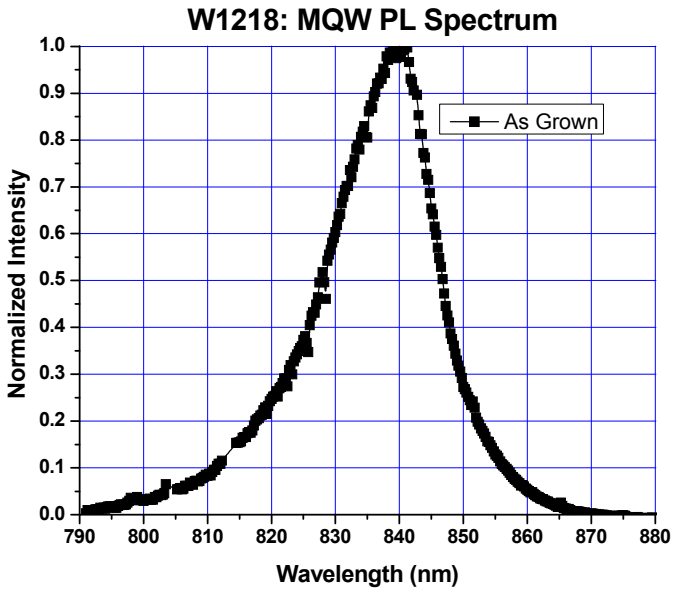

Figure 6.2 GaAs/$Al_{0.3}Ga_{0.7}As$ MQW photoluminescence measurement.

6.1.1 Bandgap Tuning

Initial characterization steps were primarily concerned with understanding the material's photoluminescence (PL) and intermixing properties. Toward this end, the PL was measured for the "as grown" condition and also after being subjected to rapid thermal annealing (RTA) at several different temperatures inside a Heatpulse 210 AG Associates annealing furnace. Both impurity free vacancy disordering (IFVD) and thermal intermixing tests were initiated. In order to minimize process related variations, IFVD and thermal intermixing tests, for identical temperature values, were annealed together. The annealing time at the target temperatures was, for all cases, 30 seconds. Photoluminescence data was acquired at room temperature (300˚K) using an Argon-Ion beam at 514 nm as the excitation source and the emission was collected by a Scientific Measurement Systems (SMS) monochromater configured for use as a spectrophotometer.

In the case of the IFVD tests, 220 nm of PECVD SiO_2 was deposited on the samples with a PlasmaTherm 790 Series PECVD system to stimulate the creation of group III vacancies by the movement of surface Ga atoms into the silica layer. Diffusion of vacancies into the active layer promotes the inflow of Al into the well layers and an outflow of Ga into the barriers. This should result in a widening of the optical bandgap (Fig 6.3) within the quantum wells [110] and a shift of the emission properties to shorter wavelengths. Thermal intermixing, which should also yield a shift of the bandgap energies to shorter wavelengths, is expected to function primarily through exchange of Ga and Al caused by ingrown vacancies, which formed during the MBE growth

process [37, 38]. Since few such vacancies are generally present, and are fixed in number, a much smaller shift in the PL is expected than with IFVD. Both of these techniques are appropriate for bandgap tuning, which can be particularly valuable in the monolithic integration of multiple device functions.

The group V constituents of the active layer do not contribute to the bandgap tuning in any significant amount since that the Arsenic (As) concentration is identical for both wells and barriers. However, one concern during thermal intermixing involves the outgassing of As, which presents the possibility of damage to the wafer surface and a decreased PL. This potential was mitigated during the testing by sandwiching each sample between two pieces of bulk GaAs wafer with the epitaxial layer facing down. Such an arrangement provides an As overpressure that limits the outflow of As from the sample.

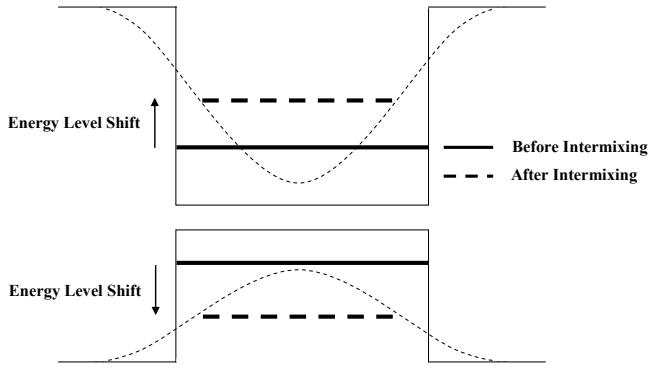

Figure 6.3 Bandgap energy diagram before and after intermixing.

The normalized results of the PL testing are shown in Fig. 6.4. For the sample which underwent IFVD, the emissions peak was blue-shifted approximately 50 nm. Conversely, for the sample which was thermally intermixed, the emission spectrum only shifted 4 nm. This

difference in the PL peak shift between the IFVD sample and the intermixed sample is large enough for most bandgap tuning applications. This will allow for selective intermixing of a planar waveguide device, permitting monolithic integration of both active and transparent regions.

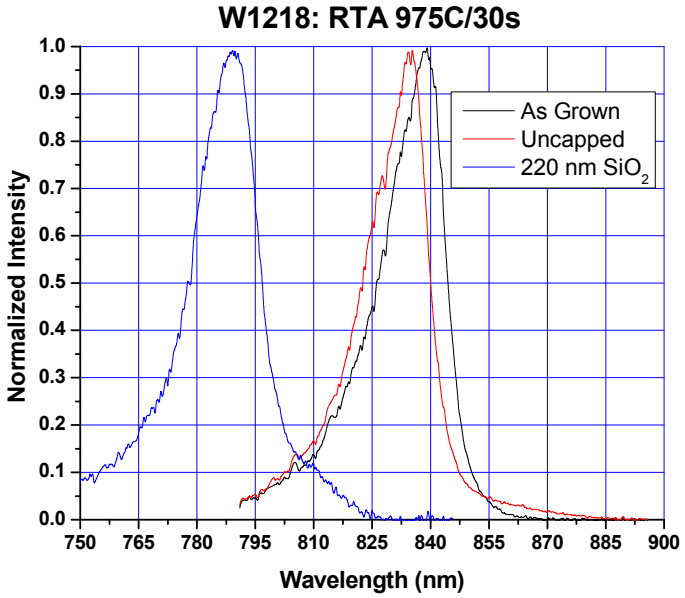

Figure 6.4 Photoluminescence spectra from MQW intermixing tests.

6.2 Design and Fabrication

The goal of this work was to produce organized arrays of quantum boxes (dots) etched from an existing MQW epitaxial material with uniform size and shape. SAQD are typically around 20 or 30 nm in diameter, necessitating the use of nanoscale fabrication techniques. The eventual epitaxial structure in which the quantum boxes would be formed is the MQW wafer

described in section 6.1. The upper cladding and intrinsic region are in total around 712 nm thick (Fig 6.1). Therefore, for quantum confinement to be successfully imposed in the lateral direction for the entire MQW stack, nanopillars approximately 750 nm high would be required. This would imply an aspect ratio better than 1:25. To meet such stringent tolerances requires the use of dry etching techniques as traditional wet chemical etching is highly isotropic. As best, WCE can be expected to produce little better than a 1:1 aspect ratio in GaAs based materials. In order to develop the fabrication techniques and the processing steps required, nanopillars were first created using GaAs mechanical wafers.

To achieve the necessary feature sizes for the QD arrays, a Leica EBPG5000+ Electron Beam Lithographic System was employed, having a minimum spot size < 10 nm. The electron beam (e-beam) resist chosen for patterning the arrays was 950K PMMA (positive) e-beam resist at 4% in Anisole due to the high resolution of nanoscale features and ease of processing. PMMA has a poor dry etching resistance compared to GaAs based materials and it was readily etched at a rate of approximately 100 nm/min using a weak oxygen plasma (40 W RF Power) in a PlasmaTherm 790 reactive ion etcher. For this reason, PMMA cannot be used as a direct etch mask for this work. It can however be easily removed with acetone at room temperature making it useful as a liftoff resist for selective metal deposition and the creation of a combination metal/dielectric masking layer. It is also considerably less expensive than most other alternatives, such as ZEP, making it cost effective in comparison.

Chromium was chosen for main portion of the etch mask as it possess good adhesion to silicon dioxide and is highly resistant to CF_4-based and BCL_3-based etching processes. In addition, chromium tends not to redeposit during these etching processes, preventing the creation

of micromasking sites on the sample surface, which could damage the uniformity of the pillar arrays.

6.2.1 Sample Preparation

The sample was cleaned by doubly rinsing the wafer sample with a sequence of acetone, methanol, and isopropanol, to eliminate any organic residue, and then drying by gently blowing with N_2 gas. This was followed by submersion in buffered oxide etchant (BOE) for 4 minutes to remove any native oxide. The sample was then rinsed in deionized water (DI) for 120 seconds and finally by repeating the acetone and alcohol rinsing sequence. The substrate was dried as before and then baked for 3 minutes at 120°C on a hotplate to remove any remaining volatiles from the wafer surface.

6.2.2 Design Approaches: Crosshatched Exposure

Two approaches were investigated for creating the initial metal masking layer and were tested concurrently. One technique, which was designated the crosshatched method, involved the growth of PECVD SiO_2 on top of the prepared GaAs substrate. This was followed by a 20 nm layer of chromium metal deposited via thermal evaporation. A 950K PMMA (positive) e-beam resist at 4% in Anisole was diluted 1:1 by volume with Anisole (99%) and spun onto the GaAs substrate at 5000 rpm for 40 seconds. This produced a uniform PMMA film approximately 70-

nm thick. A hotplate was preheated to 170°C, and the sample baked at this temperature for 5 minutes.

In this approach, two sets of lines were written on the sample using the Leica 5000+ e-beam writing system. In the first set, lines were separated by 200 nm center-to-center. The second set of lines was identical to the first, but rotated by 90 degrees, such that the two sets overlapped at right angles, creating a crosshatch pattern of exposed resist. Electron beam current was set to 500 pA, the accelerating voltage was 50 keV, and the exposure dose was 225 $\mu C/cm^2$. A solution of MIBK:IPA (1:3) was used as the developer to provide high contrast features. The sample was held motionless in the developer for 45 seconds to remove the exposed resist, then rinsed in DI water for an additional 45 seconds and dried with N_2 gas. This left behind an array of PMMA islands on top of the chromium layer. Different line spacing and exposure doses were used to vary both diameter and periodicity of the PMMA island arrays. A SEM picture showing a 200 nm period array of islands which were formed using an electron dose of 675 $\mu C/cm^2$, is shown in Fig. 6.5, with each island approximately 125 nm in diameter. The islands appear rounded as opposed to the expected square shape due to the double e-beam exposure at the crossing points of the written lines and the small periodicity of the array. Larger periodicities for the same exposure dose, yielded square islands with slightly rounded corners.

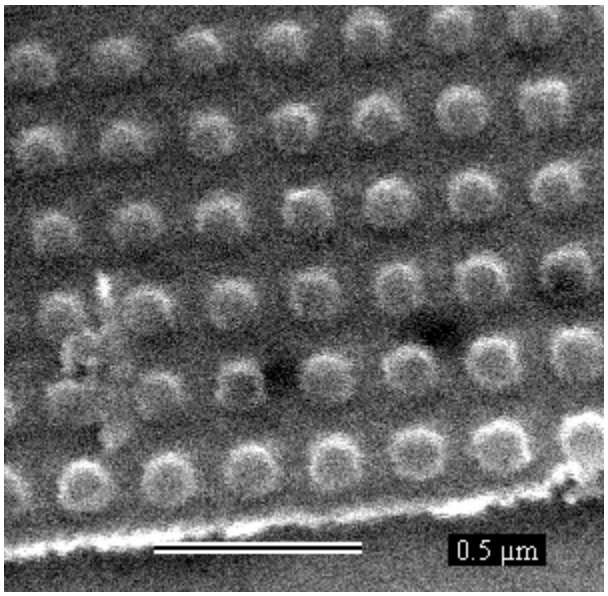

Figure 6.5 SEM image: Crosshatched pattern in PMMA with 200 nm period.

The samples were then placed in a chromium etchant to remove any exposed metal, thereby creating etch masks for the dry etching of the SiO_2. As the Cr etching was primarily isotropic in nature and prone to undercutting, the island diameter was larger than the target diameter of the desired nanopillars. However, it proved difficult to produce repeatable results. The desired diameter of the dots was on the order of the metal thickness and even slight variations in etching time or etchant concentration proved problematic, often completely removing the Cr metal. Further work on this approach was abandoned in favor of the second method.

6.2.3 Design Approaches: Single Shot Exposure

The second approach was named the single-shot method. In this approach, the e-beam resist was exposed by single exposures, each corresponding to an individual nanopillar. For the initial case, 165 nm of PECVD SiO_2 was deposited on top of the prepared GaAs substrate. A 70 nm thick film of 950K PMMA e-beam resist was spun upon the SiO_2 and prepared in the same manner as the crosshatched method described in Section 6.2.2. Electron beam current was set to 500 pA, the accelerating voltage was 50 keV. The pattern design and exposure parameters were chosen such that the e-beam writer would expose only a single spot and then move to the next position in the array and expose another spot. This would repeat until the entire 2-D square array was finished. A dose matrix was run to determine the optimum exposure parameters for a given resist, resist thickness and substrate type, and the exposure dose of 225 $\mu C/cm^2$ was chosen for the sample under discussion. Again a solution of MIBK:IPA (1:3) was used as the developer, with the sample was immersed in it for 45 seconds to remove the exposed resist, then rinsed in DI water for an additional 45 seconds and dried with N_2 gas. The result was an array of holes in the PMMA, with negative profiles suited for metal liftoff.

A layer of chromium metal 30 nm thick was then deposited via thermal evaporation. The sample was soaked in acetone to lift off the extraneous PMMA and metal, leaving behind a square array of metal disks. This approach produced arrays of metal disks that had highly repeatable disk diameter and array uniformity. The procedure was refined and the final process is given in the next section.

6.2.4 Nanopillar Fabrication

The full fabrication process developed for the creation of nanopillar arrays in GaAs based semiconductor materials begins with the deposition of 400 nm of silicon dioxide on the surface of a GaAs wafer sample, using a dual system PlasmaTherm 790 PECVD/RIE reactor. This is followed by the spinning of a 70 nm coating of PMMA 950K electron beam resist. The desired dot array is then written using a Leica EBPG5000+ Electron Beam Lithographic System with the beam current at 500 pA, the electron dose set at 740 $\mu C/cm^{2,}$ and a 50 keV accelerating voltage, with each exposure representing the placement of a particular nanopillar. A solution of MIBK:IPA (1:3) was again used as the developer, but with the sample immerse motionless for 60 seconds, then rinsed in Isopropyl Alcohol for 30 seconds, subsequently rinsed in DI water for an additional 45 seconds, and finally dried with N_2 gas. Atomic force microscopy (AFM) was used to examine the patterns and Fig. 6.6(a) and Fig. 6.6(b) show images of square lattice dot arrays in PMMA e-beam resist with 100 nm and 200 nm periods respectively.

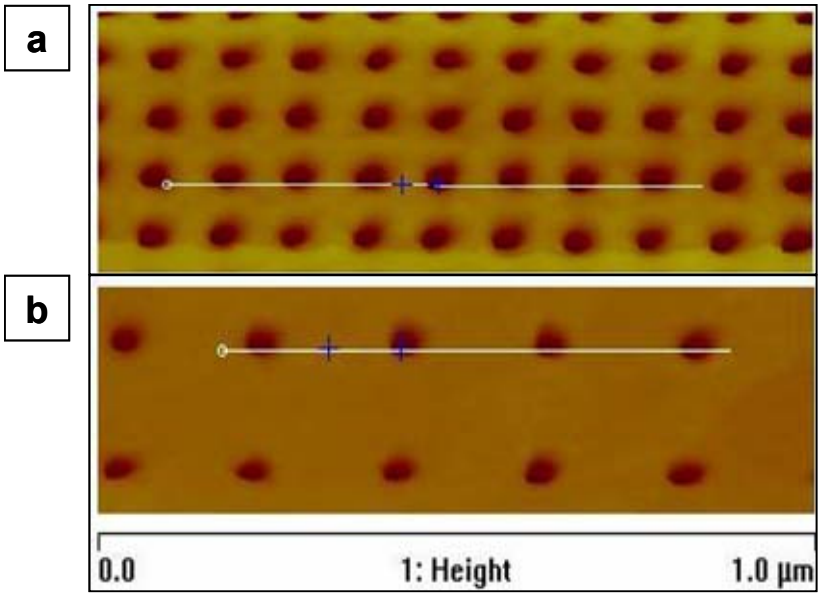

Figure 6.6 AFM image: Dot pattern in e-beam resist: (a) 100-nm period and (b) 200-nm period.

Following the development of the electron beam resist, a 30 nm thick layer of chromium was evaporated onto the patterned area via thermal evaporation and the extraneous metal was removed by immersing the sample in acetone. This process left behind an array of metal disks (Fig. 6.7), corresponding to the holes that had been patterned in the PMMA. These Cr disks acted as the etch mask for the underlying SiO_2 layer, the uncovered portion of which was then etched using a highly anisotropic CF_4-based RIE process (Table 6.1) developed in the course of this work. This procedure produced highly vertical, 400 nm high silicon dioxide nanopillars that are approximately 40 nm in diameter (Fig. 6.8). The pattern was then transferred into the GaAs/AlGaAs MQW with a BCl_3-based etching process, and carried out in an UNIAXIS ICP-RIE III-V reactor. The ICP-RIE system offers separate control of the plasma density and ion energy, allowing for highly anisotropic etching profiles. Following the III-V etching step, any metal or silicon dioxide that remained from the masking layer was removed by soaking the

sample in a buffered oxide etchant. The planarization compound (SU-8) was then applied for structural support of the semiconductor columns.

Table 6.1 Etching process for high aspect ratio silica nanopillars.

Silicon Dioxide CF_4-Based RIE Process	
CF_4 Flow	5 sccm
Residual Pressure	6 mT
RF Power	125 W
SiO_2 Etch Rate	16 nm/min

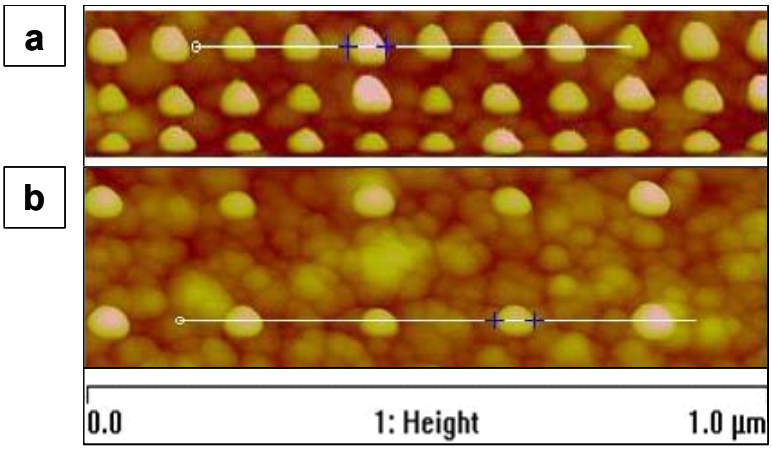

Figure 6.7 AFM image: Cr islands after metal deposition and liftoff: (a) 100-nm period and (b) 200-nm period.

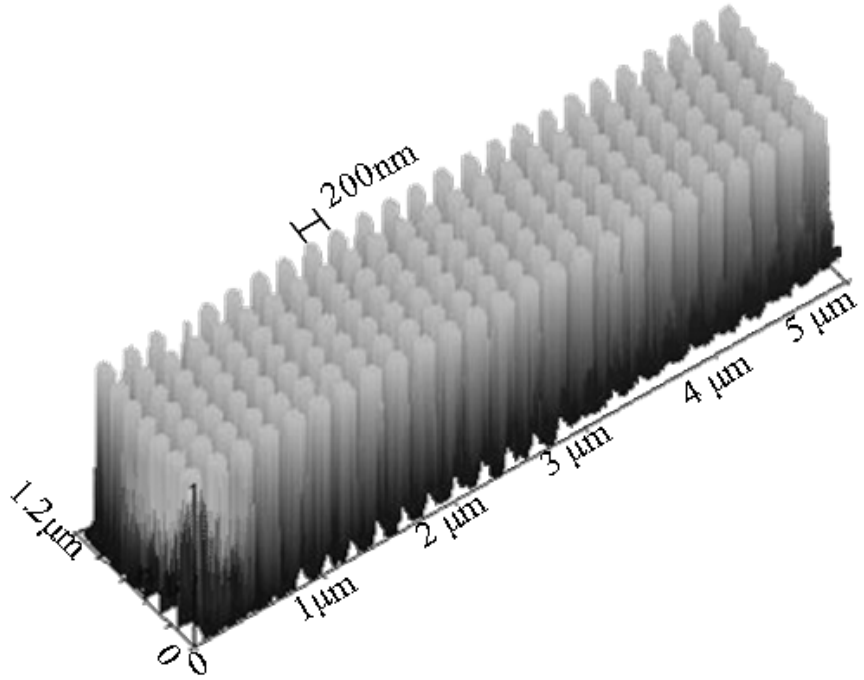

Figure 6.8 AFM image of silicon dioxide nanopillars on GaAs surface.

A scanning electron microscope (SEM) was used to image the nanopillar arrays and provide information on the etching profile, the pillar diameter and the pillar height. To date, we have produced arrays of GaAs nanopillars that have a diameter of approximately 43 nm and a height of 550 nm, as shown in Fig. 6.9. The arrays are laid out in a square lattice, with the smallest period achieved being 200 nm.

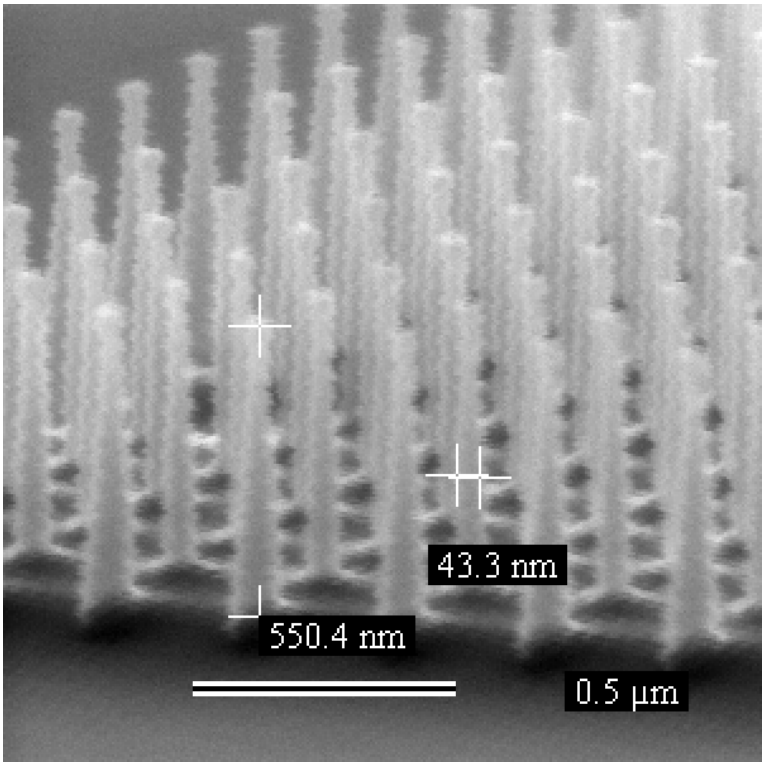

Figure 6.9 SEM image of 43-nm gallium arsenide pillars etched in ICP-RIE reactor.

6.3 Discussion

In principle, the columns of semiconductor material which remain after the ICP-RIE etching process will contain a number of laterally confined quantum wells or quantum boxes (i.e. etched quantum dots). One of the indications that quantum confinement is present in the etched structures is a blue-shift of the photoluminescence spectrum compared with that measured from the as-grown material. For a particular material system and quantum well thickness, this blue-shift is dependent upon the lateral size of the etched quantum dot. For a GaAs/AlGaAs system at room temperature, the lateral dimensions of the nanopillars need to be reduced to a diameter of 20 nm to 30 nm in order to attain a significant shift in the photoluminescence spectrum [111].

Patterned resist features and metal dot formation in this range of diameters can be accomplished with currently available electron beam lithography techniques and technology [112]. Since the multiple quantum well materials utilized in this project contain quantum wells that are buried deeply, the particular challenge to this work has been to realize a high aspect ratio coupled with a dot diameter that does not exceed 30 nm. Etch depths described to date have generally been very shallow, with columns ranging from 50 nm to 200 nm in height, placing the etched quantum dots very near the surface of the epitaxial layer [63, 105]. Deeper etchings and aspect ratio's exceeding 10:1 have been reported, though the pillars were 100 nm in diameter or greater [113]. Our most recent results show GaAs pillars which exceed a 12:1 aspect ratio with pillar diameters approaching 40 nm (Fig. 6.9).

Highly anisotropic etching and high selectivity of the etch material over the masking material for both the SiO_2 and the GaAs/AlGaAs is crucial for the formation of small diameter, high aspect ratio semiconductor pillars. In the case of the oxide etching, the PlasmaTherm 790 tool is a parallel plate RIE system, without independent control of the plasma density and ion energy. This can be compensated for by balancing the residual pressure against the applied RF power. An extremely low residual pressure of 6 mTorr is matched to a moderate RF power of 125 W, resulting in good selectivity (> 1:13) between the Cr mask and the SiO_2, and an almost 90 degree etch profile. However, there is tradeoff in a low, 16 nm/min etch rate. The ability to separately manipulate the plasma density and ion energy, as provided by the UNIAXIS ICP-RIE III-V reactor, which was used in etching the GaAs and AlGaAs materials, can allow for a higher etch rate while maintaining close to a 90 degree etch profile. Since a 90 degree etch profile is of predominant importance the etch rate must be sacrificed. As the ICP independently provides a

high density plasma source, the etch rate can be increased to the range of 150 nm/min to 250 nm/min. Selectivity between the etch mask and the GaAs is not as critical as in the case of the SiO_2 pillar formation due to the thickness of the SiO_2 masking layer.

The lateral packing density for the nanopillars discussed above is comparable to that achievable for self-assembled quantum dots (SAQD) ($10^9/cm^2$ to $10^{11}/cm^2$) in GaAs based systems [114]. For etched quantum dots with a 30 nm diameter and a 100 nm center-to-center spacing in a square lattice, the dot density is approximately $10^{10}/cm^2$. Currently we have produced nanopillar arrays with a packing density of 0.25 x $10^{10}/cm^2$. As noted in the introduction, however, the active region of a MQW extends into the third dimension though layer stacking. Whereas the number of SAQD layers in a stack can be limited due to the effects of strain accumulation [109], the number of etched quantum dot layers in a stack is only restricted by the number of quantum well layers that can be grown. For example, by employing standard epitaxial deposition (MOCVD & MBE), MQW stacks consisting of 400 wells have been grown [115]. Notably, it is difficult to set a precise limit on the number of good quality SAQD layers that can be formed in a stack, as this is dependent on many parameters, including barrier layer thickness and the material system employed. For epitaxial growth of MQWs, the primary parameters are influenced by the intended application of the material. Finally, further improvement of the in-plane packing density can be accommodated by a controlled reduction of the center-to-center spacing, as well as by shifting from a square lattice to a hexagonal lattice.

LIST OF REFERENCES

1. Agrawal, G.P., *Fiber-optic communication systems*. 3rd ed. 2002: Wiley-Interscience.

2. Tajima, K. and J. Zhou, *Ultra low loss and long length photonic crystal fiber*. 2005, IEICE. p. 870-875.

3. Gruner-Nielsen, L., et al., *Dispersion-compensating fibers.* Lightwave Technology, Journal of, 2005. **23**(11): p. 3566-3579.

4. Harun, S.W., et al., *An overview on S-band erbium-doped fiber amplifiers.* Laser Physics Letters, 2007. **4**(1).

5. Shah, L., et al., *High-power ultrashort-pulse fiber amplifiers.* IEEE Journal of Selected Topics in Quantum Electronics, 2007. **13**(3): p. 552-558.

6. Gnauck, A.H., et al., *High-capacity optical transmission systems.* Journal of Lightwave Technology, 2008. **26**(9): p. 1032-1045.

7. Morita, I., *Enabling Technologies for 40 Gbit/s-Based Ultra-Dense WDM Transmission.* Review of Laser Engineering, 2005. **33**(2): p. 106-110.

8. Sano, A., et al. *Recent Progress in High-Speed and Large-Capacity Optical Transmission Technologies*. 2007.

9. Anscombe, N., *Join up the quantum dots.* Nature Photonics, 2007. **1**(7): p. 360-361.

10. Nishi, K., H. Saito, and S. Sugou, *Temperature-insensitive luminescence linewidth from highly-uniformstrain-reduced InAs quantum dots.* Nanostructures and Quantum Dots/WDM Components/VCSELs and Microcavaties/RF Photonics for CATV and HFC Systems, 1999 Digest of the LEOS Summer Topical Meetings, 1999: p. I25-I26.

11. Shoji, H., *Self-assembled quantum dot lasers.* Self-assembled InGaAs/GaAs quantum dots, 1999: p. 241.

12. Bhattacharya, P., et al., *Carrier dynamics and high-speed modulation properties of tunnel injection InGaAs-GaAs quantum-dot lasers.* IEEE Journal of Quantum Electronics, 2003. **39**(8): p. 952-962.

13. Liu, H.Y., et al., *Improved performance of 1.3 m multilayer InAs quantum-dot lasers using a high-growth-temperature GaAs spacer layer.* Applied Physics Letters, 2004. **85**: p. 704.

14. Zhang, Z.Y., et al., *High-performance quantum-dot superluminescent diodes.* IEEE Photonics Technology Letters, 2004. **16**(1): p. 27-29.

15. Akiyama, T., et al., *An ultrawide-band semiconductor optical amplifier having an extremely high penalty-free output power of 23 dBm achieved with quantum dots.* IEEE Photonics Technology Letters, 2005. **17**(8): p. 1614-1616.

16. Akiyama, T., M. Sugawara, and Y. Arakawa, *Quantum-dot semiconductor optical amplifiers.* Proceedings of the IEEE, 2007. **95**(9): p. 1757-1766.

17. Patent, E.A., et al., *First integrated combiner based on self-switching in quantum dots.* IEEE Photonics Technology Letters, 2004. **16**(10): p. 2308-2310.

18. Haverkort, J.E.M., et al. *Photonic switching in InAs/InP quantum dots*. 2004.

19. Ghosh, S., et al., *Nonlinear optical and electro-optic properties of InAs/GaAs self-organized quantum dots.* Journal of Vacuum Science & Technology B: Microelectronics and Nanometer Structures, 2001. **19**: p. 1455.

20. Prasanth, R., J.E.M. Haverkort, and J.H. Wolter, *Electro-refraction in quantum dots: dependence on lateral size and shape.* IEEE Transactions on Nanotechnology, 2004. **3**(2): p. 270-274.

21. Qasaimeh, O., et al., *Linear and quadratic electro-optic coefficients of self-organized In0. 4Ga0. 6As/GaAs quantum dots.* Applied Physics Letters, 1998. **72**(11): p. 1275-1277.

22. Ukhanov, A.A., et al., *Comparison of the carrier induced refractive index, gain, and linewidth enhancement factor in quantum dot and quantum well lasers.* Applied Physics Letters, 2004. **84**: p. 1058.

23. Bennett, B.R., et al., *Carrier-induced change in refractive index of InP, GaAs and InGaAsP.* IEEE Journal of Quantum Electronics, 1990. **26**(1): p. 113-122.

24. Cheng, Y.B., et al., *Butt-coupled MOVPE growth for high-performance electro-absorption modulator integrated with a DFB laser.* Journal of Crystal Growth, 2007. **308**(2): p. 297-301.

25. Chen, Y., et al., *Quantum well electroabsorption modulators at 1.55 m using single step selective area chemical beam epitaxial growth.* Applied Physics Letters, 1992. **61**: p. 10.

26. Gibbon, M., et al., *Selective-area low-pressure MOCVD of GaInAsP and related materials on planar InP substrates.* Semiconductor Science and Technology, 1993. **8**: p. 998-1010.

27. Mokkapati, S., et al., *Controlling the properties of InGaAs quantum dots by selective-area epitaxy.* Applied Physics Letters, 2005. **86**: p. 113102.

28. Marsh, J.H., *Quantum well intermixing.* Semiconductor Science and Technology, 1993. **8**: p. 1136-1136.

29. Marsh, J.H., et al., *Quantum well intermixing in material systems for 1.5 micron.* J. Vac. Sci. Technol. A, 1998. **16**: p. 810–814.

30. Sudoh, T.K., et al., *Wavelength trimming by photoabsorption-included disordering for multiple-wavelength distributed-feedback laser arrays.* IEEE Photonics Technology Letters, 1997. **9**(7): p. 887-888.

31. Pape, I.J., et al., *Diffusion-induced disordering of GaInAs/InP multiple quantum wells with zinc.* Electronics Letters, 1988. **24**: p. 910.

32. Helmy, A.S., et al., *A Study of Impurity-Free Vacancy Disordering in GaAs-AlGaAs for Improved Modeling.* IEEE Journal of Selected Topics in Quantum Electronics, 1998. **4**(4): p. 661-668.

33. May-Arrioja, D.A., et al., *Intermixing of InP-based multiple quantum wells for integrated optoelectronic devices.* Microelectronics Journal, 2009. **40**(3): p. 574-576.

34. Si, S.K., et al., *Area selectivity of InGaAsP-InP multiquantum-well intermixing byimpurity-free vacancy diffusion.* IEEE Journal of Selected Topics in Quantum Electronics, 1998. **4**(4): p. 619-623.

35. Sudo, S., et al., *Impurity-free disordering of InGaAs/InGaAlAs quantum wells on InP by dielectric thin cap films and characterization of its in-plane spatial resolution.* Jpn. J. Appi. Phys. Vol, 1996. **35**: p. 1276-12 9.

36. Yu, J.S., et al., *Fabrication of wavelength-shifted In0. 2Ga0. 8As/GaAs multiple quantum well laser diodes by impurity-free vacancy disordering at different thermal annealing temperatures.* Semiconductor Science and Technology, 2003. **18**(2): p. 170-173.

37. Khreis, O.M., W.P. Gillin, and K.P. Homewood, *Interdiffusion: A probe of vacancy diffusion in III-V materials.* Physical Review-Section B-Condensed Matter, 1997. **55**(23): p. 15813-15818.

38. Lee, A.S.W., et al., *Enhanced band-gap blueshift due to group V intermixing in InGaAsP multiple quantum well laser structures induced by low temperature grown InP.* Applied Physics Letters, 2001. **78**: p. 3199.

39. Lever, P., H.H. Tan, and C. Jagadish, *Impurity free vacancy disordering of InGaAs quantum dots.* Journal of Applied Physics, 2004. **96**: p. 7544.

40. Guido, L.J., et al., *Effects of dielectric encapsulation and As overpressure on Al Ga interdiffusion in AlGa As GaAs quantum well heterostructures.* Journal of Applied Physics, 1987. **61**: p. 1372.

41. Yu, J.S. and Y.T. Lee, *Impurity-Free Vacancy Diffusion of InGaAsP/InGaAsP Multiple Quantum Well Structures Using SiH~ 4-Dependent Dielectric Cappings.* JAPANESE JOURNAL OF APPLIED PHYSICS PART 1 REGULAR PAPERS SHORT NOTES AND REVIEW PAPERS, 2007. **46**(10A): p. 6509.

42. Beauvais, J., et al., *Suppression of bandgap shifts in GaAs/AlGaAs quantum wells using strontium fluoride caps.* Electronics Letters, 1992. **28**(17): p. 1670-1672.

43. Fu, L., et al., *Suppression of interdiffusion in InGaAs/GaAs quantum dots using dielectric layer of titanium dioxide.* Applied Physics Letters, 2003. **82**: p. 2613.

44. Gao, Q., et al., *Effects of thermal stress on interdiffusion in InGaAsN/GaAs quantum dots.* Applied Physics Letters, 2004. **84**: p. 4950.

45. Djie, H.S. and T. Mei, *Plasma-induced quantum well intermixing for monolithic photonic integration.* IEEE Journal of Selected Topics in Quantum Electronics, 2005. **11**(2): p. 373-382.

46. Ooi, B.S., A.C. Bryce, and J.H. Marsh, *Integration process for photonic integrated circuits using plasmadamage induced layer intermixing.* Electronics Letters, 1995. **31**(6): p. 449-451.

47. He, J.J., et al., *Bandgap shifted InGaAsP/InP quantum well waveguides using MeV ionimplantation.* Electronics Letters, 1995. **31**(24): p. 2094-2095.

48. Paquette, M., et al., *Blueshifting of InGaAsP-InP laser diodes using a low-energyion-implantation technique: comparison between strained andlattice-matched quantum-well structures.* IEEE Journal of Selected Topics in Quantum Electronics, 1998. **4**(4): p. 741-745.

49. Helmy, A.S., et al., *Control of silica cap properties by oxygen plasma treatment for single-cap selective impurity free vacancy disordering.* Applied Physics Letters, 1999. **74**: p. 732.

50. Stesmans, A., *Passivation of P and P interface defects in thermal (100) Si/SiO with molecular hydrogen.* Applied Physics Letters, 1996. **68**: p. 2076.

51. Wright, A.F., *Interaction of hydrogen with gallium vacancies in wurtzite GaN.* Journal of Applied Physics, 2001. **90**: p. 1164.

52. Van de Walle, C.G., *Interactions of hydrogen with native defects in GaN.* Physical Review B, 1997. **56**(16): p. 10020-10023.

53. Yoon, E., et al., *GaAs surface modification by room temperature hydrogen plasma passivation.* Applied Physics Letters, 1992. **60**: p. 2681.

54. Dutta, R., P.K. Banerjee, and S.S. Mitra, *Amorphous silicon-carbon-fluorine alloy films.* Physical Review B, 1983. **27**(8): p. 5032-5038.

55. Shamirzaev, T.S., et al., *Passivation of growth defects in GaAs/AlGaAs multiple quantum well structures by CF4 plasma.* Physica B: Condensed Matter, 2001. **308**: p. 761-764.

56. Fedina, L., et al., *In situ HREM irradiation study of point-defect clustering in MBE-grown strained Si_ {1-x} Ge_ {x}/(001) Si structures.* Physical Review B, 2000. **61**(15): p. 10336-10345.

57. Pepin, A., et al., *Evidence of stress dependence in SiO/SiN encapsulation-based layer disordering of GaAs/AlGaAs quantum well heterostructures.* Journal of Vacuum Science & Technology B: Microelectronics and Nanometer Structures, 1997. **15**: p. 142.

58. Gareso, P.L., et al., *Suppression of thermal atomic interdiffusion in C-doped InGaAs/AlGaAs quantum well laser structures using TiO 2 dielectric layers.* Applied Physics Letters, 2004. **85**(23): p. 5583-5585.

59. Street, M.W., et al., *Modification of the second-order optical nonlinearities in AlGaAs asymmetric multiple quantum well waveguides by quantum well intermixing.* Applied Physics Letters, 1997. **70**: p. 2804.

60. Zhuravlev, K.S., A.L. Sokolov, and K.P. Mogil'nikov, *Transformation of nonradiative recombination centers in GaAs/AlGaAs quantum well structures upon treatment in a CF 4 plasma followed by low-temperature annealing.* Semiconductors, 1998. **32**(12): p. 1293-1298.

61. Hamilton, C.J., et al., *Suppression of bandgap shifts in GaAs/AlGaAs multiquantum wellsusing hydrogen plasma processing.* Electronics Letters, 1995. **31**(16): p. 1393-1394.

62. Ridha, P., et al., *Polarization dependence study of electroluminescence and absorption from InAs/ GaAs columnar quantum dots.* Applied Physics Letters, 2007. **91**: p. 191123.

63. Davis, L., et al., *Photoluminescence and electro-optic properties of small (25–35 nm diameter) quantum boxes.* Applied Physics Letters, 1993. **62**: p. 2766.

64. Schmitt-Rink, S., D.A.B. Miller, and D.S. Chemla, *Theory of the linear and nonlinear optical properties of semiconductor microcrystallites.* Physical Review B, 1987. **35**(15): p. 8113-8125.

65. Seaward, K.L., N.J. Moll, and W.F. Stickle, *Surface contamination and damage from CF 4 and SF 6 reactive ion etching of silicon oxide on gallium arsenide.* Journal of Electronic Materials, 1990. **19**(4): p. 385-391.

66. Sugawara, M. and B.L. Stansfield, *Plasma etching: fundamentals and applications*. 1998, Oxford University Press, USA. p. 70-71.

67. Jansen, H., et al., *A survey on the reactive ion etching of silicon in microtechnology.* Journal of Micromechanics and Microengineering, 1996. **6**: p. 14-28.

68. Yu, D.G., et al., *Comparing ion damage in GaAs and InP.* Microelectronic Engineering, 1997. **35**(1): p. 95-98.

69. Ennos, A.E., *Stresses developed in optical film coatings.* Applied optics, 1966. **5**(1): p. 51-61.

70. Djie, H.S., T. Mei, and J. Arokiaraj, *Photoluminescence enhancement by inductively coupled argon plasma exposure for quantum-well intermixing.* Applied Physics Letters, 2003. **83**: p. 60.

71. Adachi, S. and H. Kawaguchi, *Chemical etching characteristics of (001) InP.* Journal of The Electrochemical Society, 1981. **128**: p. 1342.

72. Ikossi Anastasiou, K., et al., *Wet Chemical Etching with Lactic Acid Solutions for InP based Semiconductor Devices.* Journal of The Electrochemical Society, 1995. **142**: p. 3558.

73. Levy, D.S., et al., *Fabrication of ultracompact 3-dB 2× 2 MMI power splitters.* IEEE Photonics Technology Letters, 1999. **11**(8): p. 1009-1011.

74. Soldano, L.B. and E.C.M. Pennings, *Optical multi-mode interference devices based on self-imaging: principles and applications.* Lightwave Technology, Journal of, 1995. **13**(4): p. 615-627.

75. Earnshaw, M.P., et al., *8 x 8 optical switch matrix using generalized Mach–Zehnder interferometers.* IEEE Photon. Technol. Lett, 2003. **15**(6): p. 810–812.

76. Paiam, M.R. and R.I. MacDonald, *Design of phased-array wavelength division multiplexers using multimode interference couplers.* Applied optics, 1997. **36**(21): p. 5097-5108.

77. Tseng, S.Y., et al., *Variable splitting ratio 2× 2 MMI couplers using multimode waveguide holograms.* Optics Express, 2007. **15**(14): p. 9015-9021.

78. Tseng, S.Y., S. Choi, and B. Kippelen, *Variable-ratio power splitters using computer-generated planar holograms on multimode interference couplers.* Optics Letters, 2009. **34**(4): p. 512-514.

79. Feng, D.J.Y. and T.S. Lay, *Compact multimode interference couplers with arbitrary power splitting ratio.* Optics Express, 2008. **16**(10): p. 7175-7180.

80. May-Arrioja, D.A., et al., *A reconfigurable multimode interference splitter for sensing applications.* Measurement Science and Technology, 2007. **18**(10): p. 3241-3246.

81. Kumai, S., et al., *High-speed optical switching of InAlGaAs/InAlAs multi-mode interference photonic switch with partial index-modulation region (MIPS-P).* IEICE Electronics Express, 2005. **2**(23): p. 578-582.

82. Leuthold, J. and C.H. Joyner, *Multimode interference couplers with tunable power splitting ratios.* Journal of Lightwave Technology, 2001. **19**(5): p. 700-707.

83. Nagai, S., et al., *Multimode interference photonic switches (MIPS).* Journal of Lightwave Technology, 2002. **20**(4): p. 675.

84. Lu, X., et al., *Polarization-insensitive thermo-optic switch based on multimode polymeric waveguides with an ultralarge optical bandwidth.* Applied Physics Letters, 2000. **76**: p. 2155.

85. Wang, F., et al., *Optical switch based on multimode interference coupler.* IEEE Photonics Technology Letters, 2006. **18**(2): p. 421-423.

86. Hong, J.K., S.S. Lee, and D.W. Shin, *Reduced-Power Consuming Silica-Based Compact 1 x 2 MZI Thermo-Optic Switch Using MMI Couplers.* JOURNAL-KOREAN PHYSICAL SOCIETY, 2004. **45**: p. 84-87.

87. Yang, D., et al., *Fabrication of a 4 4 strictly nonblocking SOI switch matrix.* Optics Communications, 2005. **250**(1-3): p. 48-53.

88. Moyer, P.J., S.A. Pridmore, and F. Farahi, *Multimode interference switch design with loose manufacturing tolerance.* Optical Engineering, 2004. **43**: p. 165.

89. Weng, T.H. *A comparative study of p-type diffusion in III-V compoundsemiconductors*. 1997.

90. May-Arrioja, D.A., N. Bickel, and P. Likamwa, *Robust 2× 2 multimode interference optical switch.* Optical and Quantum Electronics, 2006. **38**(7): p. 557-566.

91. Xie, N., T. Hashimoto, and K. Utaka, *Very Low Power Operation of Compact MMI Polymer Thermooptic Switch.* IEEE Photonics Technology Letters, 2009. **21**(18): p. 1335.

92. Ibrahim, M.H., et al., *A Novel 1x 2 Thermo-Optic Multimode Interference Switch Structure Based on Photodefinable Benzocyclobutene (BCB 4024-40) Polymer on Silica.* Chinese Physics letters, 2006. **23**(10): p. 2796.

93. Yaacob, M., et al., *Switching power improvement of hybrid polymer-silica based MMI thermo-optical switch.* Journal of Optoelectronics and Advanced Materials, 2009. **11**(5): p. 559-564.

94. Yeo, D.M. and S.Y. Shin, *Polymer-silica hybrid 1 x 2 thermooptic switch with low crosstalk.* Optics Communications, 2006. **267**(2): p. 388-393.

95. Norwood, R.A. *Hybrid polymer devices for improved thermal control and performance*. 2001.

96. Xia, J., et al., *Low power 2× 2 thermo-optic SOI waveguide switch fabricated by anisotropy chemical etching.* Optics Communications, 2004. **232**: p. 223-228.

97. Yang, D., et al., *A 2x2 SOI Mach-Zehnder thermo-optical switch based on strongly guided paired multimode interference couplers.* OPTOELECTRONICS LETTERS, 2007. **3**(5): p. 334.

98. Li, L.H., et al., *Growth and characterization of InAs columnar quantum dots on GaAs substrate.* Journal of Applied Physics, 2007. **102**: p. 033502.

99. Zilkie, A.J., et al., *Femtosecond gain and index dynamics in an InAs/InGaAsP quantum dot amplifier operating at 1.55 μm.* Optics Express, 2006. **14**(23): p. 11453-11459.

100. Bambha, R., et al., *Carrier escape dynamics in a single quantum well waveguide modulator.* Optical and Quantum Electronics, 1993. **25**(12): p. 965-971.

101. Sahara, R., et al., *Proposal for quantum-dot electroabsorption modulator.* IEEE Photonics Technology Letters, 1996. **8**(11): p. 1477-1479.

102. Cheng, Y.C., et al., *Fabrication of a far-infrared photodetector based on InAs/GaAs quantum-dot superlattices.* Optical Engineering, 2003. **42**: p. 119.

103. Campbell, J.C. and A. Madhukar, *Quantum-dot infrared photodetectors.* Proceedings of the IEEE, 2007. **95**(9): p. 1815-1827.

104. Bickel, N. and P. LiKamWa, *Etched quantum dots for all-optical and electro-optical switches.* Microelectronics Journal, 2008. **39**(3-4): p. 362-364.

105. Bestwick, T.D., et al., *Uniform and efficient GaAs/AlGaAs quantum dots.* Applied Physics Letters, 1995. **66**: p. 1382.

106. Steffen, R., et al., *Photoluminescence study of deep etched InGaAs/GaAs quantum wires and dots defined by low-voltage electron beam lithography.* Applied Physics Letters, 1996. **68**: p. 223.

107. Delpon, E.L., et al., *Ultrafast excitonic saturable absorption in ion-implanted InGaAs/InAlAs multiple quantum wells.* Applied Physics Letters, 1998. **72**: p. 759.

108. Loka, H.S. and P.W.E. Smith, *Ultrafast all-optical switching in an asymmetric Fabry-Perot deviceusing low-temperature-grown GaAs.* IEEE Photonics Technology Letters, 1998. **10**(12): p. 1733-1735.

109. Ledentsov, N.N., et al., *Quantum-dot heterostructure lasers.* IEEE Journal of Selected Topics in Quantum Electronics, 2000. **6**(3): p. 439-451.

110. Hamoudi, A., et al., *An optical study of interdiffusion in strained InP-based heterostructures.* Japanese journal of applied physics, 1995. **34**(1): p. 36-41.

111. Vahala, K.J., *Quantum box fabrication tolerance and size limits in semiconductorsand their effect on optical gain.* IEEE Journal of Quantum Electronics, 1988. **24**(3): p. 523-530.

112. Vieu, C., et al., *Electron beam lithography: resolution limits and applications.* Applied Surface Science, 2000. **164**(1-4): p. 111-117.

113. Varoutsis, S., et al., *Reactive-ion etching of high-Q and submicron-diameter GaAs/ AlAs micropillar cavities.* Journal of Vacuum Science & Technology B: Microelectronics and Nanometer Structures, 2005. **23**: p. 2499.

114. Leonard, D., et al., *Direct formation of quantum-sized dots from uniform coherent islands of InGaAs on GaAs surfaces.* Applied Physics Letters, 1993. **63**: p. 3203.

115. Ganichev, S., et al., *Conversion of spin into directed electric current in quantum wells.* Science Phys Rev Lett, 1997. **86**: p. 4358.